# Measurement of the $G$ Double-Polarisation Observable in Positive Pion Photoproduction


*Josephine McAndrew*

A thesis submitted in fulfilment of the requirements
for the degree of Doctor of Philosophy
to the
University of Edinburgh
July 2011

# Abstract

Establishing the resonance spectrum of the nucleon with accuracy would provide important new information about the dynamics and degrees of freedom of its constituents. The spectrum and properties of nucleon resonances are a fundamental test of the emerging predictions from Lattice QCD calculations and will guide refinements to QCD-based phenomenological models. Pion photoproduction is an excellent tool to study the nucleon resonance spectrum, as this channel is expected to couple strongly to most resonances. The new generation of measurements for this reaction, of which the measurement presented in this thesis forms a crucial part, will provide a great improvement in the quality of available experimental data. For the photoproduction process in particular, the use of photon beams and targets with high degrees of polarisation, coupled with large acceptance particle detectors is essential for disentangling the spectrum of excited states.

There are many nucleon resonances predicted by recent Lattice QCD calculations and by phenomenological nucleon models which are only observed inconsistently by different analyses of the same experimental data or which are not observed at all. It is of upmost importance to establish if this means that the resonances do not exist in nature, reflecting inappropriate degrees of freedom in the theoretical description of the nucleon or if the current experimental measurements have not been sensitive enough. As such, there is a current world effort at modern tagged photon facilities to measure the "complete set" of photoproduction observables necessary to fully constrain the partial wave analyses used to extract the experimental excitation spectrum from the data.

This thesis will present the first detailed measurement to date of positive pion photoproduction in the 730-2300 MeV photon energy (1400-2280 MeV centre-of-mass energy) region with a linearly polarised photon beam and a longitudinally

polarised proton target with a close-to-complete angular coverage in detection of the reaction products. This unique set up allows for the extraction of the double-polarisation observable, $G$. The data were taken as part of the $g9$ experiment at the Thomas Jefferson National Accelerator Facility in Virginia, using a tagged, polarised photon beam and the Frozen Proton Spin Target, FROST, in conjunction with the CEBAF Large Acceptance Spectrometer, CLAS.

The results of the study presented here are compared to the sparse existing data set for the $G$ double-polarisation observable along with the current solutions of the the three main partial wave analyses: MAID, SAID and Bonn-Gatchina. Some agreement is obtained with the expectations of these PWA at lower energies, while disagreement at higher energies is clearly evident. This is the energy region where many of the missing resonances are expected to lie. Once incorporated into the MAID, SAID and Bonn-Gatchina models, these new data will provide an important contribution to constraining the amplitudes and therefore the resonance spectrum and properties of the nucleon. The new data will form a central part of the world effort to accurately establish the nucleon excitation sepctrum for the first time by achieving the first complete measurement of experimental observables in meson photoproduction.

# Declaration

Except where otherwise stated, the research undertaken in this thesis was the unaided work of the author. Where the work was done in collaboration with others, a significant contribution was made by the author.

*J. McAndrew*
July 2011

# Acknowledgements

I would first like to thank my supervisor, Dan Watts, for all his help and guidance over the past few years and Derek Glazier for his invaluable advice with my analysis.

I would also like to thank the members of the Edinburgh Photonuclear Group: Pauline Hall-Barrientos, Tom Jude and Mark Sikora. I am grateful for their advice and support throughout my PhD and for their company at conferences and experiments. Special thanks go to Daria Sokhan for introducing me to life at JLab and to Claire Tarbert for teaching me the basics of ROOT. I should also extend my thanks to the Edinburgh Nuclear Group in general, for creating such a nice environment to work in. And I am particularly grateful to Philip Salter for all of his computing support.

I am also grateful to all my colleagues at the University of Glasgow for their advice and support with my analysis, in particular Ken Livingston and Bryan McKinnon. Special thanks also to Stuart Fegan, David Hamilton and Gary Smith for our trips to the County Grill, and endless games of Scrabble.

I would also like to thank all the members of the FROST Group at JLab, in particular Eugene Pasyuk, Mike Dugger and Igor Strakovsy. I am grateful for their support and guidance and, most importantly, their patience in answering all of my questions. I am also very grateful to the Target Group, for sharing their knowledge of FROST, NMR and the best restaurants and bars in Newport News. Special thanks goes to Chris Keith for teaching me so much about polarised targets and NMR and for his support and guidance while I was calculating the target polarisation.

I am also very grateful to Jane Patterson for dealing with administration so efficiently and for always having the answer to any administrative problems.

I would like to thank my boyfriend, Didier Caneilles, for his unfailing support

over the past few years. I am very grateful to him for his patience and encouragement, especially during my darkest days finishing my analysis and writing up.

Finally, I would like to dedicate this thesis to my father, Antoni Gadomski. He always encouraged me to seek new challenges and to do the best that I can, supporting me in all my endeavours. He was determined that I would complete a PhD and it is sad to think that he will never know that I have done so. I know that he would have been extremely proud.

# Contents

# List of Figures

# List of Tables

# Chapter 1

# Introduction

The nucleon is a fundamental component of all visible matter in the Universe, and responsible for over 99% of its mass. Understanding nucleon structure is therefore fundamental to our understanding of the Universe around us. Since the discovery of the proton by Rutherford in 1919, and the neutron by Chadwick in 1932, it is only in recent decades that the theoretical description of the nucleon has made significant progress. The quark models of the nucleon developed in the 1960s have recently been complemented by more ab-initio calculations based on the interactions of the nucleons and their consituents via Quantum Chromodynamics.

However, a common feature of these models is their inability to predict the experimentally observed nucleon excitation spectrum; they predict many resonances which are not yet observed or fail to correctly predict the properties of resonances whose existence is established experimentally, such as the lowest excited state of the proton, the Roper resonance.

The most promising tool to better establish the excitation spectrum of the nucleon is meson photoproduction. As such there is a current world effort at photon beam facilities to carry out as close to complete as possible studies of the nucleon excited states. In particular, the NSTAR programme at the Thomas Jefferson National Accelerator Facility (JLab) in Virginia aims to obtain a better understanding of the nucleon excited spectrum through the use of electromagnetic probes. The main photoproduction experiment in this programme is FROST, which utilises the CEBAF electron accelerator to produce an intense beam of high-energy tagged polarised photons, the frozen proton-spin polarised target FROST, and the CLAS spectrometer to detect a wide range of final-state particles

over close-to-complete angular coverage. This project will provide many of the first precise and high statistics measurements of single and double-polarisation observables observables in meson photoproduction on the proton. The data analysed for this thesis were taken from October 2007 to February 2008 during the first half of the FROST experiment, *g9a*.

This thesis will present a new and detailed measurement for the $G$ double-polarisation observable for the reaction channel $\gamma(p,\pi^+)n$ in the photon energy region 730-2300 MeV, corresponding to a centre-of-mass energy region of 1400-2280 MeV. This is the double-polarisation observable accessible in measurements of meson photoproduction with simultaneous linear polarisation of the beam and longitudinal spin-polarisation of the nucleon target. There are little existing data for this observable, and the current world data set suffers from large uncertainties and exhibits puzzling long-standing disrepancies with all modern partial wave analysis solutions for $G$ in certain kinematic regions. As such, a new precise and high statistics measurement is essential.

The theoretical background to this experiment and this thesis will be presented in Chapters 2 and 3, the former providing a general background to nucleon structure, QCD and the importance of the field of hadron spectroscopy while the latter will describe the formalism of the kinematics of photoproduction and the origin of polarisation observables. Chapter 4 will then discuss the previous measurements of the $G$ observable and why a new measurement is required. The JLab Facility and *g9a* experimental set up will be described in Chapter 5, followed by a description of the FROST target and the calculation of the target polarisation in Chapter 6, which were both essential to this experiment. Chapters 8 and 9 will describe the analysis carried out in order to identify the reaction channel of interest and to extract the $G$ observable. The results and their implications will then be presented in Chapter 10.

# Chapter 2

# Theoretical Background

The proton and the neutron can be thought of as two states of the same particle, the nucleon. This idea was originally proposed by Heisenberg in 1932 to explain the nearly equal masses of these two particles[1]. Heisenberg proposed a new spin quantum number, isospin ($I$), which has a value of 1/2 for the nucleon. The proton and neutron are therefore isospin substates with $I_3$=*+1/2* and $I_3$=*-1/2* respectively, whose charge, $Q$, can now be expressed as:

$$\frac{Q}{e} = \frac{1}{2} + I_3 \tag{2.1}$$

where $e$ is the electronic charge. Three years later, in 1935, Yukawa proposed the existence of the "strong force" to hold the nucleons together in the nucleus. He postulated that this force must be mediated by the exchange of a spin-0 meson with a mass $\sim$150 MeV/c$^2$ [2]. This particle, the pion, was first observed in 1947 in cosmic ray experiments by Lattes *et al.*, and it now known to be the propagator of the strong force at distances $\geq$2 fm [3]. In the same year, the cosmic ray studies of Raymond and Butler revealed new particles leading to the advent in 1952 of the "strangeness" quantum number, $s$, by Pais. Raymond and Butler had observed charged and neutral particles which were created on a timescale $\sim 10^{-20}$ s (at the same rate as pions), but which decayed into two pions after $\sim 10^{-10}$ s. This decay time is much slower than the time expected for a strong interaction and is characteristic of the weak interaction. These particles were initially named "V particles" due to the form of their cloud chamber tracks, but later identified as the K-mesons. This anomalous behaviour could only be explained by the existence of

[1]The mass of the proton is 938.27 MeV/c$^2$ compared to 939.57 MeV/c$^2$ for the neutron [1].

a new quantum number, conserved in strong or electromagnetic interactions but not conserved in weak interactions. These "strange" particles must be created in pairs via the strong interaction to conserve strangeness, but once separated decay via the weak force in which strangeness is not conserved. With this new quantum number, the equation for the charge of a particle can be extended to:

$$\frac{Q}{e} = \frac{B+S}{2} + I_3 = \frac{Y}{2} + I_3 \tag{2.2}$$

where $B$ is the baryon number and $Y$ is hypercharge, $B+S$. This was the beginning of a new, and much more complex, picture of fundamental physics. With the development of high-energy particle accelerators in the 1950s, such as the proton synchrotron at Brookhaven which could reach energies up to 3 GeV [4], an increasing number of new particles were found and it became obvious that a framework was required in order to interpret them.

The first step towards such a framework was proposed by Gell-Mann and Nishijima in 1961. They recognised that these particles occur in families with masses which differ by only a few MeV. It had already been seen that the proton and the neutron form an isospin doublet, but larger isospin multiplets could be created in which the particles have the same spin, parity and hypercharge. These multiplets are most clearly demonstrated by representing each particle as a point on a "weight diagram" of hypercharge against $I_3$. The weight diagrams of the lightest $J^{\pi}=1/2$ and $J^{\pi}=3/2$ baryon multiplets ($B=1$) are shown in Figure 2.1. The success of such an approach was demonstrated in 1965 by the discovery of the $\Omega^-$ particle. Its existence had been predicted by Gell-Mann in 1962 as a particle required to complete the baryon decuplet shown in Figure 2.1, with $J^{\pi}=3/2$ and a mass of $\sim$1680 MeV [5].

In 1964 Gell-Mann and Zweig proposed that these patterns could be explained if all baryons and mesons were made up of three fundamental particles, or quarks, that came in three types: up ($u$), down ($d$), and strange ($s$)[2].

[2]A heavier generation of quarks has also been discovered, charm ($c$) in 1974, bottom ($b$) in 1977, and top ($t$) in 1995, playing a role only in more exotic two and three-quark systems.

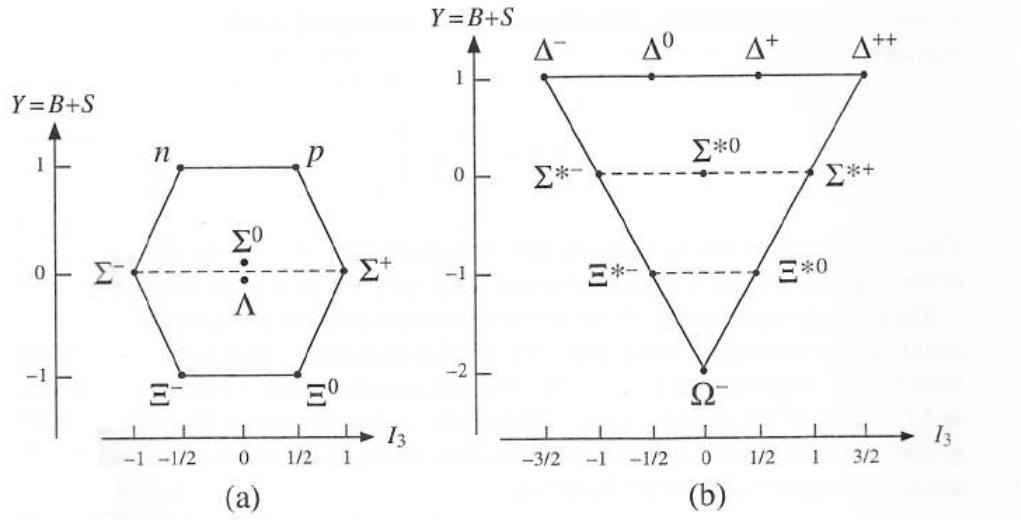


Figure 2.1: The two lightest baryon multiplets: (a) the $J^{\pi}=1/2$ octet to which the proton and neutron belong and (b) the $J^{\pi}=3/2$ decuplet [3].

## 2.1 The Quark Model

In this model all baryons are formed of three quarks, the proton being *uud* and the neutron being *ddu*, for example. Mesons are made of quark anti-quark pairs, such as $u\bar{d}$ for the $\pi^+$. As the nucleon has a baryon number of 1, quarks must have a baryon number of 1/3 and therefore fractional charges of 2/3, -1/3 and -1/3 for the *u,d* and *s* quarks respectively. The *u* and *d* quarks also form an $s$=0 isospin doublet, while the *s* quark is an $s$=-1 isospin singlet. The similarity in masses of the proton and neutron could now be explained by the down quark being only a few MeV heavier than the up quark[3]. The strange quark is ∼100 MeV heavier than the up or down quarks [1], explaining the large observed mass difference of particles which possess strangeness. The first observation of quarks was made at SLAC in 1968 through deep inelastic lepton scattering experiments.

Even though the quark model was able to explain the regular patterns in observed particles and successfully predict the existence of new ones, there were two main limitations to the model. The first is the question of why quarks are confined within hadrons and why free quarks have never been observed, a

[3]The mass of the up quark is 1.7-3.3 MeV, while the mass of the down quark is 4.1-5.8 MeV [1].

question that the more modern theory of QCD addresses. The second was the existence of particles whose quark configurations appeared to violate the Pauli Exclusion Principle. The quark model assumes the symmetry of space and spin wavefunctions under the exchange of light quarks, meaning that particles such as the $\Delta^{++}$ ($uuu$), $\Delta^{-}$ ($ddd$), and $\Sigma^{-}$ ($sss$) contain three quarks of the same type and with parallel spins [3]. The solution to this problem, as proposed by Greenberg in 1964, was to introduce a new quantum number called "colour", where each quark can have one of three colour states (red, green or blue), with the hadron itself being colourless and the forces between the quarks being colour independent. As the colour wavefunction could be anti-symmetric, the Exclusion Principle was no longer violated. Experimental evidence for the colour quantum number is seen through $e^+e^-$ scattering experiments where the predicted cross section increases by a factor of three, to agree with experiment, if colour is included as an extra degree of freedom in calculations [2].

## 2.2 Quantum Chromodynamics, QCD

QCD is the formal theory of the colour interactions (strong force) between quarks. It can be thought of as being analogous to QED, with the strong force mediated by masseless vector bosons called gluons. The gluons themselves carry a colour anti-colour charge in order to conserve colour charge at the quark-gluon reaction vertex. As a result, the gluons can also self-interact and couple to each other via the strong force, unlike the photons which mediate the electromagnetic force in QED.

The strength of the strong interaction is governed by the strong coupling constant, $\alpha_s$. This is a running coupling constant, which is shown in Figure 2.2 as a function of momentum transfer, $Q$. This term appears in the QCD Lagrangian which determines the dynamics and degrees of freedom of the quarks and gluons inside the hadron. When the Feynman path integrals obtained from the Lagrangian are expanded in terms of power series in order to solve them perturbatively, $\alpha_s$ also appears in these expansions. As can be seen in Figure 2.2, $\alpha_s$ is small and relatively constant at high momenta (or equivalently small quark separations $\leq$1 fm). This is often referred to as the "perturbative" regime of QCD, where the power series expansions converge. Difficulties arise at lower momenta

$\leq$1 GeV (or larger quark separations $\geq$1 fm), where $\alpha_s$ increases rapidly towards unity. In this "non-perturbative" regime the power series now diverge rapidly and perturbation theory can no longer be applied to solve the QCD Lagrangian. This asymptotic freedom of the coupling constant is typical of non-Abelian field theories such as QCD, and is due to the self-interaction of the gluons. Therefore, as hadrons lie within this non-perturbative regime, realistic predictions of their properties cannot be directly obtained from QCD. An interesting consequence of asymptotic freedom is that it can explain the question of confinement. As quark separation increases, the value of the strong coupling constant increases so rapidly that the binding energy increases until it becomes energetically favourable to produce a quark anti-quark pair rather than remove a quark from the hadron.

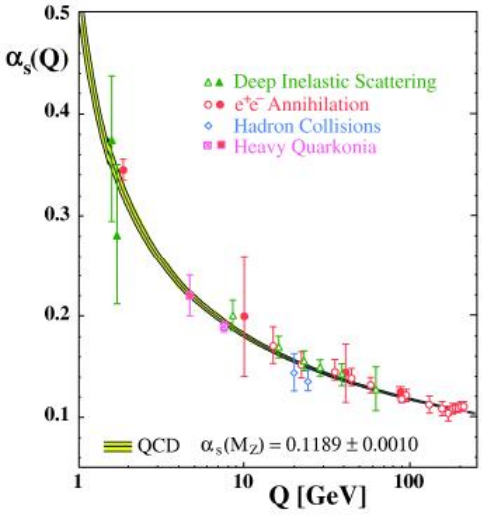


Figure 2.2: The strong coupling constant as predicted by QCD plotted as a function of momentum transfer along with experimental data points [6].

The QCD view of the nucleon is therefore much more complex than that of the early quark model. The valence quarks are now thought to only account for $\sim$1% of hadron mass, the major contribution arising from the gluon-gluon interactions.

## 2.3 Lattice QCD

By making certain approximations, it is still possible to perform QCD-based calculations and to therefore obtain useful predictions from QCD. The most successful example of this is Lattice QCD (LQCD), pioneered by Wilson in 1974 [7]. Here spacetime is approximated by a lattice of discrete points on which the quarks are placed, while the gluons propagate along the grid which links the points. With a finite lattice spacing, $a$, and a finite lattice volume, $V$, a high and low momentum cut-off is introduced to the calculations. This allows the QCD Lagrangian to become well-defined and solutions can be found using Monte Carlo techniques. The grid spacing can then be extrapolated to zero (the continuum limit) and the volume increased in order to obtain realistic predictions.

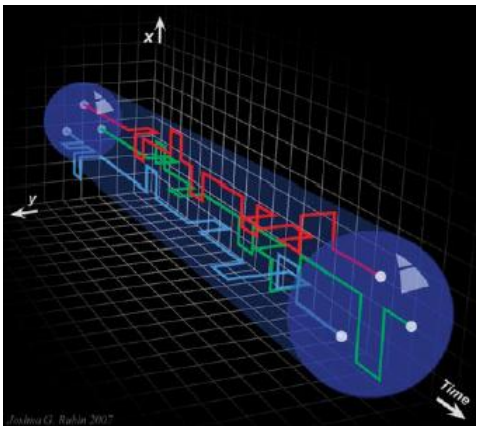


Figure 2.3: Illustration of the principles of Lattice QCD, showing propagation of the strong force between quarks along the lattice [8].

However, LQCD calculations are very intensive, and are limited by computing power and the calculation time required (the "cost" of the calculation). This scales with lattice spacing as $1/a^6$ [9] and with quark mass, $m_q$, as $1/m^p{}_q$, where $p$ has the value of two or three depending on the specific calculation [10]. Calculations are therefore perfomed with $u$ and $d$ quark masses $\sim$100 MeV [10] and the $s$ quark mass at approximately its actual value of $\sim$101 MeV [1] on a grid with a finite lattice spacing of $\sim$0.1 fm. The extracted parameters are then extrapolated to lighter masses as the grid spacing tends to zero. Figure 2.4 provides an example of this, showing how particle masses extracted from QCD are affected by the choice of lattice spacing and quark mass.

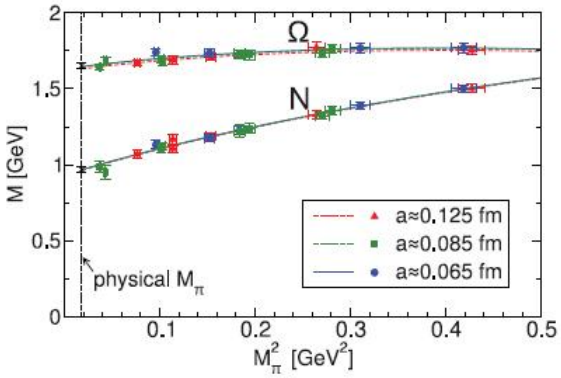


Figure 2.4: Mass of the nucleon (N) and the Ω baryon obtained from Lattice QCD calculations plot as a function of pion mass, $M_\pi$, for three different lattice spacings [11].

In spite of these limitations, some recent success has been made with LQCD calcuations. D*ürr et al.* have been able to calculate the masses of ten light hadrons agreeing with experimental values to within 1% despite using a pion mass of ∼190 MeV in the calculations [11]. Recent advances have also been made in the calculation of nucleon form factors [12], decay transitions [13] and for predictions of ground and excited states of nucleons [14].

## 2.4 Other QCD-Based Calculations

### 2.4.1 Chiral Perturbation Theory

At low momenta and within the regime of non-perturbative QCD, the effective degrees of freedom can be approximated as pions and nucleons, an assumption which forms the basis of many other QCD-based calculations. Chiral Perturbation Theory (ChiPT) is an effective field theory in which an effective Lagrangian is constructed based on the symmetries and symmetry breaking patterns of QCD such as chiral, parity and charge conjugation symmetry. Matrix elements and scattering amplitudes extracted from this Lagrangian are then expanded as a Taylor series and solved perturbatively. The quark field is split into two helicities, parallel and anti-parallel to momentum, with the quarks treated as massless particles so that their helicity does not change. As a result the Lagrangian is

chirally symmetric. This assumption that the quarks are massless leads to the main limitation of ChiPT, namely that realistic predictions are only made for hadrons containing *u, d* or *s* quarks and information about nucleon resonances cannot be directly extracted from the calculations. However, ChiPT is still a useful tool for the extrapolation of QCD, being able to describe the $\pi\pi$ and $\pi N$ interactions as well as having an important application as a test of the extent of chiral symmetry breaking in non-zero strangeness hadrons [10]. For a more in-depth description of Chiral Perturbation theory, the reader is directed to References [15] and [16].

## 2.5 Phenomenological Models

A second approach to obtain predictions about hadron properties in the absence of a rigorous solution to the QCD Lagrangian is to use QCD-inspired phenomenological models. These are complimentary to QCD-based calculations as they are designed to model certain aspects of QCD such as confinement, asymptotic freedom and consituent quarks. A brief description of some of the more successful models will be provided below, the reader being directed to texts such as Reference [10] for a general introduction, to Reference [17] for a comprehensive review of Quark Models and to Reference [18] for a comprehensive review of Bag and Soliton Models.

### 2.5.1 The Constituent Quark Models

The Constituent Quark models present the nucleon as being made up of three constituent quarks, each with ∼1/3 of the nucleon mass and confined within a simple 3D harmonic-oscillator potential. As quark mass decreases, the "bare" valence quarks of QCD become dressed by clouds of low-momentum gluons, increasing their masses from a few MeV/$c^2$ for the *u* and *d* quarks to ∼200-350 MeV/$c^2$, as shown in Figure 2.5.

Faiman and Hendry [20] proposed this relatively simple picture of the hadron, analogous to the shell model of nuclear physics, where resonances are created as excitations of the three quark system. This model was then extended by deRujula, Georgi and Glashow [21] to include aspects of QCD such as a long-range confining force independent of flavour along with a short range one-gluon

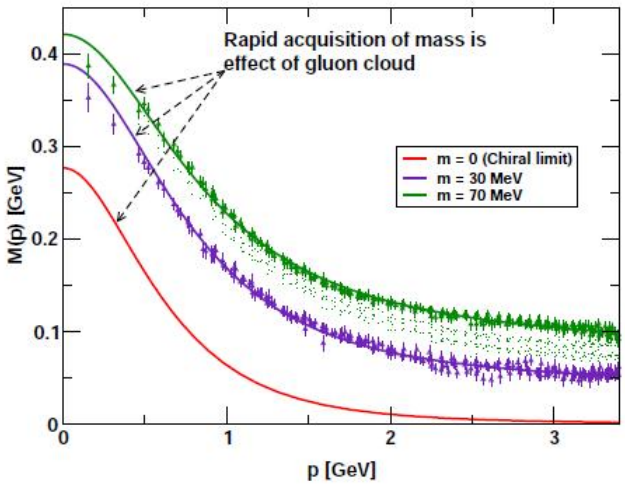


Figure 2.5: Plot showing theoretical predictions for the increase in the quark mass from the light valence quarks of QCD to the constituent quark mass as momentum decreases. The different curves are due to differences in the bare quark mass input into calculations [19].

exchange force. The idea of the harmonic oscillator potential was refined by Isgur and Karl [22], modifying the Hamiltonian to include an anharmonic perturbation and a hyperfine term.

In spite of the apparently simplistic and non-relativistic nature of the Constituent Quark Models, they have had much success in predicting baryon magnetic moments and experimentally observed excited states. However, one of the main limitations of these models is the tendancy to predict many more states than are experimentally observed, as will be discussed in Section 2.7. This tendancy can be explained if the quark models assume too many degrees of freedom. As a result, diquark models [23] were developed in which the nucleon is described as a quark and a diquark thus reducing the number of degrees of freedom. These models have had some success in predicting low-lying resonances [24], although there is some indication from recent Lattice QCD calculations that diquarks do not form [25].

### 2.5.2 Bag Models

Whereas the quark models tend to assume confinement of quarks within hadrons, other models place more emphasis on explaining this aspect of QCD. Bogoliubov

developed the Bag Model [26] in which quarks are massless particles confined within a finite spherical potential of fixed radius, while outside this volume they have infinite mass. This is achieved by the boundary conditions chosen at the surface and the quarks are confined by an inward pressure exerted by the bag. Perturbative QCD can be then be applied to the system inside the bag.

The MIT Bag Model [27] developed this idea further to place light quarks bound by weak forces into the interior of a finite spherical bag. The Cloudy Bag Model [28] refines this picture by adding terms involving a pion field at the surface of the bag in order to solve the problem of chiral symmetry breaking which arises from the boundary conditions.

The advantange of the Bag Models is that, unlike the Constituent Quark Models, they treat hadrons relativistically. They have had some success in predicting the masses of particles, as shown in Figure 2.6. In addition such models can also be used to make predictions for resonant states, and have been successful predicting the ratio of the mass of the Roper Resonance to the mass of the nucleon [10].

The Soliton Models are similar to the Bag Models, in that they developed from the SLAC Bag Model where a scalar field represents the surface of the bag and the quarks are localised to a spherical shell. Here the QCD vacuum is now a colour dielectric medium with a dielectric constant of $\kappa=1$ inside the potential and $\kappa=0$ outside with colour charges appearing has holes in the vacuum.

## 2.6 Experimental Studies

As QCD aims to fully describe the strong interaction in terms of quarks and gluons, experiments which reveal the dynamics of these particles within hadrons are a very important test of QCD. The baryon is the simplest system to exhibit QCD, thus exploring its excited (or resonant) states will provide such a test. Resonant states are labelled according to their rest mass, isospin, total angular momentum and orbital angular momentum as $X(m)L_{2I2J}$ where $X$ represents the type of particle, $m$ is the rest mass in MeV/c$^2$, $L$ is the lowest orbital angular momentum required for the states to decay to the ground state via emission of a meson expressed in spectroscopic notation, $I$ is isospin and $J$ is total angular momentum. These parameters can then be determined experimentally

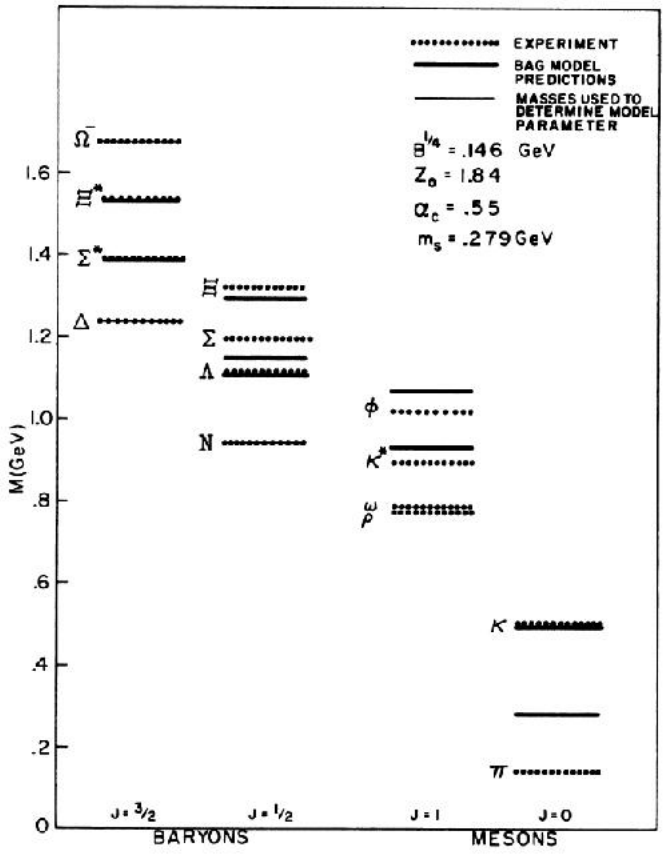


Figure 2.6: Light baryon and meson masses as predicted by the Bag Model. The actual values of the nucleon, $\Delta$, $\Omega$ and $\omega$ were used as fit parameters [29].

and compared with those predicted by theory. As will be discussed in Section 2.7, another important test of theory is the comparison of the number of resonances predicted to the number of resonances observed, as this is directly related to the number of degrees of freedom of the quarks and gluons.

Many different experimental techniques are available to probe the nucleon and to observe nucleon resonances, each being more sensitive to different aspects of nucleon structure. The basic principle is to use a beam of hadrons, electrons or photons to excite the nucleon in a proton or deuterium target to a resonant state which then decays via the strong force by the emission of mesons. The resonances are then observed through the detection of the final state products.

Beams of baryons such as protons, alpha particles and deuterons have been used extensively to study nucleon resonances and in particular the isospin degree

of freedom, due to the large cross sections obtained. The disadvantage of this technique is that the initial and final states are governed by the strong interaction, so significant initial and final state interactions make data analysis very complicated. The inelastic scattering of mesons such as pions can also be used as a probe of the nucleon. Again large cross sections are obtained and the final state interactions are slightly less complex as there is only one baryon in the final state. As such, $N\pi$ data form the majority of the world data set for the study of resonances even though QCD calculations predict that many resonances couple weakly to the $N\pi$ channel.

In spite of their smaller cross sections and non-resonant background contributions, electromagnetic probes (electrons and photons) are regarded as the best tools to explore the nucleon excited spectrum. The advantage of such experiments is that the interaction is well understood in terms of QED, there are negligible initial and final state interactions and the wavelength of the beam can be carefully selected. These probes also possess polarisation degrees of freedom which make them more sensitive to the transitions between states that reflect the internal structure of the nucleon. Resonance properties such as excitation energy, width, and branching ratios to different decay channels can therefore be extracted from the physical observables. Electron scattering is most suited to a detailed analysis of a specific resonance as the virtuality of the photon allows the transition to be explored at different distance scales. As electrons carry charge and therefore interact with charged particles, deep inelastic scattering also allows the charge and current disctributions of the nucleon to be explored. However, to look for new resonances the use of photons is preferable as only a single coupling at the real photon point needs to be constrained in analysing the data. This thesis will concentrate on the use of pion photoproduction as a probe of nucleon structure, the formalism of which will be fully explored in Chapter 3.

## 2.7 Current Experimental Knowldege

Table 2.1 summarises the current state of experimental knowledge for the $N$ and $\Delta$ resonances according to the Particle Data Group [1].

These resonances are for baryons which contain only $u$ or $d$ quarks, an $N$ resonance having isospin 1/2 and a $\Delta$ resonance having isospin 3/2. In order

Table 2.1: $N$ and $\Delta$ resonant states as recognised by the Particle Data Group along with their star rating indicating the likelihood of their existence [30].

| | | | Status as seen in — | | | | | | |
|---|---|---|---|---|---|---|---|---|---|
| Particle | $L_{2I\,2J}$ | Overall status | $N\pi$ | $N\eta$ | $\Lambda K$ | $\Sigma K$ | $\Delta\pi$ | $N\rho$ | $N\gamma$ |
| $N(939)$ | $P_{11}$ | **** | | | | | | | |
| $N(1440)$ | $P_{11}$ | **** | **** | * | | | *** | * | *** |
| $N(1520)$ | $D_{13}$ | **** | **** | *** | | | **** | **** | **** |
| $N(1535)$ | $S_{11}$ | **** | **** | **** | | | * | ** | *** |
| $N(1650)$ | $S_{11}$ | **** | **** | * | *** | ** | *** | ** | *** |
| $N(1675)$ | $D_{15}$ | **** | **** | * | * | | **** | * | **** |
| $N(1680)$ | $F_{15}$ | **** | **** | * | | | **** | **** | **** |
| $N(1700)$ | $D_{13}$ | *** | *** | * | ** | * | ** | * | ** |
| $N(1710)$ | $P_{11}$ | *** | *** | ** | ** | * | ** | * | *** |
| $N(1720)$ | $P_{13}$ | **** | **** | * | ** | * | * | ** | ** |
| $N(1900)$ | $P_{13}$ | ** | ** | | | | | * | |
| $N(1990)$ | $F_{17}$ | ** | ** | * | * | * | | | * |
| $N(2000)$ | $F_{15}$ | ** | ** | * | * | * | * | ** | |
| $N(2080)$ | $D_{13}$ | ** | ** | * | * | | | | * |
| $N(2090)$ | $S_{11}$ | * | * | | | | | | |
| $N(2100)$ | $P_{11}$ | * | * | * | | | | | |
| $N(2190)$ | $G_{17}$ | **** | **** | * | * | * | | * | * |
| $N(2200)$ | $D_{15}$ | ** | ** | * | * | | | | |
| $N(2220)$ | $H_{19}$ | **** | **** | * | | | | | |
| $N(2250)$ | $G_{19}$ | **** | **** | * | | | | | |
| $N(2600)$ | $I_{1\,11}$ | *** | *** | | | | | | |
| $N(2700)$ | $K_{1\,13}$ | ** | ** | | | | | | |
| $\Delta(1232)$ | $P_{33}$ | **** | **** | F | | | | | **** |
| $\Delta(1600)$ | $P_{33}$ | *** | *** | o | | | *** | * | ** |
| $\Delta(1620)$ | $S_{31}$ | **** | **** | r | | | **** | **** | *** |
| $\Delta(1700)$ | $D_{33}$ | **** | **** | b | | * | *** | ** | *** |
| $\Delta(1750)$ | $P_{31}$ | * | * | i | | | | | |
| $\Delta(1900)$ | $S_{31}$ | ** | ** | d | | * | * | ** | * |
| $\Delta(1905)$ | $F_{35}$ | **** | **** | d | | * | ** | ** | *** |
| $\Delta(1910)$ | $P_{31}$ | **** | **** | e | | * | * | * | * |
| $\Delta(1920)$ | $P_{33}$ | *** | *** | n | | * | ** | | * |
| $\Delta(1930)$ | $D_{35}$ | *** | *** | | | * | | | ** |
| $\Delta(1940)$ | $D_{33}$ | * | * | F | | | | | |
| $\Delta(1950)$ | $F_{37}$ | **** | **** | o | | * | **** | * | **** |
| $\Delta(2000)$ | $F_{35}$ | ** | | r | | | ** | | |
| $\Delta(2150)$ | $S_{31}$ | * | * | b | | | | | |
| $\Delta(2200)$ | $G_{37}$ | * | * | i | | | | | |
| $\Delta(2300)$ | $H_{39}$ | ** | ** | d | | | | | |
| $\Delta(2350)$ | $D_{35}$ | * | * | d | | | | | |
| $\Delta(2390)$ | $F_{37}$ | * | * | e | | | | | |
| $\Delta(2400)$ | $G_{39}$ | ** | ** | n | | | | | |
| $\Delta(2420)$ | $H_{3\,11}$ | **** | **** | | | | | | * |
| $\Delta(2750)$ | $I_{3\,13}$ | ** | ** | | | | | | |
| $\Delta(2950)$ | $K_{3\,15}$ | ** | ** | | | | | | |

| | |
|---|---|
| **** | Existence is certain, and properties are at least fairly well explored. |
| *** | Existence ranges from very likely to certain, but further confirmation is desirable and/or quantum numbers, branching fractions, *etc.* are not well determined. |
| ** | Evidence of existence is only fair. |
| * | Evidence of existence is poor. |

to be included in this table, the states must have been seen in at least two independent experimental analyses and the partial wave analyses which extract these states from experimental data must not have large errors. The states are also classified according to a star rating system, also given in Table 2.1. It can be seen that many states have one or two stars and only appear in one or two analyses of the same experimental data, indicating that the nucleon resonance spectrum is still far from being well established.

Comparison of the experimentally observed resonances to those predicted by phenomenological models has led to the "missing resonance problem", the fact that many more states are predicted than are actually observed. In Figures 2.7 and 2.8, experimentally determined $N$ and $\Delta$ resonances below 2200 MeV are shown along with resonances predicted in the Consituent Quark Model of Capstick and Roberts [17]. The discrepancies between the experimental data and the theoretical predictions may reflect something fundamentally lacking in the description of the nucleon by theoretical models or be a result of the difficulty of extracting resonances from current experimental data. The typical lifetime of a nucleon excited state is $\sim 10^{-23}$ s, corresponding to a width of 60-500 MeV. These states can have small separations in mass $\sim$10 MeV, leading to significant overlapping as can be seen from Figure 2.9.

The masses and decay widths of the resonances are extracted from experimental data using model-dependent partial wave analyses and reaction models. This contributes further uncertainty to the excited spectrum of the nucleon. It is therefore possible that many of these "missing" resonances do exist, but that the current world data set is not sufficiently comprehensive to achieve the sensitivity required to disentangle the broad, overlapping excited states. In particular, recent Lattice QCD calculations seem to predict a spectrum of excited states as rich as the Quark Model. Alternatively it may be found that these resonances do not exist in nature, providing important information about the degrees of freedom in the nucleon and non-perturbative QCD.

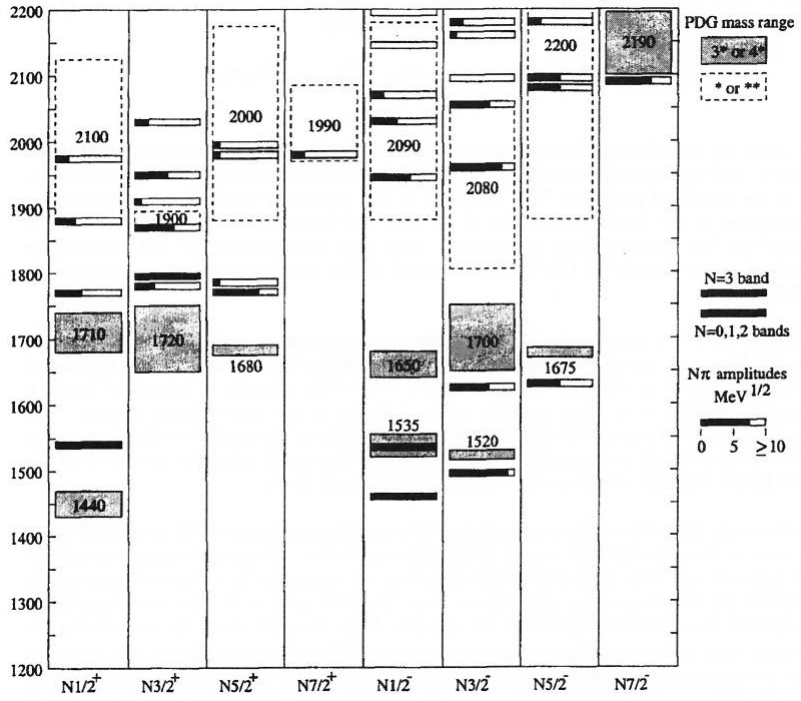


Figure 2.7: Predicted $N$ resonances from the Constituent Quark Model below 2200 MeV shown with PDG mass range values and $N\pi$ decay amplitudes [17].

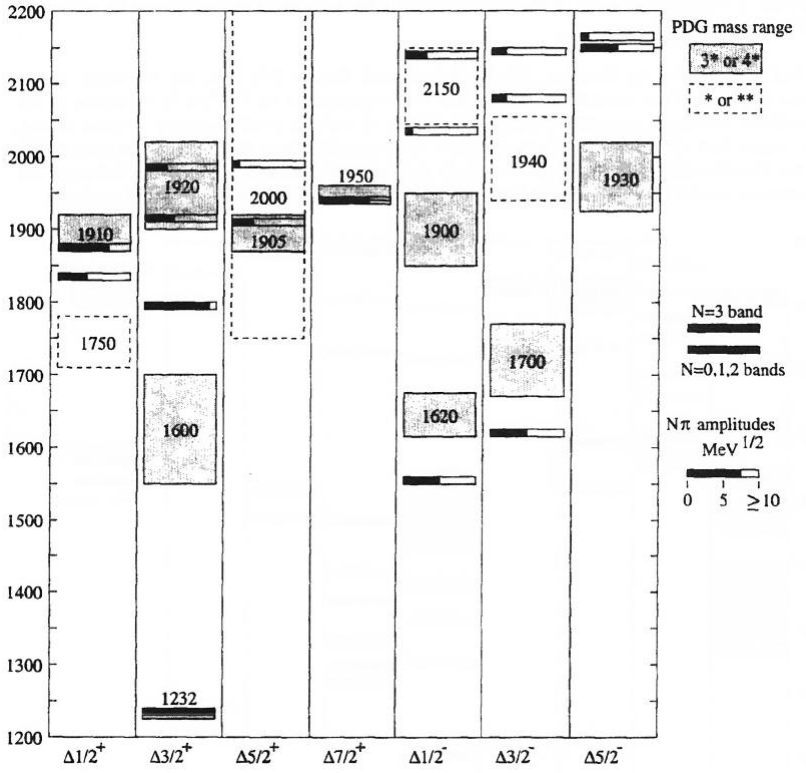


Figure 2.8: Predicted $\Delta$ resonances from the Constituent Quark Model below 2200 MeV shown with PDG mass range values and $N\pi$ decay amplitudes [17].17

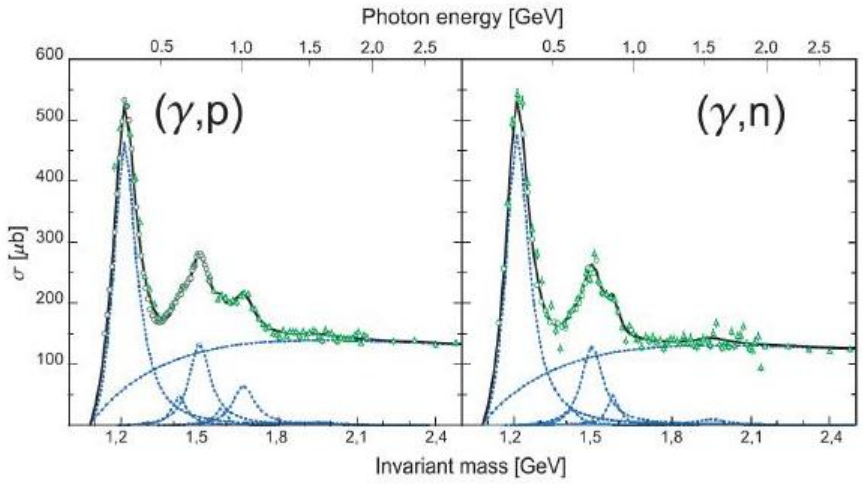


Figure 2.9: Photoabsorption cross section for the proton (above left) and the neutron (above right). The green points are experimental data and the blue curves show the $P_{33}(1232)$, $P_{11}(1440)$, $D_{13}(1520)$, $S_{11}(1535)$, $F_{15}(1680)$ and $F_{37}(1950)$ resonances along with a smooth background [31].

# Chapter 3

# Pion Photoproduction

## 3.1 Kinematics

Figure 3.1 illustrates the pion photoproduction reaction from a stationary nucleon target in the centre-of-mass frame of the photon and nucleon. In this frame the reaction is viewed as the collision of a real photon, $\gamma$, with four-momentum[1], $k$, colliding with a nucleon, $N$, with four-momentum, $p_i$. This results in the production of a baryon $B$, with four-momentum, $p_f$, and a meson, $\pi$, with four-momentum, $q$.

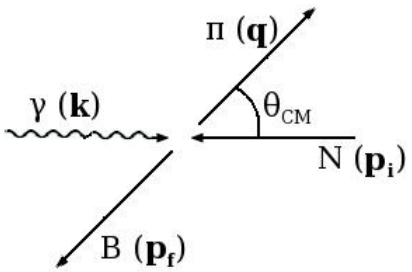


Figure 3.1: Schematic diagram of the photoproduction reaction in the centre-of-mass frame of reference. Symbols are explained in the text.

[1]Four-momentum is defined as a combination of the particle's energy, $E$ and its three-momentum, **p**: *[E,***p***]*.

The collision process can proceed via three possible mechanisms, as shown in the Feynman diagrams in Figure 3.2. The s-channel represents the process in which the photon and the neutron combine to form an intermediate particle which then decays (a resonance). The t- and u-channels represent the emission of an intermediate particle by one of the incident particles which is then absorbed by the other incident particle.

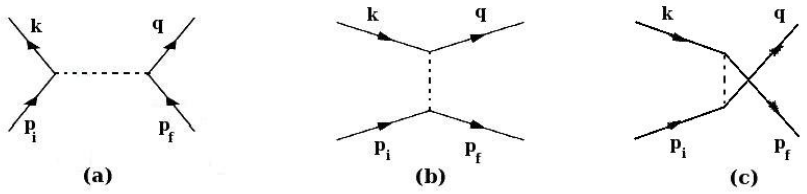


Figure 3.2: Feynman diagrams representing (a) the s-channel process, (b) the t-channel process and (c) the u-channel process.

The square of the four-momentum of each intermediate particle in these diagrams is described by the Lorentz-invariant Mandelstam Variables [32]:

$$s = (k + p_i)^2 = (q + p_f)^2 \tag{3.1}$$

$$t = (p_i - p_f)^2 = (k - q)^2 \tag{3.2}$$

$$u = (p_i - q)^2 = (k - p_f)^2 \tag{3.3}$$

It can be seen from these relations that $s$ is the square of the energy of the reaction, and that $t$ is the square of the momentum transfer and that a linear combination of $s$, $t$, and $u$ will give the sum of the masses of the particles squared:

$$s + t + u = \sum m_i^2 \tag{3.4}$$

The reaction between the photon and the target nucleon can be completely described by two of the three variables, with the $s$ and $t$ channels usually chosen. If the relativistic approximation is taken, where $mc^2 \ll E$, the Mandelstam variables can be expressed as [33]:

$$s = 4p^2 \tag{3.5}$$

$$t = 2p^2(1 - cos\theta) \tag{3.6}$$

$$u = 2p^2(1 + cos\theta) \tag{3.7}$$

where $\theta$ is the pion scattering angle in the centre-of-mass frame. For fixed $s$, therefore, $t$ becomes a linear function of $cos\theta$ and the scattering functions can be described fully in terms of $s$ and $cos\theta$.

## 3.2 Photoproduction Amplitudes

The angular distribution of the meson (pion) produced in the photoproduction reaction can be described by the differential cross-section, written in terms of the complex amplitudes, $A(s,cos\theta)$:

$$\frac{d\sigma}{d\Omega} = |A(s, cos\theta)|^2 \tag{3.8}$$

Quantum mechanically, the initial photon-nucleon state $\langle i|$ can be related to the final meson-baryon state $|f\rangle$ by the scattering matrix, $S$. This represents the probability of the transition from the initial to the final state occuring, and can be expressed using the Bjorken-Drell notation as [34]:

$$S_{fi} = \delta_{fi} - \frac{i}{(2\pi)^2}\delta^4(p_f + q - k - p_i)\left(\frac{m^2}{4E_\gamma E_i E_\pi E_f}\right)^{\frac{1}{2}} T_{fi} \tag{3.9}$$

where $p_i$, $q$, $k$ and $p_f$ are the four-momenta of the particles involved in the reaction as defined in Section 3.1, $m$ is the mass of the nucleon, and $T_{fi}$ is the transmission (T) matrix which relates the initial and final states. As the T-matrix defines the transition (photoproduction) amplitude, the differential cross section can now be expressed as:

$$\frac{d\sigma}{d\Omega} = \frac{q}{k}\sum\left|\frac{m}{4\pi W}T_{fi}\right|^2 \tag{3.10}$$

where the values are summed over all possible photon polarisations and the magnetic quantum numbers of the nucleon states and where $W$ is the invariant mass of the system.

The transmission matrix, $T$, can also be expressed generally in terms of the photon polarisation vector, $\varepsilon_\mu$, and the electromagnetic current, $J_\mu$ [35]:

$$T = \varepsilon_\mu J_\mu \tag{3.11}$$

For meson photoproduction, the transition current, $\mathbf{J}$, can be expressed in terms of the nucleon spin matrix, $\sigma$, the meson unit vector, $\hat{\mathbf{q}}$, and the photon three-momentum, $\hat{\mathbf{k}}$ [36]:

$$\mathbf{J} = \frac{4\pi W}{M}(i\tilde{\sigma}F_1 + (\sigma.\hat{\mathbf{k}})(\sigma \times \hat{\mathbf{q}})F_2 + i\tilde{\mathbf{k}}(\sigma.\hat{\mathbf{q}})F_3 + i\tilde{\mathbf{k}}(\sigma.\hat{\mathbf{k}})F_4) \tag{3.12}$$

where

$$\tilde{\sigma} = \sigma - (\sigma.\hat{\mathbf{q}})\hat{\mathbf{q}} \tag{3.13}$$

$$\tilde{\mathbf{k}} = \hat{\mathbf{k}} - (\hat{\mathbf{k}}.\hat{\mathbf{q}})\hat{\mathbf{q}} \tag{3.14}$$

where $F_i$ are the Chew, Goldberger, Low and Nambu (CGLN) amplitudes, functions of energy and scattering angle. However, as the excited states of the nucleon are functions of spin, parity and isospin, it is most useful to express them in terms of multipoles through a partial wave expansion [36]:

$$F_1 = \sum_{l=0}^{\infty}[lM_{l+} + E_{l+}]P'_{l+1}(cos\theta) + [(l+1)M_{l-} + E_{l-}]\,P'_{l-1}(cos\theta) \tag{3.15}$$

$$F_2 = \sum_{l=1}^{\infty}[(l+1)M_{l+} + lM_{l-}]P'_l(cos\theta) \tag{3.16}$$

$$F_3 = \sum_{l=1}^{\infty}[E_{l+} - M_{l+}]P''_{l+1}(cos\theta) + [E_{l-} + M_{l-}]P''_{l-1}(cos\theta) \tag{3.17}$$

$$F_4 = \sum_{l=1}^{\infty}[M_{l+} - E_{l+} - M_{l-} - E_{l-}]P''_l(cos\theta) \tag{3.18}$$

where $P''_l \cos\theta$ and $P''_l \cos\theta$ are derivatives of Legendre polynomials and $\theta$ is the pion centre-of-mass angle. The terms $E_{l\pm}$ and $M_{l\pm}$ refer to electric or magnetic transitions, where the subscript, $l$, is the orbital angular momentum of the final state.

The incoming photon has a total angular momentum, $L_\gamma$ and the nucleon has a total angular momentum of 1/2, so the resulting spin of the resonant state, $J_{N*}$,

will be [37]:

$$|L_\gamma - \frac{1}{2}| \leq J_{N*} \leq |L_\gamma + \frac{1}{2}| \tag{3.19}$$

while the parity, $\pi_{N*}$ will be given by:

$$\pi_{N*} = \pi_N \pi_\gamma \tag{3.20}$$

where the parity of the incoming photon, $\pi_\gamma$, is *(-1)*$^L$ for an electric multipole and *(-1)*$^{L+1}$ for a magnetic multipole, and the parity of the nucleon, $\pi_N$, is equal to 1.

The spin and parity of the resonant state with respect to the outgoing meson (pion) is given by:

$$|L_\pi - \frac{1}{2}| \leq J_{N*} \leq |L_\pi + \frac{1}{2}| \tag{3.21}$$

and:

$$\pi_{N*} = \pi_N \pi_\pi (-1)^{L_\pi} = (-1)^{L_{\pi+1}} \tag{3.22}$$

where the parity of the meson, $\pi_\pi$, is equal to -1.

Combining equations 3.19 through to 3.22, the spin and parity of the resonance can be expressed in terms of the spins and parities of the initial and final state particles:

$$L_\gamma \pm \frac{1}{2} \leq J_{N*} \leq L_\gamma \pm \frac{1}{2} \tag{3.23}$$

$$\pi_{N*} = \pi_\gamma = (-1)^{L_{\pi+1}} \tag{3.24}$$

As for an electric multipole $L = L_\pi \pm 1$ and for a magnetic multipole $L = L_\pi$, the spin and parity of the resonant states is related to the angular distribution of mesons as the CGLN amplitudes contain the Legendre polynomial terms. When the cross section is dominated by a particular resonance, the quantum numbers of that resonance will be reflected in the angular distributions of particles, with different resonances contributing to different partial waves. Often more than one multipole will contribute to a resonance and so as different reaction channels are sensitive to different resonances, several channels must be measured to disentangle the different resonance contributions.

## 3.3 Photoproduction Amplitudes in the Isospin Representation

Even though electromagnetic interactions do not conserve isospin, the overall isospin of the hadronic interaction must be conserved and can be described as follows. The isospin of the nucleon determines the isospin of the initial state, $I_i$=*1/2*. The isospin of the final state, $I_f$, is a combination of the pion isospin, $I_\pi$=*1*, and the nucleon isospin. As such, $I_f$ = *1/2* or *3/2*. The value of $I_f$ is determined by the photon which behaves as a linear combination of isoscalar, $I_s$, and isovector, $I_v$, particles. The system can now be described in terms of three isospin amplitudes [35]:

$$A^0 =< 1/2, I_3|I_s|1/2, I_3 > \tag{3.25}$$

in the case of an isoscalar photon, and

$$A^1 =< 1/2, I_3|I_v|1/2, I_3 > \tag{3.26}$$

$$A^3 =< 3/2, I_3|I_v|1/2, I_3 > \tag{3.27}$$

in the case of an isovector photon. If we define the following isospin amplitude terms [38]:

$$A^+ = \frac{(A^1 + 2A^3)}{3} \tag{3.28}$$

$$A^- = \frac{(A^1 - A^3)}{3} \tag{3.29}$$

then the physical amplitudes for each of the possible pion photoproduction processes can be expressed as [38]:

$$A(\gamma p \to n\pi^+) =< n\pi^+|I|\gamma p >= \sqrt{2}(A^0 + A^-) \tag{3.30}$$

$$A(\gamma p \to p\pi^0) =< p\pi^0|I|\gamma p >= (A^0 + A^+) \tag{3.31}$$

$$A(\gamma n \to p\pi^-) =< p\pi^-|I|\gamma n >= \sqrt{2}(A^0 - A^-) \tag{3.32}$$

$$A(\gamma n \to n\pi^0) =< n\pi^0|I|\gamma n >= -(A^0 - A^+) \tag{3.33}$$

From these equations it can therefore be seen that to fully disentangle the individual reaction amplitudes, photoproduction measurements on both proton and neutron targets are required.

## 3.4 Photoproduction Amplitudes in the Helicity and Transversity Representations

In addition to requiring both proton and neutron targets, a full experimental understanding of the photoproduction reaction system requires measurements beyond that of the unpolarised differential cross section. This is because the four CGLN structure functions arise from the four possible combinations of photon helicity and nucleon spin. Experiments involving polarised beams and/or polarised nucleon targets are therefore required, with the CGLN structure functions being most easily related to these experiments in terms of helicity or transversity amplitudes.

The t-channel helicity amplitudes $\tau_i$ can be related to the CGLN invariant amplitudes $A_i$ from equations 3.15 to 3.18 by the relations [39]:

$$\tau_1 = -A_1 + 2mA_4 \tag{3.34}$$

$$\tau_2 = A_1 + tA_2 \tag{3.35}$$

$$\tau_3 = 2mA_1 - tA_4 \tag{3.36}$$

$$\tau_4 = A_3 \tag{3.37}$$

where $m$ is the nucleon mass and $t$ is the momentum transfer Mandelstam variable as defined in Section 3.1. These t-channel amplitudes can then be represented in terms of the s-channel helicity amplitudes [39, 35]:

$$\begin{pmatrix} \tau_1 \\ \tau_2 \\ \tau_3 \\ \tau_4 \end{pmatrix} = \frac{-4\sqrt{\pi}}{\sqrt{-t}} \begin{pmatrix} 2m & \sqrt{-t} & -\sqrt{-t} & 2m \\ 0 & \sqrt{-t} & \sqrt{-t} & 0 \\ t & 2m\sqrt{-t} & 2m\sqrt{-t} & t \\ 1 & 0 & 0 & -1 \end{pmatrix} \begin{pmatrix} S_1 \\ N \\ D \\ S_2 \end{pmatrix} \tag{3.38}$$

where $N$ is the no-flip amplitude, $S_1$ and $S_2$ are single-flip amplitudes and $D$ is the double-flip amplitude. By taking linear combinations of these helicity amplitudes, transversity amplitudes can then be defined [40, 35]:

$$b_1 = \frac{1}{2}[(S_1 + S_2) + i(N - D)] \tag{3.39}$$

$$b_2 = \frac{1}{2}[(S_1 + S_2) - i(N - D)] \tag{3.40}$$

$$b_3 = \frac{1}{2}[(S_1 - S_2) - i(N + D)] \tag{3.41}$$

$$b_4 = \frac{1}{2}[(S_1 - S_2) + i(N - D)] \tag{3.42}$$

As can be seen from the equations above, the photoproduction process is fully described by four complex amplitudes. By taking bilinear combinations of the four equations in either the helicity of the transversity formalism, 16 combinations result. Table 3.1 shows these combinations or "polarisation observables" in both helicity and transversity notations along with the type of experiment required to measure them.

The 16 polarisation observables are classified as: the differential cross section, three single-polarisation observables ($P$, $\Sigma$, and $T$) where one of the beam, target or recoil are polarised, and 12 double polarisation observables where two of the three reaction components which can carry polarisation are polarised. The double-polarisation observables themselves are divided into three groups: beam-target ($G$, $H$, $E$, $F$), beam-recoil ($O_x$, $O_z$, $C_x$, $C_z$), and target-recoil ($T_x$, $L_x$, $L_z$).

Experimentally, it is the differential cross section of the meson in the photoproduction reaction that will be measured. For the beam-target measurements, this can be expressed in terms of polarisation observables as [39]:

$$\begin{aligned}\frac{d\sigma}{d\Omega} = \left(\frac{d\sigma}{d\Omega}\right)_{unpolarised} \{1 - P_L \Sigma cos(2\phi) + P_x[-P_L H sin(2\phi) + P_\odot F] \\ -P_y[-T + P_L P cos(2\phi)] - P_z[-P_L G sin(2\phi) + P_\odot E]\}\end{aligned} \tag{3.43}$$

Table 3.1: Table showing the 16 polarisation observables along with their helicity and transversity representations [40]. Note that the axes given for the experiments required follow the Basel Convention: $z$ is in the same direction as the beam, $y$ is normal to the reaction plane, and $z'$ is in the direction of the scattered meson.

| Usual symbols | Helicity representation | Transversity representation | Experiment required[a] |
|---|---|---|---|
| $\sigma/t$ | $\|N\|^2+\|S_1\|^2+\|S_2\|^2+\|D\|^2$ | $\|b_1\|^2+\|b_2\|^2+\|b_3\|^2+\|b_4\|^2$ | $\{-;-;-\}$ |
| $\Sigma$ | $2\Re(S_1^*S_2-ND^*)$ | $\|b_1\|^2+\|b_2\|^2-\|b_3\|^2-\|b_4\|^2$ | $\{L(\frac{\pi}{2},0);-;-\}$ $\{-;y;y\}$ |
| $T$ | $2\Im(S_1N^*-S_2D^*)$ | $\|b_1\|^2-\|b_2\|^2-\|b_3\|^2+\|b_4\|^2$ | $\{-;y;-\}$ $\{L(\frac{\pi}{2},0);0;y\}$ |
| $P$ | $2\Im(S_2N^*-S_1D^*)$ | $\|b_1\|^2-\|b_2\|^2+\|b_3\|^2-\|b_4\|^2$ | $\{-;-;y\}$ $\{L(\frac{\pi}{2},0);y;-\}$ |
| $G$ | $-2\Im(S_1S_2^*+ND^*)$ | $2\Im(b_1b_3^*+b_2b_4^*)$ | $\{L(\pm\frac{\pi}{4});z;-\}$ |
| $H$ | $-2\Im(S_1D^*+S_2N^*)$ | $-2\Re(b_1b_3^*-b_2b_4^*)$ | $\{L(\pm\frac{\pi}{4});x;-\}$ |
| $E$ | $\|S_2\|^2-\|S_1\|^2-\|D\|^2+\|N\|^2$ | $-2\Re(b_1b_3^*+b_2b_4^*)$ | $\{c;z;-\}$ |
| $F$ | $2\Re(S_2D^*+S_1N^*)$ | $2\Im(b_1b_3^*-b_2b_4^*)$ | $\{c;x;-\}$ |
| $O_x$ | $-2\Im(S_2D_2^*+S_1N^*)$ | $-2\Re(b_1b_4^*-b_2b_3^*)$ | $\{L(\pm\frac{\pi}{4});-;x'\}$ |
| $O_z$ | $-2\Im(S_2S_1^*+ND^*)$ | $-2\Im(b_1b_4^*+b_2b_3^*)$ | $\{L(\pm\frac{\pi}{4});-;z'\}$ |
| $C_x$ | $-2\Re(S_2N^*+S_1D^*)$ | $2\Im(b_1b_4^*-b_2b_3^*)$ | $\{c;-;x'\}$ |
| $C_z$ | $\|S_2\|^2-\|S_1\|^2-\|N\|^2+\|D\|^2$ | $-2\Re(b_1b_4^*+b_2b_3^*)$ | $\{c;-;z'\}$ |
| $T_x$ | $2\Re(S_1S_2^*+ND^*)$ | $2\Re(b_1b_2^*-b_3b_4^*)$ | $\{-;x;x'\}$ |
| $T_z$ | $2\Re(S_1N^*+S_2D^*)$ | $2\Im(b_1b_2^*-b_3b_4^*)$ | $\{-;x;z'\}$ |
| $L_x$ | $2\Re(S_2N^*-S_1D^*)$ | $2\Im(b_1b_2^*+b_3b_4^*)$ | $\{-;z;x'\}$ |
| $L_z$ | $\|S_1\|^2+\|S_2\|^2-\|N\|^2-\|D\|^2$ | $2\Re(b_1b_2^*-b_3b_4^*)$ | $\{-;z;z'\}$ |

[a] Notation is $\{P_\gamma;P_T;P_R\}$ where:
$P_\gamma$ = polarisation of beam,
$L(\theta)$ = beam linearly polarised at angle $\theta$ to scattering plane,
$C$ = circularly polarised beam;
$P_T$ = direction of target polarisation;
$P_R$ = component of recoil polarisation measured.

Similarly for the beam-recoil measurements [39]:

$$\rho_f \frac{d\sigma}{d\Omega} = \left(\frac{d\sigma}{d\Omega}\right)_{unpolarised} \{1 + \sigma_y P - P_L cos(2\phi)(\Sigma + \sigma_y T) \\ -P_L sin(2\phi)(O_x\sigma_x + O_z\sigma_z) - P_\odot(C_x\sigma_x + C_z\sigma_z)\} \tag{3.44}$$

and for the target-recoil measurements [39]:

$$\rho_f \frac{d\sigma}{d\Omega} = \left(\frac{d\sigma}{d\Omega}\right)_{unpolarised} \{1 + \sigma_y P + P_x(T_x\sigma_x + T_z\sigma_z) \\ +P_y(T + \Sigma\sigma_y) - P_z(L_x\sigma_x - L_z\sigma_z)\} \tag{3.45}$$

where $P_x$, $P_y$, $P_z$ are the degrees of target polarisation along the $x$, $y$, $z$ axes, $P_\odot$ and $P_L$ are the degrees of circular and linear beam polarisation respectively, and $\phi$ is the direction of transverse linear beam polarisation with respect to the scattering plane. Here $\rho_f$ is the density matrix of the recoil nucleon and is given by:

$$\rho_f = \frac{1}{2}(I + \sigma.\mathbf{P_f}) \tag{3.46}$$

where $\mathbf{P}_f$ is the polarisation of $\rho_f$.

## 3.5 The "Complete" Experiment

A central aim of the current generation of meson photoproduction experiments currently being performed is therefore to obtain a "complete" set of measurements which will fully constrain the reaction amplitudes. By measuring the differential cross section plus all three single-polarisation observables, the magnitude of the transversity amplitudes can be fully determined. However, the phase cannot be unambiguously determined without the measurement of double-polarisation observables.

There is still some debate as to how many observables must be measured in order to achieve this. The 1975 paper of Barker, Donnachie and Storrow (BDS) [40] was the first to attempt to definitively answer this question. They showed

that five double-polarisation observables were required, provided that no more than four of these measurements come from the same group of beam-target, beam-recoil or target-recoil. Keaton and Workman [41], however, were able to show that some of the combinations of measurements which satisfy the conditions proposed by BDS still result in an ambiguous solution. Chiang and Tabakin [42] agreed with the Keaton and Workman result, but concluded that only four carefully selected double-polarisation observables in conjunction with the differential cross section and the three single- polarisation observables, are enough to fully determine the transversity amplitudes. As the Chiang and Tabakin selection rules are much more complicated than those of BDS, the reader is referred to Reference [42] for further details and proofs.

## 3.6 Extraction of Resonance Parameters from Data

Reaction models have been developed in order to extract the amplitudes, widths and masses of resonances from experimental data. In general, these involve separating the transmission matrix into its background and resonant contributions, parameterising these terms and then finding these parameters through fits to experimental data.

If the reaction $a \rightarrow c \rightarrow b$ is considered, where $a$ is the inital nucleon-photon system, $b$ is the final nucleon-meson system, and $c$ is the intermediate resonant state, the Hamiltonian describing the photoproduction system can be written as:

$$H = H_0 + V \tag{3.47}$$

where $H_0$ is the free Hamiltonian, a sum of the kinetic energy operators in the system, and $V$ is the interaction term. The interaction term itself can be described in terms of a background contribution, $V_{BG}$, and a resonant term, $V_R(E)$, which describes the resonance as function of the total energy of the system:

$$V = V_{BG} + V_R(E) \tag{3.48}$$

The background contribution arises from the $\gamma N$ interaction producing a meson,

but without producing an intermediate resonant state. The transmission matrix, $T_{ab}$, can now be expressed as:

$$T_{ab}(E) = V_{ab} + \sum_{c} V_{ab} g_c(E) T_{cb}(E) \tag{3.49}$$

where $\sum_{c}$ represents the sum over all possible paths from states $a$ to $b$ via $c$, and $g_c$ is the propagator of channel $c$. The transmission matrix can also be split into its separate background and resonance contributions:

$$T_{ab} = t_{ab}^{BG} + t_{ab}^{R}(E) \tag{3.50}$$

### 3.6.1 Partial Wave Analyses

Partial wave analyses (PWA) decompose the background and resonant contributions of the transmission matrix into into a series of partial waves of definite angular momentum and multipoles. The background terms are in general modelled by Born terms and vector-meson contributions, while a Breit-Wigner curve is assumed for the resonant contribution. The parameters of the analysis are obtained through a two-step fitting process to current experimental data. The first stage is to perform a global fit in order to determine the phases of the multipoles. The second stage is to perform a local fit to the data divided in 10-20 MeV wide energy bins in order to determine the absolute values of the multipoles. In this second stage, the absolute values are varied, while the phase determined from the global fit is kept constant, until good agreement is obtained between the local and global fits. Certain resonances can be added or removed from the fit, indicating the sensitivity of the resonances to certain multipoles.

There are two main partial wave analyses relevant to pion photoproduction: MAID developed at the University of Mainz [43] and SAID developed by the CNS Data Analysis Centre at George Washington University [44].

The MAID PWA is a unitary isobar model based on a T-matrix of the form [45]:

$$T_{\gamma\pi}(E) = V_{\gamma\pi}(E) + V_{\gamma\pi}(E) g_0(E) T_{\pi N}(E) \tag{3.51}$$

where $V_{\gamma\pi}$ is the transition potential for the $\gamma N \rightarrow \pi N$ reaction, $T_{\pi N}$ is the $\pi N$

scattering matrix and $g_0$ is the free $\pi N$ propagator. Here the transition potential and scattering matrix can be decomposed into its resonant and background terms which are expanded as partial waves. The data used in the MAID fit include only resonances below 2 GeV which are classed as 4* by the Particle Data Group [1], with the latest version, MAID2007, including 13 resonances [45]. As such, the main limitation of the PWA is that it is only valid up to 2 GeV.

Unlike MAID, the SAID PWA makes no assumptions about resonant contributions nor the channels which should be included in the analysis. The T-matrix is defined for the $\gamma N$, $\pi N$ and $\pi\Delta$ channels, the latter representing all other open channels [46]:

$$T_{\gamma\pi} = A_I(1 + iT_{\pi N}) + A_R T_{\pi N,\pi N} \tag{3.52}$$

$A_I$ parameterises the background and $A_R$ parameterises the resonant terms. The background terms are of the form [46]:

$$A_I = A_B + A_Q \tag{3.53}$$

a combination of pseudoscalar Born amplitudes and Legendre polynomials. The resonant contribution, $A_R$, is of the form [46]:

$$A_R = \frac{\mu}{q}\left(\frac{k}{q}\right)^l \sum_{n=0}^{N} \frac{p_n}{\mu}\left(E_\gamma - \mu\left[1 + \frac{\mu}{2m}\right]\right) \tag{3.54}$$

where $\mu$ is the pion mass, $E_\gamma$ is the photon lab energy, $m$ is the nucleon mass as before, and $q$ and $k$ are the pion momentum and the photon momentum in the centre-of-mass frame respectively as before. The parameter $p_n$ is determined in a fit to experimental data.

Overall, the two partial wave analyses are very similar, with their differences arising from the specific treatment of the background terms and the channels included in the fits. In general, good agreement for measured observables is achieved at lower energies $\leq$1 GeV, but differences arise in the second and third resonance regions [47]. However, significant discrepancies for poorly measured observables exist even for the low-lying regions of the nucleon excitation spectrum. This suggestes that the PWA are underconstrained by the available experimental data, the $G$ observable being one example of this. A full description of these PWA is beyond the scope of this thesis, with the reader being referred to References [43]

and [45] for further details about MAID and References [44] and [46] for further details about SAID.

### 3.6.2 Dynamical Reaction Models

Dynamical reaction models take into account off-shell scattering effects such as the case where a meson could be produced in a non-resonant reaction and then re-scattered off the nucleon to produce a resonance. The Hamiltonian for the photoproduction system is separated into terms taking into account the pure meson baryon-states, the pure constituent quark states and the quark core with a meson cloud. The interaction is described in terms of well-known meson exchange contributions and phenomenological two-body separable potentials for multiple scattering. Coupled channel analyses extend dynamical reaction models by simultaneously taking into account the electromagnetic and strong interactions for all meson photoproduction channels. One of the main coupled-channel analyses relevant to this thesis is the Bonn-Gatchina model, developed by the University of Bonn and the Petersburg Institute of Nulcear Physics in Gatchina [48]. This analysis takes into account $\pi N$ and $kN$ scattering as well as photoproduction data with two or more mesons in the final state, including in total 65 different reactions [49]. And unlike MAID and SAID, fits are performed as a function of energy and angle simultaneously. For further information the reader is referred to References [49], [50] and [51].

## 3.7 Summary

Pion photoproduction experiments using both polarised beams and polarised targets provide crucial information regarding the photoproduction scattering amplitudes through polarisation observables. Double-polarisation observables, such as the measurement of the $G$ observable presented in this thesis, are vital to move closer to the "complete experiment" which will provide all the necessary data to fully constrain these amplitudes. Reaction models such as the MAID and SAID partial wave analyses extract resonance parameters from the experimental data, the results of which can then be compared to theoretical predictions. These comparisons provide valuable information about the dynamics and degrees of freedom of the constituents of the nucleon.

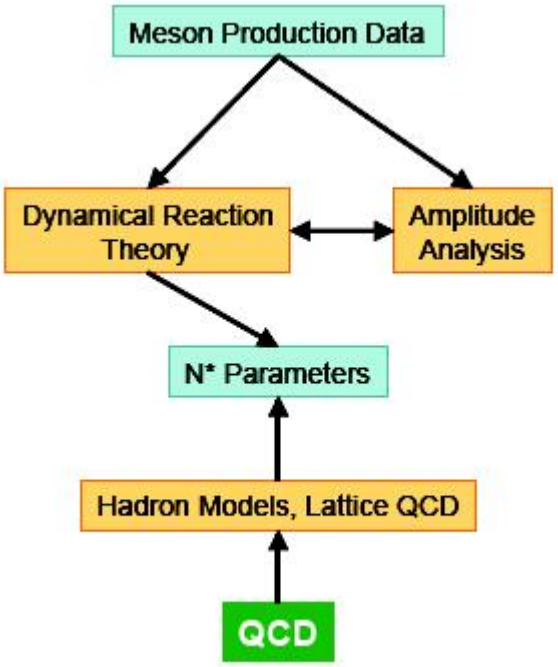


Figure 3.3: Flow chart summarising the links between each stage of the study of nucleon resonances, from photoproduction experiments and extraction of the resonances from experimental data, to theoretical treatment with QCD and phenomenological models of the nucleon [52].

# Chapter 4

# Previous Measurements

## 4.1 Overview

The development of electron accelerators above 500 MeV in the late 1940s and 1950s provided a new window into the structure of nuclei and nucleons and were used extensively in elastic scattering reactions. These machines were also capable of producing photons of around 300 MeV, allowing pioneering meson photoproduction reactions to be studied at Berkeley, Cornell, MIT and later Caltech [53]. By the 1970s, research was being focused on experimentally achieving a "complete" set of accurate measurements to extract the resonance spectrum in a partial wave analysis [54]. However the available beam quality, as well as a lack of hermetic detectors and polarised targets, left a data set far from the completeness or quality required, with only the single-polarisation observables easily accessible. In spite of this long history, the current contribution to the world data set from this period of measurement is dominated by unpolarised cross sections at lower energies.

In the past 20 years, the development of continuous wave accelerators, such as CEBAF at Jefferson Lab, ELSA in Bonn, GRAAL in Grenoble, MAMI in Mainz and Spring8 in Osaka [37] has allowed the world data set for meson photoproduction to nearly double. Also necessary for the improvement in the data available were the advances in detector technology, in particular with respect to spatial and energy resolutions and also nearly full angular coverage [55]. The development and improvement of polarised beams, targets and polarimeters has also greatly increased the potential of polarised photoproduction experiments.

Ongoing research at Jefferson Lab Hall B [56]-[60], the CB-ELSA experiment at Bonn [61, 62] from 2006-2007, and the Crystal Ball Experiment at MAMI in Mainz from 2009-2010 [63]-[70] aim to provide such data by measuring both single and double polarisation observables in meson photoproduction. It is hoped that these programmes using the complementary detectors and beam characteristics at each facility can provide a complete set of measurements to make close to "model independent" analyses of the photoproduction amplitudes possible.

## 4.2 Previous measurements of the *G* Double Polarisation Observable

Three previous experiments have measured the $G$ double polarisation observable for the $\gamma(p,n)\pi^+$ reaction in the energy range 320 MeV to 1875 MeV, a brief description of which will be provided in the remainder of this chapter. These experiments provide a total of 84 data points. However, only the experiment performed by Bussey *et al.* in 1980 [71] provides experimental data within the range of energies studied in this thesis, which is still a total of 76 data points.

Bussey *et al.* [72, 71] made the first measurements of the $G$ and $H$ double-polarisation observables in two experiments measuring neutral and positive pion photoproduction on the proton in 1979 and 1980 using the NINA electron synchrotron at Daresbury Laboratory. For the $\pi^+ n$ channel, these observables were measured for photon energies between 600 MeV and 1875 MeV at pion centre-of-mass angles between $30^0$ and $100^0$ [71].

The linearly polarised photon beam was produced using coherent Bremsstrahlung from a diamond radiator with beam polarisation typically between 40% and 60% [71], and the flux on target being measured by a pair spectrometer. If the butanol target was polarised both longitudinally and transversely, with the photon beam polarised at $\pm 45^0$ to the horizontal reaction plane in which the outgoing particles are detected, the differential cross section in Equation 3.43 reduces to:

$$\frac{d\sigma}{d\Omega} = \left(\frac{d\sigma}{d\Omega}\right)_{unpolarised} (1 \pm p_\gamma p_z G \mp p_\gamma p_x H) \tag{4.1}$$

allowing both $H$ and $G$ to be measured separately when $p_z$ and $p_x$ are set to zero

respectively.

The outgoing $\pi^+$ were detected by a magnetic spectrometer, $\pi^+$ events being separated from proton events using a Cherenkov Counter. In contrast with the experiment presented in this thesis, the neutron was directly detected using an array of plastic scintillator blocks and a 5cm-thick lead absorber as the Bussey *et al.* measurement required the photon energy to be reconstructed from the final state reaction kinematics in the absence of a tagged-photon beam.

The angular range over which the $\pi^+$ and neutron were detected was severely limited by the superconducting coils of the polarised target, a common problem before the introduction of frozen spin targets. In order to maximise the scattering angle, the orientation of the coils and hence the polarisation of the target had to be such that a mixture of the $G$ and $H$ observables contributed to the measured asymmetries. Target polarisations between 50% and 60% were achieved with this polarisation orientation.

A further complication introduced by the polarised target was that outgoing charged particles were deflected from the horizontal reaction plane, resulting in small components of the $\Sigma$, $P$ and $T$ observables being present in the asymmetries. Values for these observables obtained in previous experiments by Bussey *et al.* were introduced as small correction terms.

Bussey *et al.* found that their results were consistent with the expectations for the $G$ and $H$ observables available at that time (the multipole and amplitude analyses of Barbour *et al.* [73]), as shown in Figure 4.1. However, as will be seen in Figures 10.2 to 10.8, where the Bussey *et al.* results are plot alongside the values of $G$ obtained for this thesis and the current MAID, SAID and Bonn-Gatchina solutions, the Bussey *et al.* results are inconsistent with more modern expectations. Even though the work of Bussey *et al.* still provides the vast majority of experimental data available for the $G$ observable, these data cannot differentiate between the three PWA solutions with little or no agreement above a photon energy of 1600 MeV. In addition, the statistical and systematic uncertainties of these data mean that they do not have significant influence on these solutions.

Belyaev *et al.* [74] were the first group to measure the $G$ double polarisation observable for positive pion photoproduction in the region of the first $\Delta(1232)$ resonance in 1984, measuring both the $G$ and $H$ observables at photon energies

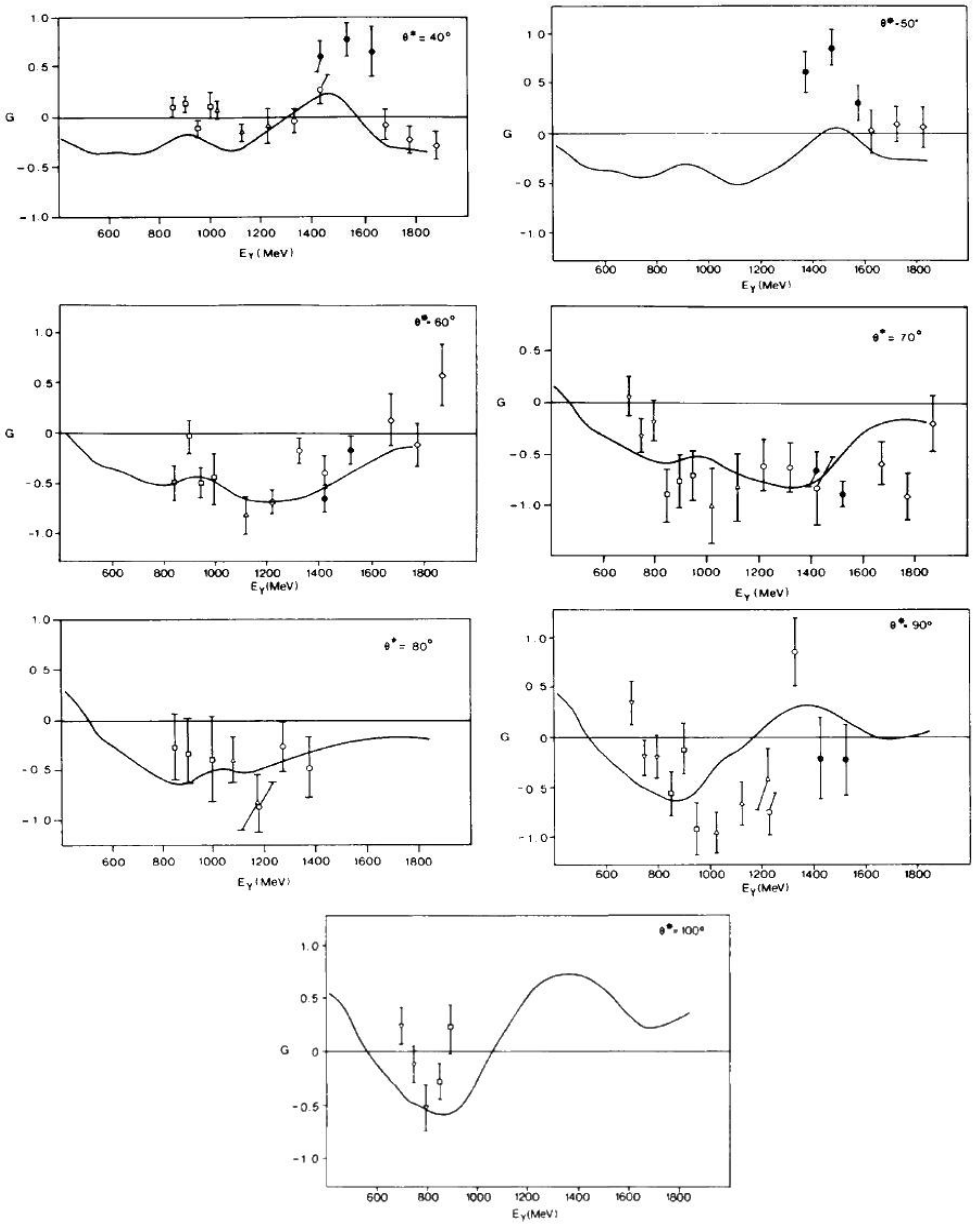


Figure 4.1: Values of the $G$ observable obtained by Bussey *et al.* [71] for the $n\pi^+$ channel plot as a function of photon energy for various pion centre-of-mass angles. The different symbols indicate data taken at different photon beam settings. The solid black line corresponds to the multipole and amplitude analyses of Barbour *et al.* [73].

of 320 MeV, 350 MeV and 380 MeV. Their experiment was carried out using the electron linear accelerator of the Khar'kov Physicotechnical Institute, Ukraine. A linearly polarised photon beam was produced by the coherent Bremsstrahlung technique on a thin diamond radiator, which was then focused onto a polarised propylene glycol target. As for the Bussey *et al.* experiment, the beam was polarised at $\pm 45^0$ to the horizontal reaction plane, although no value of beam polarisation was quoted in the Belyaev *et al.* paper. The target polarisation reached $\sim$70% [74]. Only the outgoing charged particles were measured using Cherenkov Counters and scintillation counters located in the focal plane of two magnetic spectrometers located at $90^0$ to each other.

As for the previous work, the polarised target introduced certain complexities to the data analysis. Again, both $G$ and $H$ contributed to the measured $\pi^+$ distributions as the target was not polarised in a purely linear or transverse direction; this time the orientation was deliberately chosen so that the direction of the axis of the magnetic coils would not have to be changed during the experiment [74]. Today, the general practice is to construct two separate magnetic coils to create purely longitudinal and purely transverse magnetic fields. The positioning of the spectrometers allowed pairs of measurements to be taken at each energy and angle, allowing the contributions of $G$ and $H$ to be separated out. In more modern experiments, large acceptance detectors are used to separate the different spin observables. In addition, the magnetic field of the target coils deflected particles from the reaction plane, so small components of the $\Sigma$ and $P$ asymmetries were present. Again, previous values of these observables had to be included as correction terms, which Belyaev *et al.* stated as a supplementary source of error.

Only four data points were obtained for the $G$ observable: three at a $\pi^+$ centre-of-mass angle of $65^0$ and photon energies 320 MeV, 350 MeV and 380 MeV, and one at a photon energy of 350 MeV and a $\pi^+$ centre-of-mass angle of $80^0$. These were compared to the multipole analyses of Metcalf and Walker [75] and Fëller *et al.* [76], providing reasonable agreement with the predictions.

The most recent measurement of the $G$ observable in pion photoproduction was carried out by Ahrens *et al.* [77] using the Glasgow-Mainz photon tagging facility at the Mainz Microtron, MAMI, in 2005. This was a test measurement for both positive and neutral pion photoproduction carried out for a photon energy

of 340±14 MeV, a precise measurement of $G$ in the energy range 250 MeV to 800 MeV being proposed with the Crystal Ball at MAMI [68].

The Ahrens *et al.* experiment used a diamond radiator to produce a linearly polarised photon beam at $\pm 45^0$ to the horizontal plane, achieving polarisations of 50%. Unlike any of the previous measurements of $G$, a butanol frozen spin target was used, which achieved polarisations of up to 88% [77]. This was the first time a frozen spin target had been used for the measurement of $G$, greatly improving the value of proton polarisation and the length of time that the target remained polarised (200 hours [77] compared to 2 hours for Bussey *et al.* [71]). Additionally frozen spin targets use much smaller magnetic coils, thus having little effect on the reaction products' trajectories and allowing almost all of the $\sim 4\pi$ coverage of the detector to be used. Unlike the previous measurements of $G$, the direction of target polarisation was purely longitudinal and so a "pure" measurement of the $G$ observable was obtained.

For the $n\pi^+$ channel, only the outgoing $\pi^+$s were detected by the DAPHNE detector, consisting of multiwire proportional chambers, segmented plastic scintillators and a scintillator-absorber sandwich. Two additional detectors were located at more forward angles: the MIDAS silicon microstrip detector array and an aerogel Cherenkov Counter.

The values of $G$ obtained by Ahrens *et al.* are in good agreement with recent MAID and SAID solutions and also with the experimental values of Belyaev *et al.*, as can be seen in Figure 4.2. However, as only six data points were measured no preference for either the MAID or SAID analyses can be observed.

In addition to the experiment presented in this thesis, a measurement of the $G$ double polarisation observable is currently being carried out by the CBELSA-TAPS collaboration [61, 62]. This forms part of their current experimental programme to make precise meson photoproduction measurements up to 2500 MeV [61] using the ELSA electron accelerator and the Crystal Barrel detector at the University of Bonn. So far only preliminary values for the $G$ and $\Sigma$ observables have been extracted for the $\gamma(p,p)\pi^0$ and $\gamma(p,p)\eta$ reaction channels.

With respect to the literature, it is evident that a new measurement of the $G$ observable is required for positive pion photoproduction at a large range of energies and angles. The current world data set cannot distinguish between the two main partial wave analyses, and more precise data is needed for all

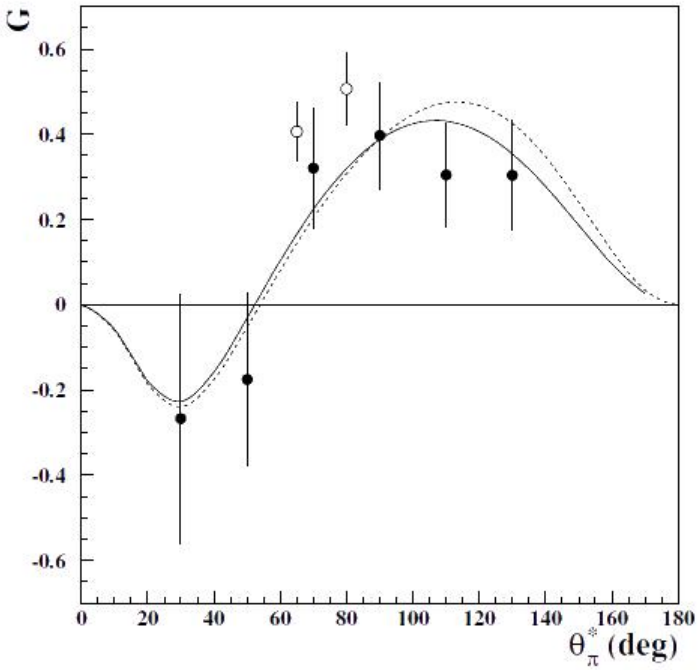


Figure 4.2: Values of the $G$ observable obtained by Ahrens *et al.* [77] (solid black circles) for the $n\pi^+$ channel plot as a function pion centre-of-mass angle for a photon energy of 350 MeV. The solid line shows the MAID2003 prediction [43] and the dashed line shows the SAID-FA04K prediction [44]. The hollow circles show the previous measurement of Belyaev *et al.* [74].

regions of the resonance spectrum in order to constrain the PWA analyses. The experiment presented in this thesis aims to provide high statistics measurements of the $G$ observable for this channel between photon energies of 730 and 2300 MeV corresponding to centre-of-mass energies 1400 to 2280 MeV, and pion centre-of-mass angles between -$180^0$ and $180^0$. This will extend the current contribution to the world data at higher energies by 405 MeV, providing the first data in new regions of the resonance spectrum. At all the sampled energies the new data will greatly extend the angular range, over which $G$ is determined providing a new level of constraint on the partial wave analyses.

# Chapter 5

# Experimental Facility

The aim of this chapter is to outline the experimental setup used for the experiment. The CEBAF accelerator at Jefferson Lab will be described, followed by the production of the linearly polarised photon beam required to measure the $G$ double-polarisation observable and the CLAS detector used to detect the reaction products. The Frozen Spin Target, FROST, which is central to this thesis work, will be presented in detail in the next chapter.

## 5.1 The Thomas Jefferson National Accelerator Facility

The Continuous Electron Beam Accelerator Facility (CEBAF) provides high intensity electron beams of up to 6 GeV and with approximately 100% duty cycle to three experimental halls: A, B and C. An upgrade to 12 GeV will be completed in 2014 and a fourth hall, D, is currently under construction [78]. Halls A and C use high luminosity electron beams to perform scattering experiments to study the electromagnetic and weak neutral current structure of nuclei [79, 80]. Hall D will use high energy photon beams and a solenoid detector to perform meson spectroscopy experiments and to test the current understanding of quark confinement [78]. Hall B houses the CEBAF Large Acceptance Spectrometer (CLAS), which is used with both electron and photon beams in nuclear and hadron physics experiments. A schematic diagram of Hall B with all its major components is shown in Figure 5.2.

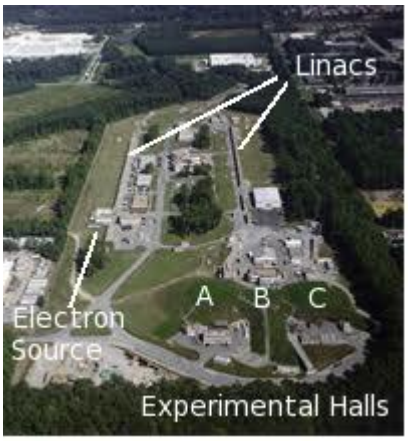


Figure 5.1: Aerial photograph of the Thomas Jefferson National Accelerator Facility showing portions of the CEBAF accelerator and the current three experimental halls [81].

## 5.2 CEBAF

The CEBAF accelerator consists of two anti-parallel superconducting RF-linacs connected by recirculation arcs to create a racetrack configuration with a total length of ∼1.4 km as shown schematically in Figure 5.3. The accelerator produces a continuous-wave electron beam which can circulate around the linacs up to five times, gaining ∼1.2 GeV of energy with each pass. The beam is referred to as "continuous" as the electrons are delivered in short, picosecond pulses at 2.005 ns intervals as shown in Figure 5.4.

## 5.3 The electron source

The electron beam delivered to all three halls originates from the same polarised source, one of two 100 kV GaAs electron guns [84] mounted at $15^0$ to the injector axis [85]. To induce photo-electron emission, three independent lasers (one for each hall) illuminate the cathode of the electron gun with circularly polarised light in short bursts of 499 MHz, the frequency being locked to the accelerator frequency. The three-laser system allows for independent control over the beam provided to the three experimental halls as laser intensity, polarisation and wavelength can be different for all three lasers. The photo-electrons are longitudinally polarised, the degree of longitudinal electron-beam polarisation

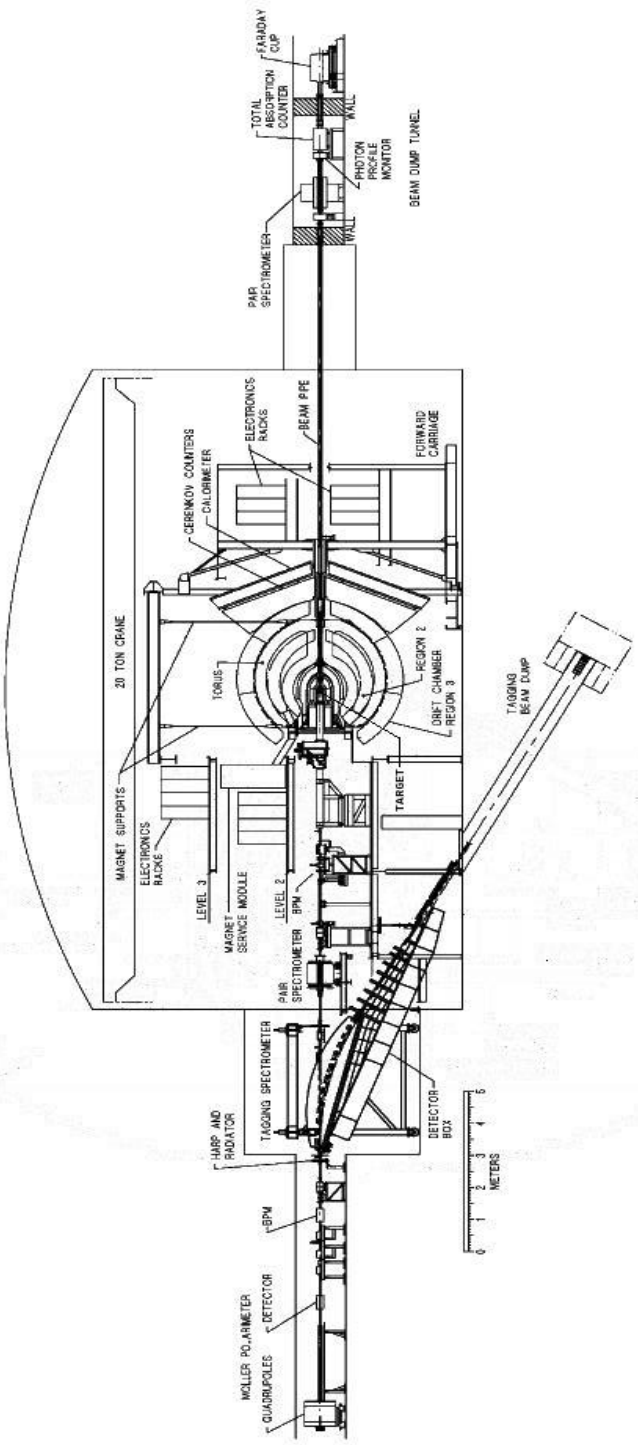


Figure 5.2: Detailed schematic diagram of the Hall B beamline [82].

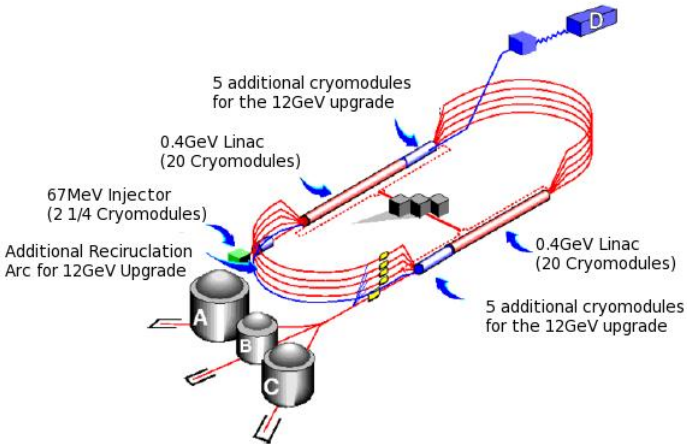


Figure 5.3: Schematic diagram of the CEBAF accelerator, showing the linacs, recirculation arcs and experimental halls. The additions being made for the 12GeV upgrade are also shown [78].

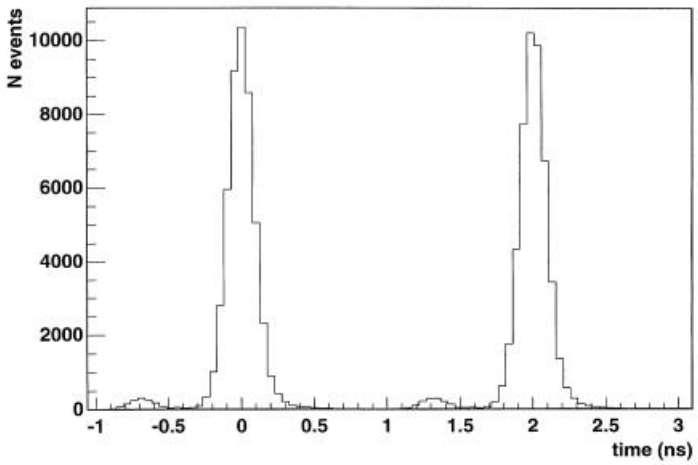


Figure 5.4: Beam bunches arriving in Hall B with 2.005 ns intervals. The smaller peaks correspond to beam being delivered to one of the other experimental Halls [83].

being related to the degree of circular laser-beam polarisation as well as the cathode material and the incident photon wavelength.

The beam leaving the photocathode then passes through a $15^0$ bending magnet to deflect the electrons onto the photoinjector axis, where beam passes through a Wien filter to orient the electron polarisation. The electron beam is now focused as it traverses several metres of magnetic solenoids. Each solenoid is divided into two sections, with equal and opposite longitudinal fields, allowing the beam to be focused without a net rotation of its transverse polarisation component. An RF chopping system ensures that the electron beam has the required bunch structure. The "chopper" consists of two 499 MHz RF deflecting-cavities with a three-slit copper plate between them. The first cavity sweeps the electron beam in a circle across the copper plate where it passes through the slits which are arranged $120^0$ apart. The second cavity then returns the bunched beam to its original path. The beam can then be accelerated to 67 MeV by the injector cryomodules before entering the linacs.

## 5.4 The linacs and recirculation

In the linacs the electrons are accelerated by 160 superconducting niobium RF cavities, cooled by liquid He to $\sim$2.08 K [86]. The cavities are hermetically paired to form "cryounits" as shown in Figure 5.5. Four cryounits make up one, eight-cavity cryomodule. Each linac contains 20 of these cryomodules, with a "warm section" between each one, containing the beam vacuum pipe, vacuum pumps, valves, and the steering dipoles.

On leaving the linac, the electrons enter the recirculation beam lines where the beam is bent by $180^0$ before entering the second linac. There are nine recirculation beam lines in total: five in the first recirculation arc and four in the second [86]. In the linacs, the electrons of different energy can occupy the same beamline. However, in the recirculations arcs, electrons of different energies require a different magnetic field strength to achieve the same bending radius. The electrons therefore pass through an optical spreader which allows electrons of different energies to spread out vertically and enter individually energy-tuned recirculation arcs. Lower energy electrons enter the top arc, with higher energy electrons entering the bottom arc. The electrons then pass through a recombiner

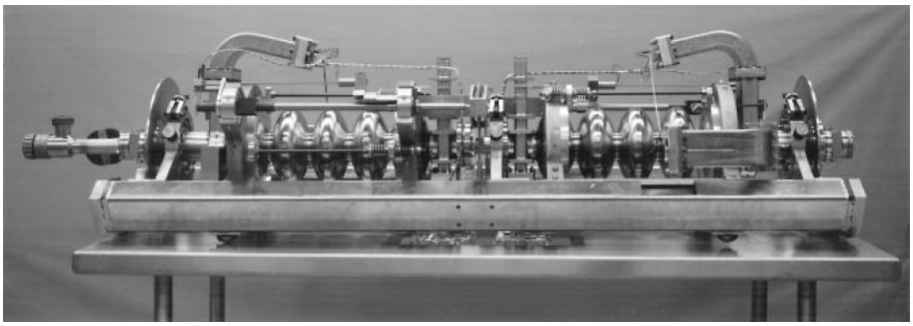

Figure 5.5: Photograph showing a typical CEBAF RF cavity pair or "cryounit" [86].

(a mirror image of the spreader) where individual beams from the arc beamlines are phase matched to the next linac.

## 5.5 Beam extraction

Beam extraction into the three experimental halls occurs at the end of the south linac. Here, nine separator cavities positioned in each of the five recirculation arcs are able to produce a 100 $\mu$rad "kick" to any one pass [87] in order to deflect the beam to the halls. Beam is provided to all three halls simultaneously, with each hall able to receive beam at maximum energy or individual halls are able to extract the beam at a lower energy.

## 5.6 Measurement of beam parameters

In order to successfully provide beam that can be used by the experiments of all three halls, several beam parameters must be known and monitored either continuously or on a regular basis: beam position, beam current, beam profile and beam polarisation.

### 5.6.1 Beam position

Beam position and intensity are continuously monitored using resonant RF cavities as beam position monitors (BPMs) at various locations along the

beamline. For Hall B, these are situated 36.0, 24.6 and 8.2 m upstream of CLAS [82]. A beam lying exactly along the orbit will not induce any oscillation in the cavity. However, if the beam is displaced, its electric field will induce an oscillation which is proportional to the offset in position. The information provided by the BPMs is then used in a feedback loop to keep the beam on target.

#### Beam Current

Beam current is measured in several places throughout the accelerator system. Two Faraday Cups in the injector measure beam current as part of beam set up and for detection of beam condition changes. Two beam-current monitors measure current at the end of the accelerator to determine and limit beam losses. Finally, each hall monitors the beam current delivered to the target. In Hall B, the Faraday Cup used to measure the beam current is also used as the beam dump. This consists of a 4000 kg block of lead placed on ceramic supports inside a vacuum at the end of the beamline, 29 m downstream of CLAS [82]. By stopping the beam, the Faraday cup accumulates charge which can then be drawn off and measured to provide an online monitor of beam current.

### 5.6.2 Beam profile

Wire scanners, called harps, are used to measure the beam profile. Each consists of 20 and 50 $\mu$m tungsten and 100 $\mu$m iron wires which are perpendicular to each other and to the direction of the beam. The wires are driven through the beam at $45^0$ with respect to the horizontal axis by a stepper motor. This allows both X and Y profiles to be measured simultaneously, an example of which is shown in Figure 5.6. The electron beam then scatters from the wire, mainly through the Bremsstrahlung or Møller-scattering processes. PMTs located 5 m downstream of the harp are used to detect the Cherenkov light produced by the scattered electrons as they pass through the glass windows of the PMTs. The beam profile is then produced by correlating the position of the wire scanner and the count rate in the four PMTs which are located top, bottom, beam left and beam right. There are three harps located in the Hall B beamline 36.7, 22.1 and 15.5 m upstream of CLAS [82]. This is a destructive technique, so the measurement is taken only when beam energy is changed or when beam is restored after a long interruption.

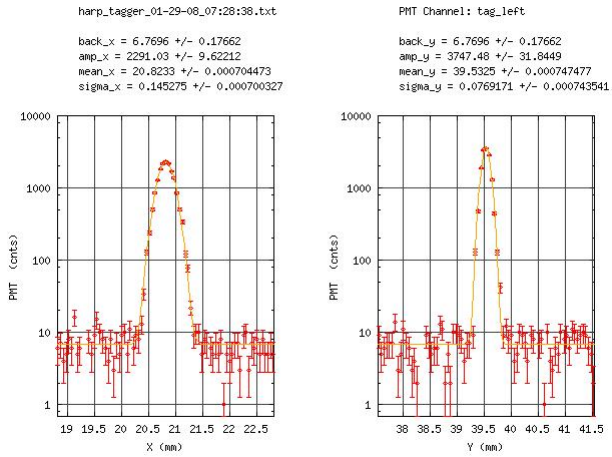


Figure 5.6: Example of a harp scan taken during the experiment. As can be seen from the figure, the beam profile is scanned along two perpendicular axes. The scan also shows that the beam spot is not quite circular, with a width of $\sim$145$\mu$m along the $x$ axis and $\sim$77$\mu$m along the $y$ axis [88].

### 5.6.3 Beam Polarisation

There are five electron beam polarimeters in total in the beamline to measure electron beam polarisation: a Mott Polarimeter in the injector, Møller Polarimeters in the beamlines of Halls A, B and C and a Compton Polarimeter in the Hall A beamline. All three types of polarimeter work on the same principle: electrons in the beam are scattered from a target foil and the asymmetry of scattered electrons is measured to obtain beam polarisation. Only the Mott Polarimeter is non-destructive and in general beam polarisation measurements will interrupt beam delivery for $\sim$30 mins. The Hall B Møller Polarimeter is located immediately upstream of the Bremsstrahlung tagging system, with the detectors for the Møller-scattered electrons located 7 m downstream of the target.

## 5.7 Linearly Polarised Photon Beam Production

Linearly polarised photons were obtained using the coherent Bremsstrahlung technique where unpolarised electrons are incident on a crystalline (diamond) radiator. The recoiling Bremsstrahlung-electrons are momentum analysed in

the tagging spectrometer or tagger. The photons are undeflected by the tagger magnet, passing through a bore hole in the tagger and a collimator on their path to the target. The layout of the various components are shown in Figure 5.7.

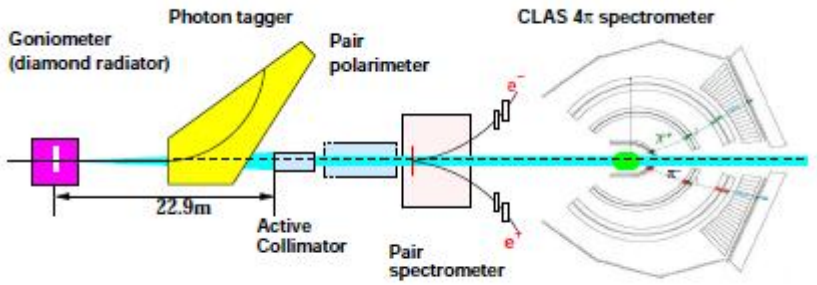


Figure 5.7: Schematic diagram showing the components of the Hall B beamline involved in the production of the photon beam [89].

## 5.8 The Hall B Photon Tagging System

The tagger measures the electron energy and timing, allowing the photon energy to be calculated on an event by event basis from the difference between the energy of the incident and outgoing electrons:

$$E_0 = E_{e^-} + E_\gamma \tag{5.1}$$

where $E_0$ is the incident electron energy, $E_{e^-}$ is the electron energy as measured in the tagger and $E_\gamma$ is the energy of the tagged photon produced by the Bremsstrahlung process on the electron. The energy resolution of the Hall B tagging system is $0.001E_0$ and the timing resolution is 110 ps in a range of energies from 20-95% of $E_0$ up to 6 GeV [82].

The tagger consists of a C-shaped dipole electromagnet which deflects electrons from the beamline onto the tagger hodoscope. The radius of the circular path along which electrons are deflected is dependent on electron energy and the strength of the magnetic field. The magnetic field has to be adjusted for each incident electron beam energy so that a non-radiating electron is directed straight into the tagger beam dump below the floor of Hall B.

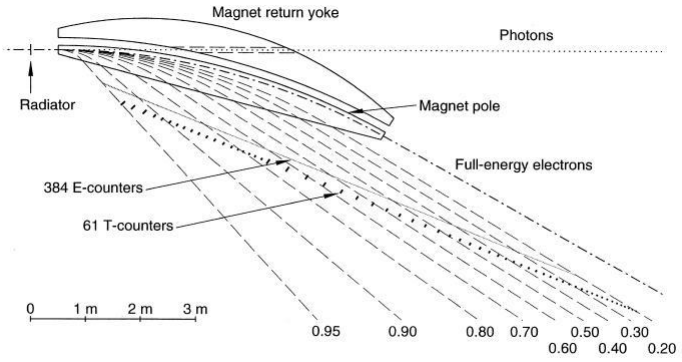


Figure 5.8: Schematic diagram of the tagging system showing the paths of the electrons as a function of relative photon energy, $E_\gamma/E_0$ [83].

On leaving the tagger magnet, the electrons enter the tagger hodoscope. This consists of two planes of plastic scintillators perpendicular to the electron path: an energy plane (E-Plane) and a timing plane (T-Plane) which provide energy and timing information respectively for the radiating electron and hence for the photon.

As shown in Figure 5.9, electrons first pass through the E-Plane which is made up of 384 plastic scintillators, each 20 cm long and 4 mm thick [82]. The widths of the scintillator paddles vary from 6-18 mm so that each one covers a $0.003E_0$ momentum range [83]. The paddles overlap by 1/3 of their width to avoid gaps, resulting in 767 photon energy bins and an energy resolution of $0.001E_0$ [83].

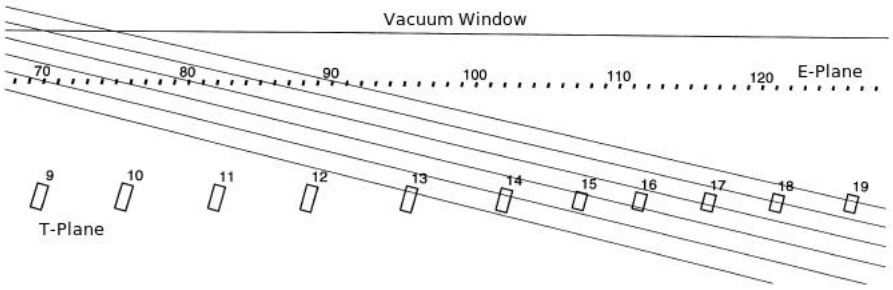


Figure 5.9: Schematic diagram showing the geometry of the E-plane and T-plane scintillators along with possible electron trajectories [83].

The electrons then pass through the T-Plane, situated 20 cm behind the E-Plane. This consists of 61 scintillator paddles which are 2 cm thick and which overlap by a few milimetres. The paddles are divided into two groups of different widths: 42 wider counters for the range 20-75% of $E_0$ and 19 narrower counters for electrons corresponding to a photon energy of 75-95% of $E_0$. The lengths of the paddles also vary from 20 cm long for high momenta electrons to 9 cm long for the low momentum range [83]. This is due to the $1/E_\gamma$ dependence of the Bremsstrahlung cross section and allows the count rate in each detector to be almost the same.

The efficiency of the tagger is measured as the "tagging ratio": the fraction of tagged electrons to photons which are incident on the CLAS target. This can be measured by inserting the Total Absorption Shower Counter (TASC) array [83] into the beam in front of the target. This is a set of four lead-glass blocks in a square 2x2 array which measure photon flux with 100% efficiency. The tagging ratio has been found to be ∼70-80%, dependent on $E_0$ [83].

## 5.9 Collimation and Beam Monitoring

Having passed through the tagger, the photon beam is collimated in order to produce a well-defined beam spot and remove the beam halo. For an unpolarised photon beam, the beam spot is quite large ($\leq$3 cm diameter) compared to the beam spot of the polarised beam ($\leq$5 mm) [82].

The two collimators used in this experiment were situated 14 m downstream from the radiator: a nickel and tungsten cylinder with a 2 mm-diameter cylindrical hole for polarised photon beam experiments, and a cylindrical nickel collimator with a 8.61 mm-diameter hole for use with the unpolarised photon beam [82]. The collimators are divided in two, with a magnet in between each half to remove from the beamline any low-energy particles produced in the collimator.

The photon beam position and the size of the beam spot are constantly monitored during experiments by the pair polarimeter, an array of crossed scintillator-fibres situated 20 m downstream of the target. These detect the $e^+e^-$ pairs produced by the interaction of the photon beam with the target.

## 5.10 The Coherent Bremsstrahlung Technique

The photon beam was produced using the coherent bresstrahlung process, where relativistic electrons pass through a thin crystal and radiate a photon as they are slowed by the electromagnetic field of the atoms in the crystal. Incoherent Bremsstrahlung is produced when the radiating electron transfers recoil momentum to an individual atom in an amorphous radiator, with the atoms of the radiator acting independently of one another. This results in an unpolarised photon beam with a smooth energy dependence falling off as $\sim 1/E_\gamma$. The use of a crystalline radiator allows production of coherent Bremsstrahlung photons. Here the recoil is taken up by a particular crystal lattice vector, with the contributions from individual atoms adding coherently to provide photons over a narrow energy range. The photon spectrum from a crystalline radiator will be a sum of coherent and incoherent Bremsstrahlung contributions. Figure 5.10 compares an incoherent Bremsstrahlung with a coherent Bremsstrahlung spectrum, showing the discrete energy structure arising from the crystal structure.

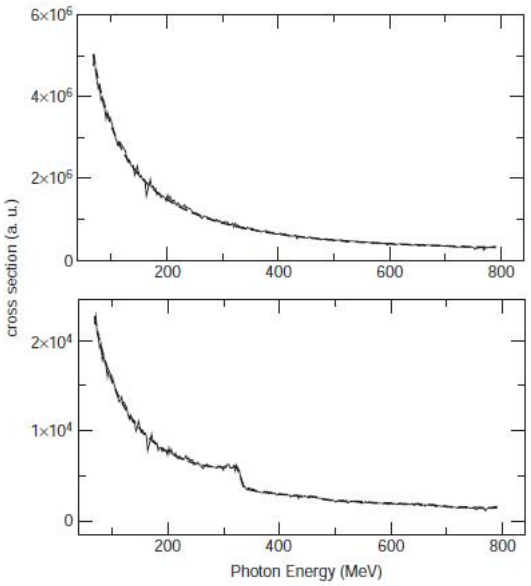


Figure 5.10: Typical Bremsstrahlung spectra for an amorphous radiator (upper plot) and a diamond radiator (lower plot). The solid curve represents experimental data, while the dashed curve represents a theoretical least-squares fit [90].

The features of the coherent spectra can be seen most clearly after dividing through by the photon energy spectrum of an amorphous *ie.* incoherent radiator. The resulting spectrum is then referred to as an "enhancement plot", as shown in Figure 5.11. This plot is characterised by sharp peaks corresponding to the reciprocal lattice vectors of the diamond crystal. This is because the crystal structure restricts the magnitude and direction of the momentum transfer from the electrons to the crystal nuclei, so that the recoil momentum must be equal to a reciprocal lattice vector in the crystal[1]. The reciprocal lattice vector also defines the plane of the electric field vectors of the photons, resulting in polarisation in a single plane.

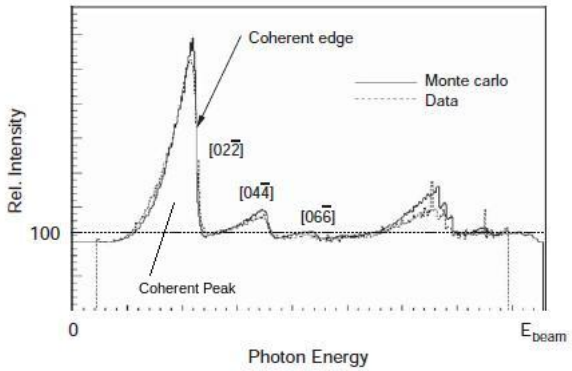


Figure 5.11: Typical enhancement plot for a coherent Bremsstrahlung spectrum, showing both experimental data and a Monte-Carlo simulation [91]. Also shown are the reciprocal lattice vectors of the planes in the diamond crystal responsible for each peak.

By controlling the orientation of the diamond crystal with respect to the electron beam, specific lattice vectors can be selected, thus producing a linearly polarised beam of photons with a chosen direction of polarisation. These photons are emitted in a narrow cone with a characteristic angle $\theta_c = 1/E_\gamma$, whereas incoherent Bremsstrahlung is emitted with a much wider angular distribution. Higher degrees of linear polarisation can be achieved using collimators, as collimation removes the incoherent photons when using a diamond radiator, leaving a higher fraction of coherent photons.

[1]The reciprocal lattice vectors of a plane defined by the Miller Indices (hkl) form a vector orthogonal to that plane, where the length of the reciprocal vector is equal to the spacing between two similar planes.

## 5.11 The Diamond Radiator

The experiment used a 50 $\mu$m-thick natural-diamond radiator mounted onto a goniometer 7 m downstream of the tagger magnet [82]. Having as thin a diamond as possible is desirable to minimise the effect of multiple scattering of electrons as they pass through the radiator as this increases the angular spread of the radiating electrons thereby mixing coherent and incoherent distributions. The goniometer allowed for precise orientation of the diamond through three rotational and two translational axes. An amorphous carbon radiator was also mounted onto the target ladder and used to produce an unpolarised photon beam.

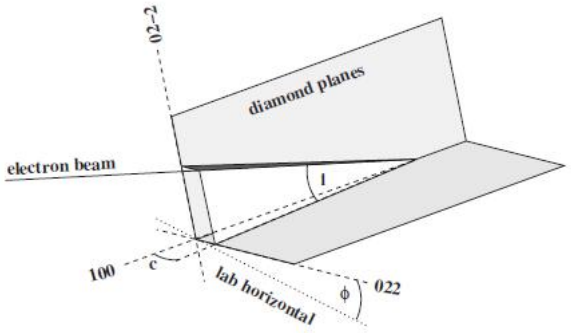


Figure 5.12: Diagram showing the 100 diamond plane and the sets of planes defined by the [022] and [02$\bar{2}$] reciprocal lattice vectors. The angle of the electron beam with respect to the diamond plane and scattering angles are also shown [91].

Diamond was chosen as a radiator for coherent Bremsstrahlung production for two main reasons: its high Debye temperature means the thermal motion of the carbon atoms within the crystal are small, so the lattice structure is relatively unaffected; and relatively defect-free diamond crystals are easily obtained compared to other crystals suitable for coherent Bremsstrahlung (such as beryllium) [92].

## 5.12 Calculation of the Photon Beam Polarisation

To extract the $G$ observable, as well as the other polarisation observables measured in this experiment, it was necessary to know the degree of linear beam polarisation as accurately as possible. The orientation of the polarisation plane must also be established with accuracy and can be determined from the goniometer settings.

The calculation of the degree of linear beam polarisation involves comparing the shape of the coherent Bremsstrahlung spectrum to a spectrum obtained from theoretical Bremsstrahlung calculations. As described in Section 5.10, an enhancement plot can be used to separate the coherent contribution from the incoherent contribution to the spectra. The enhancement plots are fit with a theoretical spectrum produced by the Analytical Bremsstrahlung (ANB) Calculation [93, 94]. The ANB calculation takes into account 17 experimental parameters characterising the geometry of the radiator, collimator and photon beam. Several of these parameters can be measured experimentally (such as photon beam energy and beam spot size) whereas others (such as electron beam divergence on the radiator) are varied until a good agreement is obtained between the enhancement plot and the ANB calculation. These parameters are then extracted from the fit and are used to calculate the degree of polarisation per event as a function of photon energy. This information is then summarised in lookup tables.

## 5.13 The CLAS Detector

The photon beam collides with the target at the centre of the CEBAF Large Acceptance Spectrometer (CLAS), the main detector system in Hall B. As can be seen in Figure 5.14, CLAS is a multi-layered magnetic spectrometer, divided into six independent sectors by six superconducting coils arranged symmetrically around the beamline producing a toroidal magnetic field. There is a magnetic field-free region in the centre of the detector, allowing for the use of polarised targets such as FROST (Chapter 6). For photon beam experiments, a scintillator start counter providing timing and triggering information on reaction products

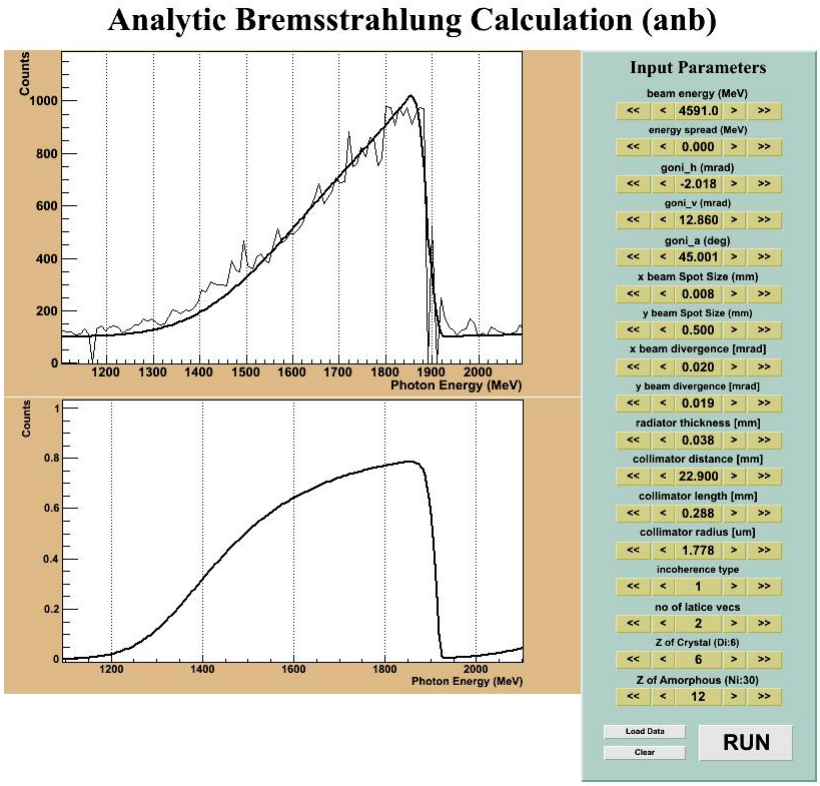


Figure 5.13: Screen-shot taken during an ANB calculation. The upper plot shows the enhancement spectrum and the lower plot shows calculated polarisation as a function of photon beam energy.

is the innermost detector surrounding the target. Outside the start counter, the first three layers of detectors consist of drift chambers to determine the curved trajectories and hence momenta of charged particles. Surrounding the drift chambers, a gas Cherenkov Counter identifies electron events and allows for the differentiation of electrons from pions. This is then surrounded by a layer of plastic scintillator for time-of-flight measurements. The outermost detector system is made up of electromagnetic calorimeters for the detection of photons, electrons and high-energy neutrons. This design of CLAS allows charged particles to be detected with high-momentum resolution over ∼75% of the $4\pi$ azimuthal angle.

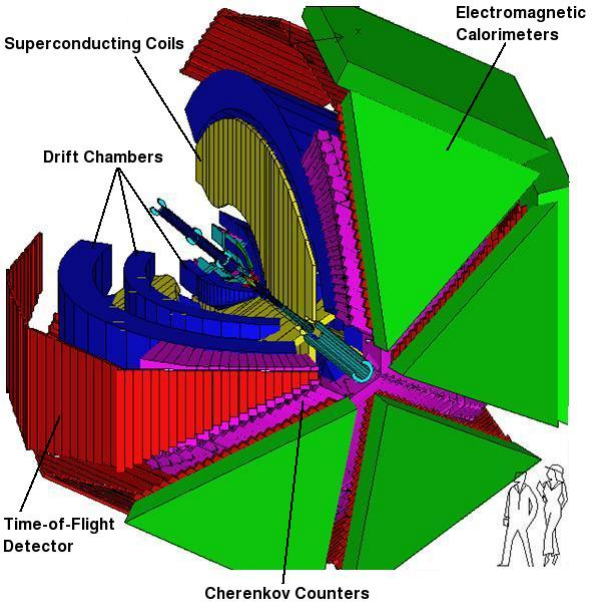


Figure 5.14: Schematic diagram of the CLAS detector, adapted from [95].

## 5.14 The Torus Magnets

The six superconducting coils which comprise the torus magnets are each made of four layers of 54 turns of aluminium-stabilised NaTi/Cu, cooled by supercritical He to 4.5 K [82]. This wire is wound into a kidney-shape, designed so that the main field component is in the azimuthal direction, with the highest magnetic field gradient (∼2.5 Tm) in the forward direction and the lowest magnetic field

gradient (∼0.6 Tm) at larger scattering angles [82]. This magnetic field geometry (Figure 5.16) allows the degree of curvature of the charged-particle tracks to be optimised as the majority of charged particles will be emitted in the forward direction. The inner shape of the coils is circular, in order to minimise their effect on charged particle trajectories passing close to the coil surfaces. In spite of this careful design, the presence of the six torus magnets is responsible for reducing the acceptance of CLAS to ∼75% of $4\pi$.

For the experiment described in this thesis, data were taken with a positive polarity field and a setting of 1920 A, where positive polarity means that positively charged particles are bent outwards from the beamline and negatively charged particles towards the beamline [96].

Figure 5.15: Photograph of the torus magnets before installation [97]. They are each 5 m long and 5 m in diameter.

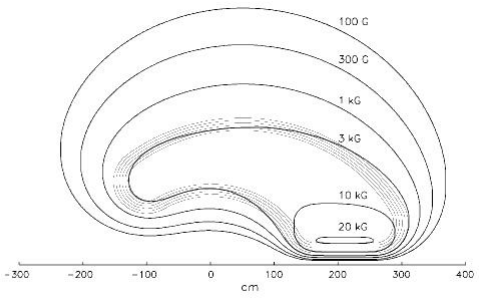


Figure 5.16: Field map for the CLAS toroidal magnetic field in the midplane of one of the CLAS sectors [82].

## 5.15 The Start Counter

The start counter (SC) provides the start signal for the experimental trigger. The timing information from the SC is also used in conjunction with timing information from the tagger T-Counters (Section 7.2) to identify which RF beam bucket is responsible for each reaction.

The start counter consists of 24 EJ-200 scintillator paddles [98] coupled to an acrylic light-guide, arranged in six sectors where one paddle plus its mirror image form one sector. Each paddle is 619.5 mm long in total, with a 502 mm-long straight section and a tapered triangular end section referred to as the "nose" [98]. The paddles are 29 mm wide and 2.15 mm thick and are wrapped in VM-2000 radiant mirror film with every other paddle wrapped in black tedlar film to minimise light loss [98]. The light produced by the scintillators is detected by 15 mm-diameter photomultiplier tubes (PMTs) [98], which are located upstream away from the acceptance of CLAS.

The SC timing resolution was measured by comparing the difference in the time of an event as measured by the start counter and the time of the event at the vertex to the RF time of the accelerator. It was found that timing resolution in the straight section is 292±1 ps in the nose 324±2 ps [98], which is far smaller than the ±1 ns required to differentiate between the electron beam bunches.

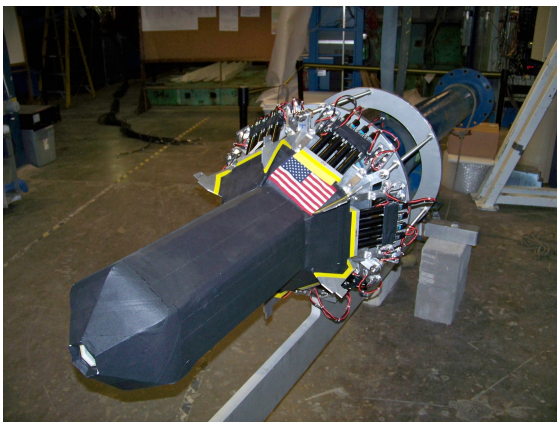

Figure 5.17: Photograph of the start counter showing the wrapped scinillator paddles and light guides as well as the photomultiplier tubes [97].

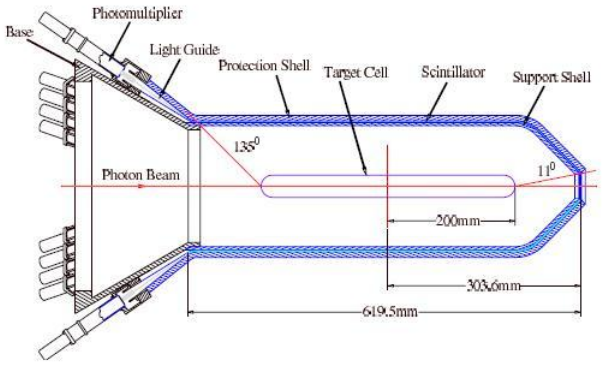


Figure 5.18: Schematic diagram showing a cross section of the start counter [98].

## 5.16 The Drift Chambers

The drift chambers (DCs) are used to measure the momentum and velocity of charged particles in CLAS. There are three layers or "regions" of drift chambers, divided into six sectors and therefore there are 18 drift chamber modules in total. The Region 1 drift chambers are the closest to the target ($\sim$1 m from the beamline), and provide the initial trajectory of charged particles leaving the target. The Region 2 drift chambers are situated in an area of high magnetic field between the torus coils and $\sim$2 m from the beamline and therefore provide the best momentum resolution. The outermost drift chambers are those of Region 3, located outside the torus coils, providing information about charged particle trajectories as they enter the Cherenkov Counters.

Each drift chamber module is trapezoidal in shape, designed to fit between the torus coils. In order to obtain a maximum possible acceptance, all non-active parts of the detector (such as the electronics) are placed in the "shadow" of the torus coils. The DCs therefore cover a polar angular range of $8^0 \leq \theta \leq 142^0$ and over 80% of the azimuthal angle [95]. Inside the drift chamber modules, the wires are stretched between the drift chamber endplates, with the endplates parallel to the neighbouring coil plane and tilted at $60^0$ to the neighbouring DC endplates. As a result, the wires are almost perpendicular to the bend plane of the charged particles, which increases the sensitivity of the DCs to particle momenta. The drift chambers are filled with a mixture of $\sim$88% Ar and $\sim$12% $CO_2$, chosen for its high drift velocity and because it can operate at several hundred volts before

Figure 5.19: Photograph of the Region 3 drift chambers, with part of the time-of-flight detector in the background on the left [97].

breakdown [95].

The DC wires themselves are arranged in layers with one layer of sense wires followed by two layers of field wires. This results in a hexagonal structure with a sense wire at the centre of the hexagon and field wires at the vertices, as shown in Figure 5.20. The hexagonal cell structure was chosen as it is a good approximation to a circular cell in which drift time and drift distance are independent of the angle of charged particle trajectories. The wire cells are then arranged in two "superlayers" consisting of six layers of cells: the first superlayer is aligned along the magnetic field and the second is aligned at a $6^0$ stereo angle to the first to provide azimuthal information for the particle trajectory[2]. The perimeter of each superlayer is surrounded by a layer of guard wires, with a potential such that the electric field configuration is equivalent to that of an inifinite grid of cells. This layer of guard wires is necessary to ensure that the electric field at the surface of all sense wires is the same.

The sense wires are made of 20 $\mu$m-diameter gold-plated tungsten [95], chosen for its durability and the gold plating ensures that the wires are chemically inert. The field wires are made of 140 $\mu$m-diameter gold-plated aluminium 5056 alloy [95], chosen for its long radiation length which minimises multiple scattering and for its low density allowing the wires to be strung at lower tension.

The sense wires are held at a positive potential and the field wires at a negative potential by high voltage translation boards mounted to the high-voltage side of

[2]The Region 1 drift chambers are an exception to this, having only six axial layers and four stereo layers due to space constraints.

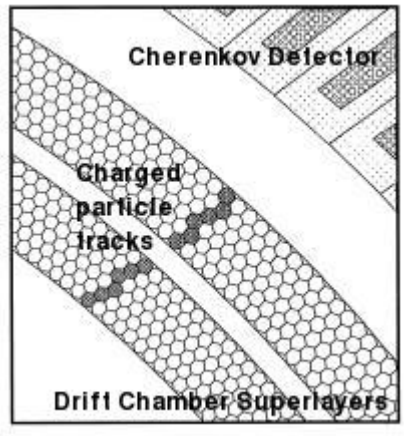


Figure 5.20: Schematic diagram showing the layout of the two superlayers and the hexagonal cells formed by the sense wires and the field wires in the Region 3 DC. Also shown as the dark-grey filled cells is the track of a charged particle. Note that the guard wires are not shown in this diagram [82].

each DC module. On the other side of the module, multi-layer printed circuit boards (PCBs) receive electrical signals from each sense wire and decouple the high voltage from the signal. This signal is then sent to the CLAS readout electronics by 20 m-long twisted pair cables.

The track resolution obtained by the drift chambers varies from 300-450 $\mu$m for all regions, equivalent to an uncertainty of $\leq$0.5% for particles with an energy of 1 GeV/c [95]. The angular resolution of these constructed tracks is $\leq$2 mrad [95].

The efficiency of the drift chambers can be characterised in two ways: the "layer efficiency", the probability that a hit is recorded in a wire layer through which a track has passed; and the "tracking efficiency", the probability of identifying a track when charged particles are kinematically predicted to pass through an active region of the drift chambers. The average layer efficiency has been found to be $\geq$98% [82]. The tracking layer efficiencies are $\geq$95% for chamber hit occupancies up to 4% [95].

## 5.17 The Cherenkov Counters

The Cherenkov Counters (CC) are used to detect electrons and to differentiate between electron and pion events. For this reason, they are most important for electroproduction experiments where, in conjunction with the electromagnetic calorimeters, they form part of the Level 1 trigger determining if an event contains a scattered electron.

Figure 5.21: Photograph of one of the six Cherenkov Counter sectors during installation in the CLAS detector. The drift chambers are shown in the background on the left of the photograph [97].

The CCs are situated between the time-of-flight scintillator and the Region 3 Drift Chambers. They are divided into the six azimuthal sectors of CLAS, each subtending an azimuthal angle of $60^0$, and covering a scattering angle in each sector of $8^0 \leq \theta \leq 45^0$ [82]. This polar angular range of each sector is then divided into 18 regions, each of which is further subdivided into two modules about the symmetry plane dividing each region. There are therefore 12 subsectors around each azimuthal region and therefore 216 light collection modules in total.

A schematic diagram of a pair of CC modules is shown in Figure 5.22. Each module consists of a hyperbolic and an elliptical mirror which focus the Cherenkov light onto a Winston Cone. They are designed so that the light is primarily focused in the azimuthal direction preserving information about the scattering angle of the charged particles whose trajectories are primarily in the $\phi$ plane. Any abberations due to imperfections in these mirrors are corrected by the circular mirror.

The CC modules are filled with perfluorobutane gas ($C_4F_{10}$), chosen for

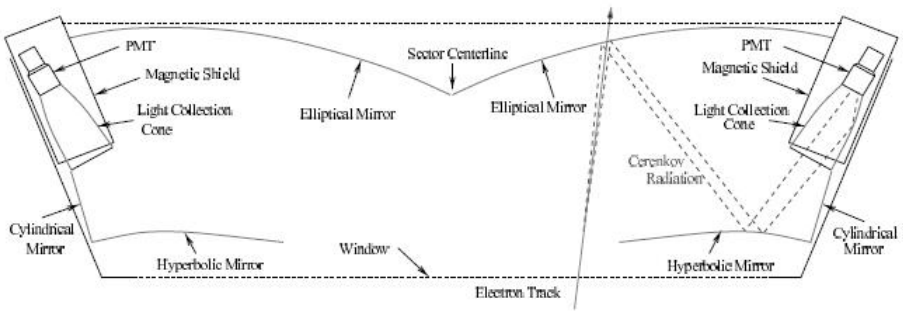


Figure 5.22: Schematic diagram of a pair of Cherenkov Counter Modules with an electron track shown [82].

its high refractive index ($n$=1.00153), its high pion-momentum threshold (2.5 GeV/c) and its excellent light transmission properties [99]. Highly sensitive PMTs able to trigger on a single electron detect the Cherenkov light are located in the shadow of the torus coils in order to maximise the active region of the Cherenkov detectors. The PMT signals are sent to amplifiers and split; one part is used to determine the threshold settings and reduce noise, the other is read out along with TDC information and data from the other detectors.

The performance of the Cherenkov Counters is mainly limited by the reflectivity of the mirrors which is ∼85% in the UV region typical of Cherenkov light [99]. Using elastic scattering of electrons from a hydrogen target, the electron detection efficiency within the fiducial regions of the detector has been found to be ≥99% [99]. Here the fiducial regions are defined by the edges of the mirrors, and this efficiency excludes the midplane of the mirrors where the gaps in the mirrors are largest.

## 5.18 Time of Flight

The CLAS time-of-flight (TOF) system forms part of the Level 1 Trigger and is also used for particle identification through time-of-flight calculations.

The TOF covers the full azimuthal angular range of CLAS and a scattering angle of $8^0 \leq \theta \leq 142^0$ [82]. It consists of a layer of highly-segmented, 5.08 cm-thick scintillators [82] positioned between the Cherenkov counters and the electromagnetic calorimeters. The TOF paddles are made of long, rectangular

pieces of Bicron BC-408 plastic scintillator and vary in length from 32 cm at small scattering angles to 450 cm at larger angles [100]. This material was chosen as it has a fast response time and low light attenuation, allowing for excellent timing resolution. The paddles located at "forward" angles of $\theta \leq 45^0$ are 15 cm wide whereas at all other angles they are 22 cm wide [82]. The scintillator is wrapped in two layers of aluminium foil and a layer of black capton with a 0.0127 cm-thick lead foil on the side facing the target to shield the detectors from X-Rays [100]. Each of the six sectors of CLAS has 57 TOF scintillators positioned perpendicular to the beam direction and tilted perpendicular to the average particle tranjectory, with each scintillator subtending a $1.5^0$ scattering angle [82]. The light from each scintillator is measured by a PMT coupled to each end which is again positioned in the "shadow" of the coils along with the other inactive components of the TOF system. The signals from the PMTs are then read out by ADCs and sent to TDCs which record the size and timing of the pulses.

The timing resolution of the TOF was investigated using cosmic rays, a laser calibration system and reconstructed $e\pi$ coincidence events, from the first CLAS electron beam experiment. It was found to vary between ∼80 ps for the shortest paddles and ∼160 ps for the longest paddles, much smaller than the maximum acceptable resolution of 120 ps and 250 ps for the longest and shortest paddles respectively [100].

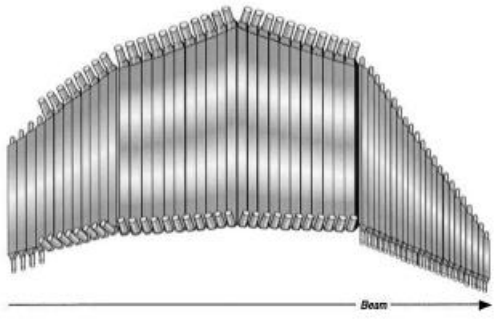


Figure 5.23: Schematic diagram of one sector of the time-of-flight detector system showing the segmented structure of the system, with the scintillator paddles arranged perpendicular to the beam direction. Also shown are the PMTs coupled to each end of the scintillator paddles [100].

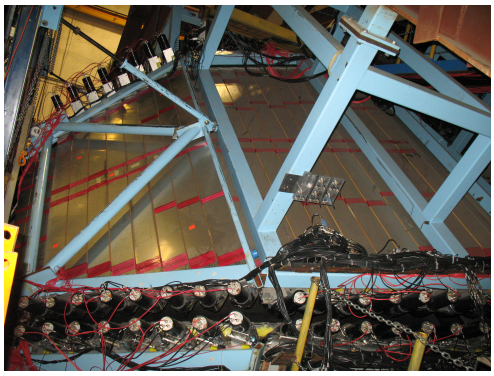

Figure 5.24: Photograph of a sector of the TOF detectors during the construction of CLAS [97].

## 5.19 The Forward Electromagnetic Calorimeter

The electromagnetic calorimeters (EC) form the outermost layer of the CLAS detector. Their purpose is to detect electrons at energies $\geq$0.5 GeV, neutrons, and photons at energies $\geq$0.2 GeV. In addition the EC also forms part of the trigger system for experiments using electron beams.

Figure 5.25: Photograph showing the electromagnetic calorimeters on the right of the image with the rest of the CLAS detector subsystems on the left [97].

The forward EC subtends an angle of $8^0 \leq \theta \leq 45^0$ [82]. Its sectors are made up of 39 alternating layers of Bicron BC412 plastic scintillator sheets and 2.2 mm-thick lead sheets [101]. The sheets are in the shape of an equilateral triangle, whose area increases as a function of distance from the target, allowing the EC to fill all available space in CLAS, as well as minimising shower leakage and dispersion in arrival times of signals from the different layers.

The scintillator layers are divided into 36 strips parallel to one side of the equilateral triangle, with the strips in each successive layer being rotated by $120^0$. This arrangement allows access to stereo information of the energy deposition of the showering particles. For longitudinal information, the 13 layers in each orientation are further divided into an inner group of five layers and an outer group of eight layers, referred to as "stacks". The layers of each stack are then connected by acrylic light-guides to a PMT, with one PMT for each stack. The PMTs are then mounted to the downstream (non-active) side of the EC.

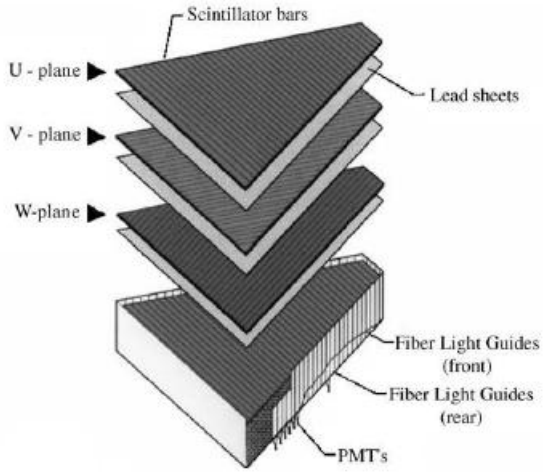


Figure 5.26: Schematic diagram of a sector of the forward electromagnetic calorimeter showing its layered structure. The three possible orientations of the scintillator strips are referred to as "views" and are labelled here as U, V and W [101].

The energy and timing of each hit in the EC is calculated from the distance of the hit position to the readout-edge of the scintillator strip. For the hit to be valid, the showering particle must have deposited energy in both stacks and all three layers of scintillator. The average position resolution was found to be $\sim$2.3 cm, measured by the difference in the charged particle hit position in the EC and the projected charged particle position from the trajectory recorded by the drift chambers [101]. The timing resolution was measured by comparing the timing information of the EC to that of the TOF scintillators for charged-particle events. For electrons this was found to be $\sim$200 ps [101].

## 5.20 The Large Angle Calorimeter

Similar in structure to the Forward EC, the Large Angle Calorimeter (LAC) is also used to detect electrons and neutral particles, particularly for experiments requiring such measurements at backward angles. In particular, the LAC has been designed to detect neutrons with high efficiency. In contrast to the other detector subsystems, the LAC covers only two sectors in CLAS, subtending an azimuthal angle of $120^0$ and a polar angle of $45^0 \leq \theta \leq 75^0$ [82].

The two LAC modules are rectangular and consist of 33 layers of 0.2 cm-thick lead sheets and 1.5 cm-thick layers of NE110A plastic scintillator [82]. The scintillator is divided into strips which vary from 10 cm wide for the inner layers to 11.15 cm wide for the outer layers, with the orientation of the strips being rotated by $90^0$ for each successive layer [102]. As for the forward EC, the two orientations are also further divided into two stacks: an inner stack of 17 layers and an outer stack of 16 layers. The scintillator layers of each stack are connected by light guides attached to both ends of the strips and the light signals are detected by two PMTs [102], with one PMT for each stack.

The neutron detection efficiency above neutron energies of 0.5 GeV/c is ∼30%. The time resolution was measured with cosmic rays and was found to be ∼260 ps over the whole detector [82].

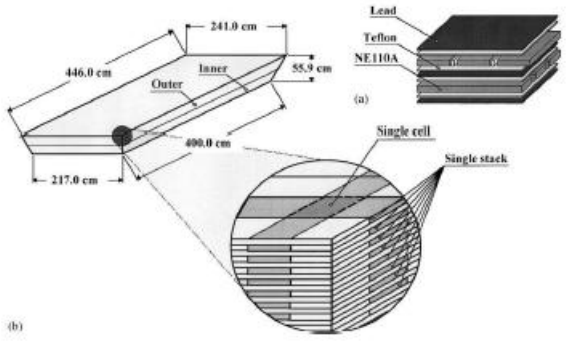


Figure 5.27: Schematic diagram of one of the two large angle calorimeter modules, showing their layered structure [103].

## 5.21 The Trigger System

All signals from the detector subsystems are passed to a two-level trigger system controlled by the trigger supervisor which determines if an event belongs to a real physical process of interest to the experiment.

The Level 1 Trigger is initiated by coincident hits in the tagging spectrometer, start counter and time-of-flight scintillators. It then compares the hit patterns in each of the detectors to patterns loaded in memory tables. These tables must be programmed for each experiment using the graphical software package TIGRIS [82]. The patterns are then correlated and geometrical constraints applied in order to identify likely events. In total, the Level 1 Trigger requires 90.5 ns of processing time [82].

The Level 2 Trigger may then be used to veto events which pass the Level 1 Trigger conditions, but which leave no tracks in the drift chambers such as a cosmic ray passing through CLAS. The Level 2 Trigger looks for probable tracks corresponding to each event recorded by the drift chambers. If the event cleared by the Level 1 trigger does not match any of the tracks, the Level 2 trigger issues a "Level 2 Fail" signal and the event is not recorded. This process will take $\sim$2 $\mu$s and contributes directly the the deadtime of CLAS [104].

Once an event has passed both the Level 1 and Level 2 triggers, the trigger supervisor outputs the event information to the readout electronics. The trigger supervisor can also be configured to require only a Level 1 Trigger or both Level 1 and Level 2, depending on experimental requirements. The trigger for this experiment was the detection of one charged particle in CLAS and both Level 1 and Level 2 triggers were used. The trigger supervisor also produces all the signals and resets required by the detector electronics. A time of $\sim$1 $\mu$s is required for all electronics to be reset and become active again if both Level 1 and Level 2 triggers are used [104].

## 5.22 Data Acquisition

24 FASTBUS and VME crates in Hall B digitise the data from each of the detector subsystems and then pass this data to the 24 VME Readout Controllers (ROCs) within these crates [82]. Here the data are formed into tables, or event fragments, before being output to the CLAS Online Acquisition Computer (CLON10) in the

Hall B control room. CLON10 is made up of three systems which process the data fragments so that they can be transferred to tape for storage. The first stage is the Event Builder (EB) which assembles the fragments into complete events and gives the tables headers and labels. The Event Transport (ET) then sends some of the data for online reconstruction, analysis and monitoring in the control room. The ET sends the rest of the data to the Event Recorder (ER) which writes the data in a single stream to the local RAID[3] disks. From here the data can be transferred to the JLab Tape Silo for permananent storage.

The acquisition, monitoring and storage of data is managed by the CEBAF online data acquisition system (CODA) [105]. Before data taking can begin, this system first configures all of the DAQ components and electronics. All executable code required by the ROCs and the EB, detector parameters and trigger logic are then downloaded from the run configuration file for the experiment. These parameters are then read back from the hardware and compared to the original run configuration in the "prestart" phase. The run can then begin with the trigger enabled. Data is then recorded along with scalar readings in ∼2 GB files (the maximum file size permitted by the Linux machines), with each run lasting between one and two hours and containing ∼40 files.

[3]Redundant Array of Independent Disks

# Chapter 6

# The Frozen Spin Target, FROST

The frozen spin target, FROST, was purpose built for the *g9* series of experiments [56, 58, 59, 60] by the Jefferson Lab Polarised Target Group and contributing Universities in the US and the UK. The experiment with which this thesis is concerned was the first experiment in which a frozen spin target had been used at Jefferson Lab. A description of FROST and the reasons why such a target was required will be covered in the first half of this chapter. The second half will describe the calculation of the target polarisation which was carried out by the author, work which formed the basis of all analyses using the FROST target. This was the first use of the FROST target, so the method for extracting the polarisation with minimal systematic errors had to be developed as part of this thesis.

## 6.1 Background

The first polarised nucleon targets were built in the early 1960s, following the development of the Dynamic Nuclear Polarisation Process (see Section 1.2) for metals (Overhauser Effect) in 1953 and for solid insulators (Solid State Effect) in 1958 [106]. These targets were "continuously polarised", meaning they had to be kept in a high magnetic field and continually illuminated with microwave radiation. The main disadvantage of such targets for use in reaction measurements is that they require a large magnet to surround them, limiting the angle and energy ranges at which reaction products can be detected.

The first successful Frozen Spin Targets were developed in the 1970s and made

truly operational following advances in the field of $^3$He/$^4$He dilution refrigeration [107]. Prior to this, target cryogenic systems used $^3$He and $^4$He evaporative cooling which only achieve temperatures as low as $\sim$0.5 K, therefore restricting targets to continuous polarisation [106]. The principle of operating a frozen spin target is to polarise the target material in a high magnetic field and at a low temperature before cooling the target even further to "freeze in" the polarisation.

A polarised target used previously in Hall B at Jefferson Lab was continuously polarised at a temperature $\sim$1 K and in a field of 5 T [108]. As a result only particles scattered in a forward cone of $\pm 55^0$ could be detected [109], corresponding to only $\sim$25% of the $4\pi$ acceptance of CLAS [110]. The *g9* experiments required a target that could be polarised both longitudinally and transversely, with a minimal effect on the trajectories of outgoing reaction products *ie.* a minimal amount of material and only a small magnetic field surrounding the target. These requirements were met with the development of the frozen spin target, FROST, shown in Figure 6.1. The FROST apparatus comprises a continuously working cryogenic system, a high field "polarising" magnet, a low field "holding" magnet, a microwave source and an NMR system to measure the degree of polarisation. This is placed on a rail mounted cart which can position the target with precision of less than a millimetre [111].

The main geometrical constraints on the design of the FROST were dictated by the CLAS detector. FROST is designed to fit into the field-free region which is 200 cm long and 25 cm in diameter [59]. FROST therefore has a horizontal design allowing all cryogenic components to be placed at angles backward of $135^0$, giving clean acceptance in the $0^0$ to $150^0$ region.

## 6.2 The target material

The FROST target material consists of frozen, 1-2 mm beads of butanol ($C_4H_9OH$) mixed by weight with 5% $H_2O$ and 0.5% TEMPO (2,2,6,6-tetramethylp ipendine-1-oxyl) [113], and placed inside the target cup which is 50 mm long and 15 mm in diameter [56]. The target material was chosen to have a high maximum polarisation, a high ratio of polarisable nucleons to the total number of nucleons (the quality factor), a high resistance to ionising radiation, and a small number of unwanted polarisable nuclei [56]. The target material must also be easy to

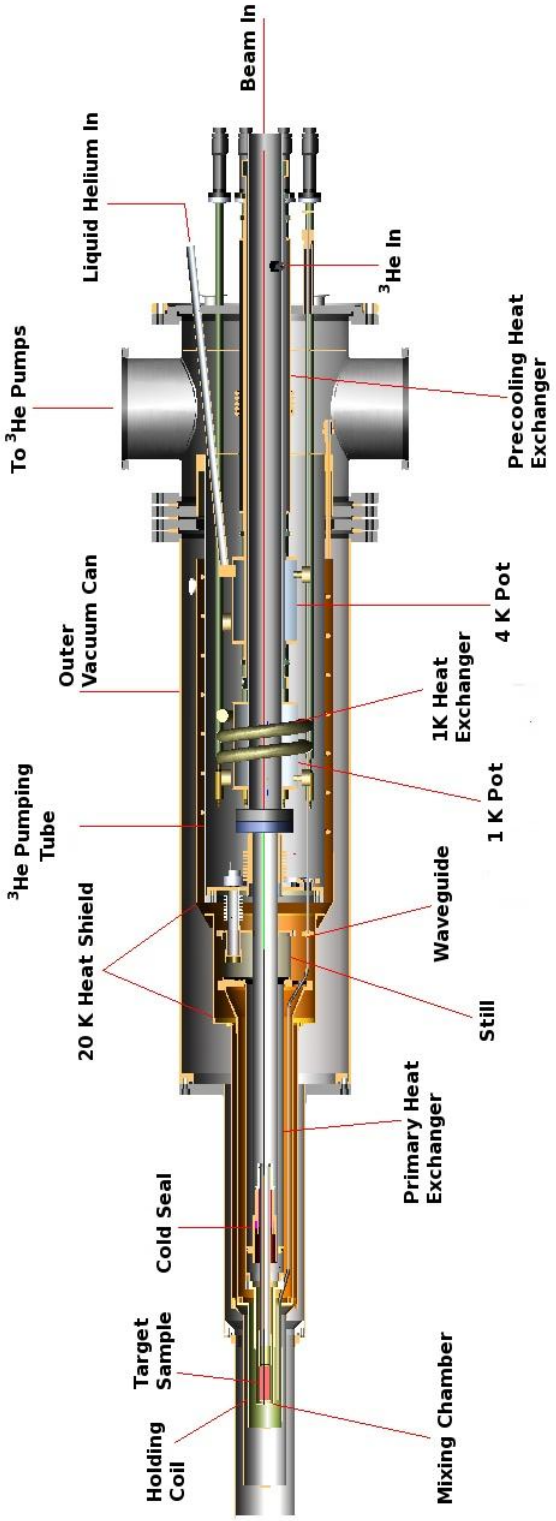


Figure 6.1: Schematic diagram of FROST inside the polarising magnet during "polarisation mode" [112].

prepare and handle and have a short polarisation build up time along with a long relaxation time.

Butanol is a good choice of material as it has a large number of polarisable nuclei (H atoms), high achievable polarisation levels of 85% to 90% [56] and a long relaxation time of ∼600 hours [109]. Additionally, as the carbon and oxygen are spinless particles, pure butanol has no background polarisation. The quality factor of butanol is also relatively high compared to most other target materials as can be seen in Table 6.1.

Table 6.1: The properties of the most commonly used target materials [110].

| Name | Dopant | Quality Factor | Radiation Resistance |
|---|---|---|---|
| Polyethylene, $C_2H_4$ | chemical | 0.12 | low |
| Polystyrene, $C_8H_8$ | chemical | 0.07 | low |
| Propandiol, $C_3H_6(OH)_2$ | chemical | 0.11 | moderate |
| Butanol, $C_4H_9OH$ | chemical | 0.13 | moderate |
| Ammonia, $^{15}NH_3$ | radiation | 0.17 | high |
| Lithium Hydride, $^7LiH$ | radiation | 0.12 | very high |

As the target is polarised using Dynamic Nuclear Polarisation, it is necessary to imbed free electrons (paramagnetic radicals) into the target material (Section 6.4) either by irradiating the target material or through the use of a chemical dopant.

Many studies were performed from the 1960s to the 1980s to determine the combinations of target material and dopant which result in a high polarisation [114, 115]. For butanol, TEMPO and porphyrexide are the most commonly used chemical dopants [116]. TEMPO was chosen as the dopant in this experiment as it is easily obtainable, inexpensive, and stable at the temperatures at which the FROST target operates [112, 117]. After doping the resulting electron concentration is $\sim 10^{19}$ spins/cm$^3$ [113].

$H_2O$ is mixed into the target material to prevent butanol crystals forming during the "shock freezing" process used to produce the butanol beads. In this process the liquid butanol mixture is dropped into liquid nitrogen. This procedure allows the creation of an amorphous or "glassy" state favourable for a uniform distribution of the TEMPO and hence the paramagnetic radicals throughout the material [112, 118].

## 6.3 The Target Cooling System

The main requirements of the FROST target cooling system are that: it must provide a cooling power of several mW at 0.2-0.3 K while absorbing ∼20 mW microwave power during polarisation mode; and during "frozen spin mode" a cooling power a few $\mu$W at 50 mK is necessary to overcome heating from the incident beam and additional sources of heat such as thermal radiation and vibrations [112].

The previous Hall B Polarised target, which used a $^4$He evaporation refrigerator would not be able to achieve a temperature low enough for frozen spin operation. In this earlier design, the target material was immersed in liquid $^4$He, which cooled as He atoms moved from the liquid to the vapour phase, removing energy from the system to overcome the interatomic forces. However, for such a system, cooling power is dependent on the $^4$He vapour pressure which decreases exponentially with temperature. Therefore cooling power also decreases exponentially with respect to temperature and the lowest temperatures which can be achieved are ∼1 K [119].

The solution is to use a $^3$He/$^4$He dilution refrigerator which can achieve much lower temperatures. The design of such a refrigerator was first proposed by Heinz London in 1961 [120] and the first dilution refrigerator was built by Das, de Bruyn Ouboter and Taconis in 1965, achieving a temperature of 0.22 K [121]. One year later, with an improved design, B.S. Neganov *et al.* in Dubna and H.E. Hall *et al.* in Manchester achieved temperatures of ∼25 mK [119].

Dilution refrigeration works on the principle that below 0.87 K [120] a mixture of $^3$He and $^4$He will spontaneously separate into a $^3$He rich (concentrated) phase and a $^3$He poor (dilute) phase. The relative proportions of $^3$He and $^4$He in each phase are temperature dependent; as the temperature approaches 0 K, the concentration of $^3$He in the concentrated phase approaches 100%, whereas in the dilute phase a minimum of 6.4% $^3$He will always be present [106]. Additionally, $^4$He condenses to its superfluid state at temperatures $\leq$2.177 K [119], so in the dilution refrigerator system it may be thought of as being thermally inert. We can therefore neglect its contribution and model the mixture as $^3$He liquid (the concentrated phase) lying above $^3$He vapour (the dilute phase), analagous to an "upside-down" $^3$He evaporation refrigerator (Figure 6.2).

If $^3$He is now removed from the dilute phase, $^3$He atoms from the concentrated

phase will cross the phase separation line in order to re-establish equilibrium, absorbing energy in the process and thus cooling the liquid. In this case, the cooling power is now dependent on the rate of dilution combined with the difference in enthalpy of $^3$He in the concentrated and dilute phases which is proportional to temperature squared [119].

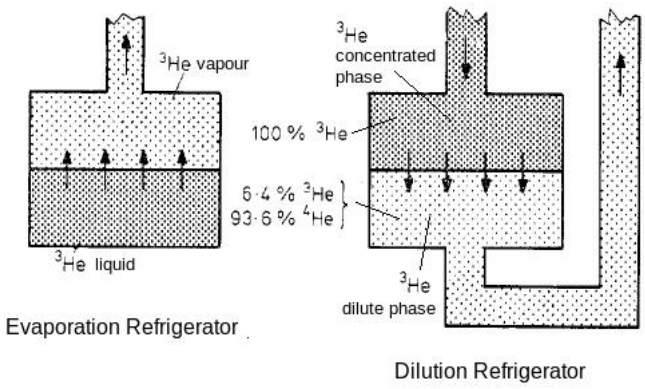


Figure 6.2: Schematic diagram comparing an evaporation refrigerator to a dilution refrigerator. The mixing of liquid $^3$He and $^4$He below 0.87 K and their relative concentrations are also shown, along with arrows representing the direction of flow of $^3$He atoms during the cooling process [121].

FROST has a horizontal design, but the principle of operation is the same as for the conventional dilution refrigerator shown in Figure 6.3. The vertical refrigerator design is included here as the individual components described below are more clearly shown than in Figure 6.1.

The cooling system is divided into three main components through which $^3$He is continuously recirculated. $^3$He at $\sim$300 K enters the precooler where it flows through a preliminary heat exchanger where it is cooled to 5 K, followed by a coiled heat exchanger where it is cooled further to 2.5 K. The $^3$He then enters the condenser where the $^3$He is condensed at $\sim$1 K. The precooler contains two vessels filled with $^4$He at $\sim$4 K and $\sim$1 K which are cooled by evaporation and which provide the $^4$He vapour which flows through the precooler heat exchangers. Once liquified, the $^3$He is further cooled inside a copper capillary tube submerged in the still, followed by a counterflow heat exchanger between the still and the mixing chamber. For FROST, the last (and coldest) sections of this heat exchanger

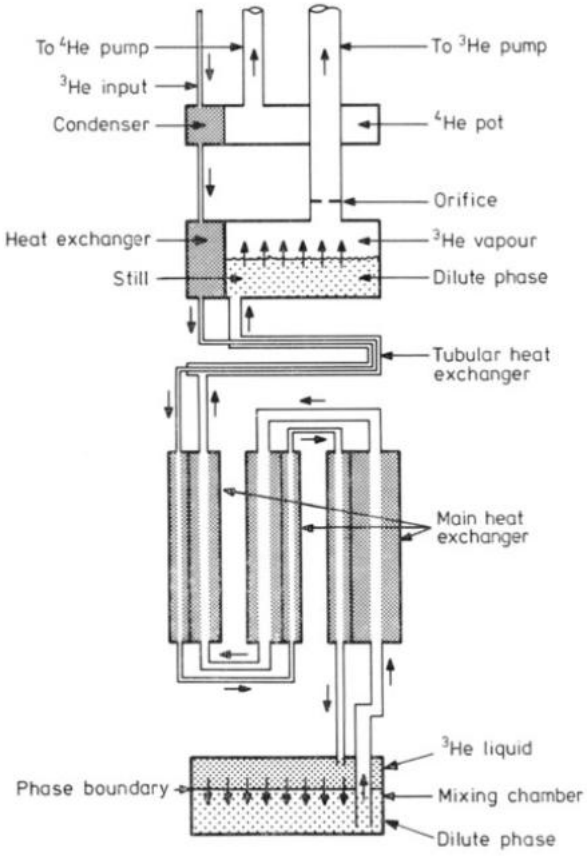


Figure 6.3: Schematic diagram of a conventional dilution refrigerator [121].

consists of several sections of copper tube with copper powder sintered on both the inner and outer surfaces to provide a total surface area for heat exchange of ∼4 $m^2$. This large area is required to compensate for the thermal boundary (Kapitza) resistance between liquid helium and the body of the heat exchanger [119].

The mixing chamber is cooled by removal of $^3$He from the dilute phase causing the incoming $^3$He to cross the phase boundary into the dilute phase. This is done by pumping $^3$He vapour from the still, drawing $^3$He liquid in the still into the vapour phase and thus drawing $^3$He atoms from the dilute phase in the mixing chamber upwards by osmotic pressure. The still is kept at ∼700 mK as at this temperature the vapour pressure of $^3$He is ∼1000 times higher than the vapour pressure of $^4$He. This optimises the rate of circulation of $^3$He in the system and minimises the amount of $^4$He which can enter the vapour phase in the still. Once the extracted $^3$He reaches the top of the refrigerator, it is recycled and once more flows downwards to the mixing chamber, creating a continuous cooling cycle.

## 6.4 Polarisation of the Target using Dynamic Nuclear Polarisation (DNP)

The protons and electrons in the target material have an intrinsic spin quantum number of $s = 1/2$, and therefore two spin substates, $m = \pm 1/2$, where $m$ is the magnetic quantum number. These spin states are degenerate in the absence of a magnetic field. When FROST is being polarised or is being operated in frozen spin mode, the presence of the magnetic field breaks the degeneracy of the two states to make them occur at different energies (Zeeman Splitting) as can be seen in Figure 6.4.

The energy difference between the two states, $\Delta E$, depends on the strength of the applied magnetic field, $B$, and the gyromagnetic ratio of the particle, $\gamma$ [123]:

$$\Delta E = \hbar \gamma B \tag{6.1}$$

As the gyromagnetic ratio of the proton is positive, its magnetic moment, $\mu_p$, is in the same direction as the spin. The opposite is true of the electron, whose magnetic moment, $\mu_e$, is negative.

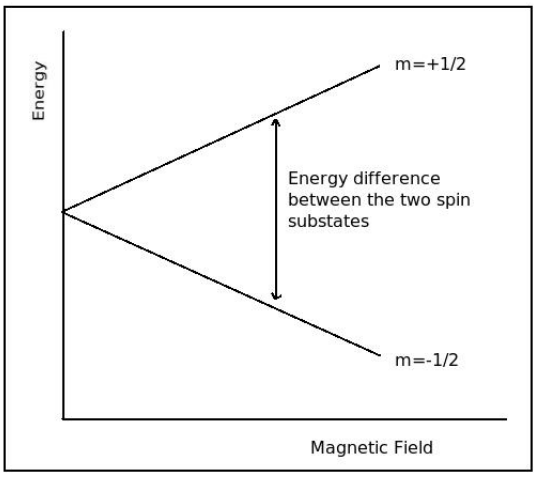


Figure 6.4: Schematic diagram of the Zeeman splitting of a *s = 1/2* particle, where energy of the spin substates is plot as a function of magnetic field strength [122].

In the presence of a magnetic field, the spins will align themselves with or against the field, with slightly more spins aligned with the direction of the field as this corresponds to the lower energy state. In the general case of a spin-*1/2* particle with magnetic moment, $\boldsymbol{\mu}$, the relative populations of the two substates are given by [123]:

$$\frac{N_\beta}{N_\alpha} = exp(\frac{-\Delta E}{kT}) \tag{6.2}$$

where $N_\alpha$ is the number of protons in the lower energy substate, $N_\beta$ is the number of particles in the higher energy substate, $k$ is Boltzmann's constant and $T$ is the temperature in Kelvin. However, the spin cannot align itself parallel to the field lines as this would violate the Pauli principle. For this reason, $\boldsymbol{\mu}$ will precess around this field direction at a fixed angle, $\theta$, given by [122]:

$$E = -\boldsymbol{\mu}.\mathbf{B} = \mu B cos(\theta) \tag{6.3}$$

and at a frequency known as the Larmor Frequency, $\omega_0$, given by [122]:

$$\omega_0 = -\gamma B \tag{6.4}$$

where $\omega_0$=140 GHz for electrons and $\omega_0$=219 MHz for protons in a 5 T magnetic

field.

Aligning the spins in this manner in order to polarise the target is often referred to as "Brute Force" polarisation [124]. For spin-1/2 particles such as protons, the Boltzmann factor indicated by Equation 6.2 leads to the following expression for the target polarisation, $P$, for in a magnetic field, $B$, and at a temperature, $T$ [110]:

$$P = \tanh\left(\frac{\boldsymbol{\mu}.\mathbf{B}}{kT}\right) \tag{6.5}$$

As can be seen from this equation, a high degree of polarisation requires high field strengths and very low temperatures. To avoid this problem, the well-established technique of dynamic nuclear polarisation (DNP) is used to polarise the target [125]. Here the target material is cooled to $\leq$1 K, and placed inside the field of a powerful "polarising" magnet so that the free electrons are highly polarised using "brute force". FROST utilises a polarising temperature of $\sim$0.3 K and a field of 5 T [108]. Due to their higher magnetic moment ($\mu_e \sim 660\mu_p$) [106], the free electrons in the target material are almost completely polarised under these field and temperature conditions, while the proton polarisation remains low (see Figure 6.5). The electron polarisation is then transferred to the protons using microwave radiation, DNP being the general term for the several mechanisms through which this process may occur. A brief summary of some of the simpler DNP models will be provided below, a detailed description, however, is beyond the scope of this thesis.

The simplest DNP mechanism for a solid polarised target is the Solid Effect, as developed by Abragam and Proctor in 1958 [126]. In this model the electron and proton spins are coupled through the electron's magnetic field resulting in an admixture of states and a non-vanishing probability of mutual spin-flips between an electron and a proton, as shown in Figure 6.6. If energy is provided to the system (in this case in the form of microwaves), the spins of an electron and proton can flip simultaneously.

Also shown in Figure 6.6 are two examples of possible spin transitions. At 5 T and at $\sim$0.3 K, electrons will be in the spin down state, anti-parallel to the magnetic field. By applying energy of the value:

$$E = \hbar(\omega_e - \omega_p) \tag{6.6}$$

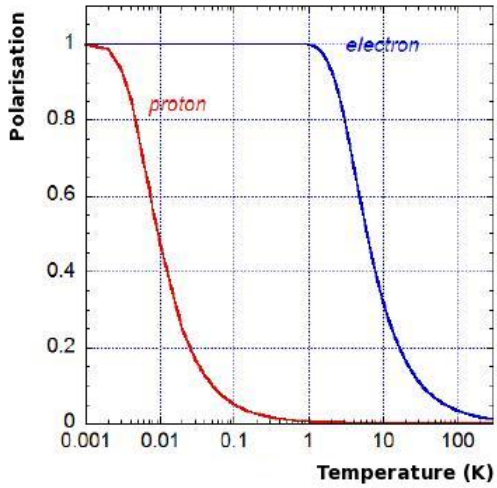


Figure 6.5: Comparison of achievable electron and proton polarisation in a 5 T field [124].

where $\omega_e$ is the electron Larmor frequency and $\omega_p$ is the proton Larmor frequency, an electron can flip to the spin up state along with a proton. As the electron relaxation time is short ($\sim 10^{-3}$ s) compared to the spin relaxation rate of the nucleon ($\sim 10^{3}$ s) [106], the electron will return quickly to its spin-down state and flip the spins of further protons to the spin-up state. As a result, one electron is capable of transferring polarisation to $\sim 10^{3}$ free protons [124]. The choice of temperature and magnetic field is made to minimise the electron relaxation time and maximise the nuclear relaxation time to achieve the highest degree of polarisation possible [108].

If the target is to be polarised in the opposite direction, energy of the value:

$$E = \hbar(\omega_e + \omega_p) \tag{6.7}$$

is applied to the target. In this case, electrons with spin down will flip to the spin-up state, simultaneously flipping protons with spin up to the spin-down state.

The description above is often referred to as the "Resolved Solid Effect" as the proton and electron spin resonance lines are easily resolved from one another. The Resolved Solid Effect therefore requires the width of the electron spin resonance (ESR) line to be narrow compared to the nuclear Larmor frequency.

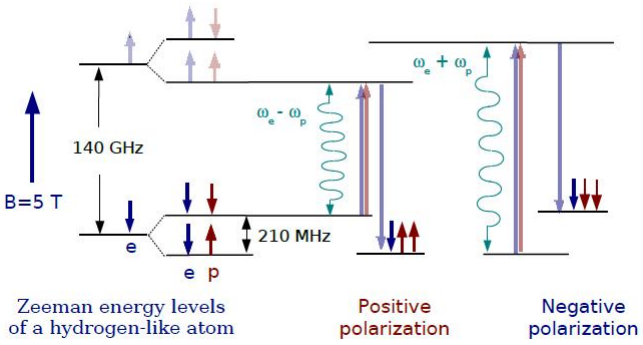


Figure 6.6: Schematic diagram of the resolved electron and proton spin states and possible transitions between them [124].

As an extension to this model, the Differential Solid Effect takes into account effects such as dipolar coupling between the electrons or an anisotropy in the electrons' g-factor, which results in a slight broadening of the ESR line. In this case, a range of microwave energies can cause a transition from one spin state to the other and it is no longer possible to excite one particular electron/proton spin flip transition without also partially exciting the opposite transition. This means that the maximum achievable polarisation of the material is now lower than for the "ideal" case of the Resolved Solid Effect.

If, however, the ESR line is significantly broadened such that its width approaches the nuclear Larmor frequency, DNP can still occur. For example, the Cross Effect is thought to be the dominant spin transfer mechanism in such systems [127]. In this model, two electrons of opposite spin with a broadened line can provide the correct energy to flip a nearby proton. This will occur if the Larmor frequencies of the two electrons, $\omega_{e1}$ and $\omega_{e2}$, differ by exactly the Larmor frequency of the proton:

$$\omega_{e1} - \omega_{e2} = \omega_p \tag{6.8}$$

As the density of free electrons increases, dipolar coupling between the centres produces a homogeneously broadened ESR line. Here as well as in the case of lines exhibiting both homogeneous and inhomogeneous broadening the Thermal Mixing process is believed to be responsible for DNP [125]. The idea

of flipping spins is no longer considered: polarisation occurs by the transfer of energy between the energy states of the Nuclear Zeeman Effect, the Electron Zeeman Effect, and the dipolar coupling between the electrons. Each of these three systems can be viewed as a "thermal reservoir", described by a "spin temperature" which characterises the Boltzmann populations of the various energy levels. Microwave radiation near the Larmor frequency changes the population distribution of the dipolar reservoir, effectively cooling or heating it to a spin temperature that is below or above the temperature of the electron Zeeman reservoir. The latter can be regarded, to a first approximation, as the Lattice Temperature which experimentally is the temperature of the helium bath surrounding the material. If the width of the ESR line is close to the Larmor frequency, the nuclear Zeeman and Spin-Spin Temperatures are comparable in size and so an exchange of energy may occur between these two systems until the two temperatures are equal. As a result, the spin temperature of the nuclear Zeeman states will decrease or increase alongside that of the dipolar states. This is possible because the nuclear spins are in better thermal contact with the electron spins than with the lattice. In effect, Thermal Mixing replaces the Lattice Temperature of Equation 6.5, with a much lower spin temperature.

Microwave irradiation below the electron Larmor frequency, $\omega_e$, "cools" both the dipolar and nuclear spin thermal reservoirs and results in a positive spin temperature, meaning that the majority of the nuclei will be in the lower spin state (positive polarisation). Irradiation above $\omega_e$ results in "population inversion" of the spin states that is described by a negative spin temperature and hence an enhanced negative polarisation of the proton spins. Thermal mixing is the dominant polarisation mechanism for most current target materials, including TEMPO-doped butanol.

Once polarised the protons naturally go through the process of relaxation in a characteristic time, $T_1$, in which the spins return to their equilibrium with the lattice temperature. This process is known as Spin-Lattice Relaxation [126] and is the result of the fluctuation of the local magnetic field in the vicinity of the proton. This is dominated by the thermal motion of nearby electron spins and is therefore strongly dependent on temperature as well as magnetic field. The decay of polarisation due to spin-lattice relaxation is described by [124]:

$$P(t) = P_{TE} - P_{TE}exp(\frac{-t}{T_1}) \tag{6.9}$$

where $P$ is the polarisation of the target, $P_{TE}$ is the thermal equilibrium polarisation and $t$ is time.

The polarising magnet for this experiment (Figure 6.7) is a 5.1 T superconducting solenoid bought from Cryomagnetics Inc [59], producing a field uniform to $\Delta B/B < 3 \times 10^{-5}$ over the volume of the polarised target, 15x50 mm [109]. The microwave generator used for the polarisation process is an extended interaction oscillator (EIO), as this is the highest power microwave generator available at frequencies ∼140 GHz, and it can be tuned over a bandwidth of 2 GHz [108]. The frequency is measured with a frequency counter, and the tube power is monitored by a temperature-compensated thermistor [124]. Rectangular waveguides outside the cryostat and a CuNi tube inside transmit the microwaves to the target [124].

Figure 6.7: Photograph of the 5.1 T polarising magnet [110].

## 6.5 Operation of the target in Frozen Spin Mode

Once the target polarisation is sufficiently high so that it can be inserted into the detector, the microwave generator and magnet are switched off, while the target is cooled to <0.05 K [124]. At the same time, a thin solenoid surrounding the target is switched on to create the 0.56 T [124] holding field. The holding coil

(Figure 6.8) is a small, superconducting solenoid made of three layers of 785 turns of NbTi wire with a fourth layer of 162 turns at each end to trim the magnetic field. Its field is uniform to $\Delta B/B < 3 \times 10^{-3}$ [109], in order to resolve the proton NMR line so that NMR measurements can be made during the experiment. The compact design of the holding coil contributes to the field homogeneity, and also means that it has a weak outer fringe field which does not influence the detectors close to the target or the paths of the charged particles entering the detectors. Both the coil windings and the aluminium mandel on which they are wound are thin (∼0.3 mm and 1 mm respectively [112]) so that the energy loss of scattered particles is kept to a minimum. Unlike the polarising magnet, the holding coil is mounted inside the refrigerator.

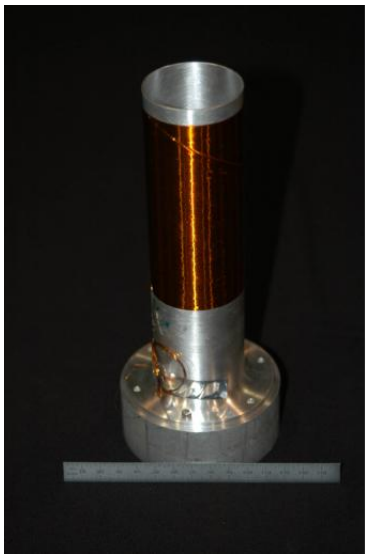

Figure 6.8: Photograph of the holding coil for longitudinal polarisation [128].

DNP takes a few hours for high target polarisations ∼80% to be achieved and then cooling the refrigerator to below 50 mK for frozen spin operations takes ∼45 minutes. Once the required temperature is achieved, the target can be moved into the centre of CLAS. Data taking can then begin for 5-10 days, after which the target has to be repolarised. With the holding field present and the target cooled to ≥30 mK (∼32 mK with beam [112]), the polarisation typically decays at a rate of only ∼1% per day [124] with the degree of polarisation during beam-time monitored online using NMR techniques.

For the *g9b* experiment transverse polarisation and therefore a transverse

holding field was required. In this case, the holding coil is a dipole magnet made of racetrack shaped coils wrapped around a cylinder as shown in Figure 6.9. Both coils were produced by the Jefferson Lab Polarised Target Group, with early transverse coil prototypes constructed with contributions from the Edinburgh and Glasgow Nuclear Physics Groups.

Figure 6.9: Photograph of the holding coil for transverse polarisation [128].

## 6.6 The NMR Technique

Positive polarisation in the target material corresponds to the majority of protons being in the lower spin state, and for negative polarisation the majority of protons are in the higher spin state. This leads to a large population difference between the spin substates. If electromagnetic (EM) radiation at the Larmor Frequency is now applied to the protons it can either be absorbed or emitted resulting in a flip of one state to another. This flip induces a current in the NMR coils surrounding the detector and a magnetic resonance is detected.

In the process of continous wave NMR (CW-NMR), a coil wound around the target produces radiofrequency (RF) radiation perpendicular to the magnetic field in order to flip the nuclear spin. However, as the spin energy levels and hence the resonance line have finite widths, the RF frequency has to be swept over a range close to $\omega_0$. For FROST experiments this corresponds to a sweep width of 212.2 MHz to 213.0 MHz, performed from lower to higher frequency

and then reversed. Usually 100 of these double sweeps will be performed and the result averaged before the spectrum is recorded. The circuit diagram of the NMR system used to measure the degree of polarisation of FROST is shown in Figure 6.10. This circuit consists of a coil of inductance, $L$, wrapped around the target material, and attached to a Liverpool Q-Meter Circuit by a coaxial transmission cable (Figure 6.11).

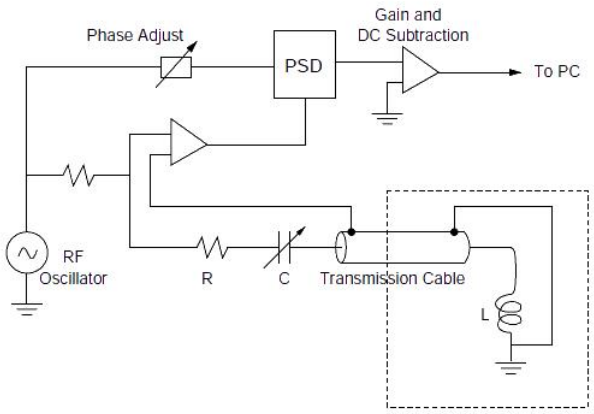


Figure 6.10: Schematic diagram of the Q-Meter circuit [108]. The components within the dashed lines are cooled by the dilution refrigerator system.

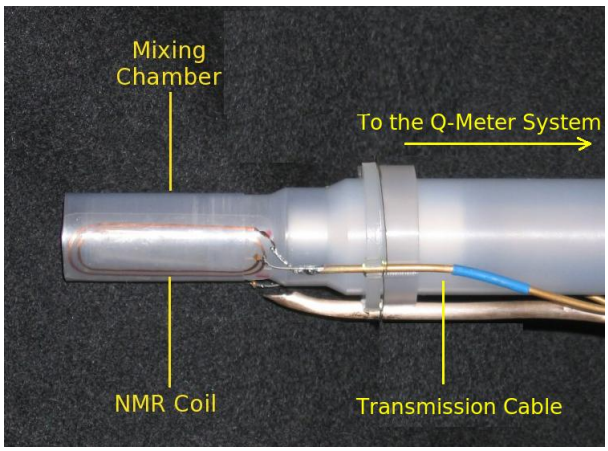


Figure 6.11: Photograph of the low field NMR coil and transmission cable [129]. A second NMR coil is used for the high field NMR measurements.

The cable length was chosen to be $n\lambda/2$ at $\omega_0$ to create a resonant RLC circuit. The complex magnetic susceptibility, $\chi(\omega)$, of the target material is given by [130]:

$$\chi(\omega) = \chi'(\omega) - i\chi''(\omega) \tag{6.10}$$

where $\chi''(\omega)$ is determined by the energy absorbed or transmitted during a transition between energy levels. As this is completely dependent on the population of the energy states, $\chi''(\omega)$ is a direct measure of the polarisation of the target material. $\chi(\omega)$ changes as the RF frequency is swept close to the Larmor frequency thus altering the inductance of the coil. This in turn modifies the complex impedance, $Z(\omega)$, of the circuit by [130]:

$$Z(\omega) = R + i\omega L[1 + \eta\chi(\omega)] \tag{6.11}$$

where $\eta$ is the effective filling factor of the target. The constant current resistor, $R_c$, and the damping resistor, $R_d$, allow the coil current to be kept constant and so the change in impedance of the circuit can be measured as a change in voltage across the circuit.

The real part of the voltage change is measured by a phase sensitive detector (PSD). This has two input ports: one for a high level constant amplitude reference signal, and the other for the signal from the circuit. The output is proportional to $V\cos\phi$, where $V$ is the amplitude of the voltage from the circuit and $\phi$ is the phase difference between the two signals [131]. If $\phi$ is set to zero, then the real (absorptive) part of the RF signal is measured.

## 6.7 Data Acquisition and Computer Control of the Target Systems

There are two hardware systems used to control and monitor FROST. EPICS (Experimental and Industrial Control Software) is used to control the cryogenic systems for the target. This is a software environment developed by the Argonne National Laboratory and is used to develop control systems for large experiments and particle accelerators [132]. This runs on a VME-based single board computer in the experimental hall [108].

The data acquisition and instrument control software for the target is based on the Labview 5.2 package, a graphical programming environment developed by National Instruments [133]. Labview is used to control the NMR system, the polarisation and holding magnets and monitors both the frequency and power of the microwave system. This control system operates from a Linux PC in the experimental hall which can be accessed from the Hall B control room to control the NMR system during frozen spin mode.

## 6.8 Analysis of NMR Data

The NMR data were transferred to Edinburgh in text file format in order to be analysed by the author using the CERN software package, ROOT [134]. The data files contained voltage (scan data) vs. deviation of RF frequency from the Larmor frequency. The absorptive part of the complex susceptibility of the circuit is related to polarisation by [130]:

$$P = C \int_{\Delta\omega} \chi''(\omega) d\omega \tag{6.12}$$

where $C$ is a proportionality factor and $d\omega$ is the resonance frequency region.

As $\chi''(\omega)$ is measured as a change in voltage, it has been shown by Abragam and Goldman [125, 135] that the area under the NMR curve is proportional to the polarisation of the target material:

$$P = C \int_{\Delta\omega} V(\omega) d\omega \tag{6.13}$$

The constant of proportionality, $C$, varies greatly according to several circuit and target parameters so it cannot be measured directly. Instead, NMR spectra are obtained for the material polarised under conditions of thermal equilibrium where the spin states are populated according to Boltzmann statistics and where the polarisation can be accurately calculated using Equation 6.5. Here a thermal relaxation mechanism puts the nuclear spin in contact with the lattice, and as the lattice is in thermal equilibrium with the refrigerator, a precise measurement of temperature can be made. For FROST these measurements were made at 1.01 and 1.5 K in a 5 T magnetic field, where $\omega_0 \approx 212.6$ MHz [108]. Under these conditions, FROST was used as a $^4$He evaporation refrigerator where

the $^3$He/$^4$He mixture was replaced with superfluid $^4$He, ensuring a uniform temperature throughout the target material.

The calculation of target polarisation was therefore performed in two stages:
i) The first was to find the constant of proportionality henceforth referred to as the "calibration constant", $C$, using the equation:

$$C = \frac{A_{TE}}{P_{TE}} \tag{6.14}$$

where $A_{TE}$ is the area of the NMR spectra and $P_{TE}$ is the polarisation at thermal equilibrium.
ii) The second was to use this value of calibration constant to calculate the average target polarisation per run during the experiment.

The calculation of the calibration constant will be described in detail in the next section and the calculation of the target polarisation in Section 6.12.

## 6.9 Calculation of Calibration Constant, $C$

An example of the NMR thermal equilibrium spectrum obtained is shown in Figure 6.12 below.

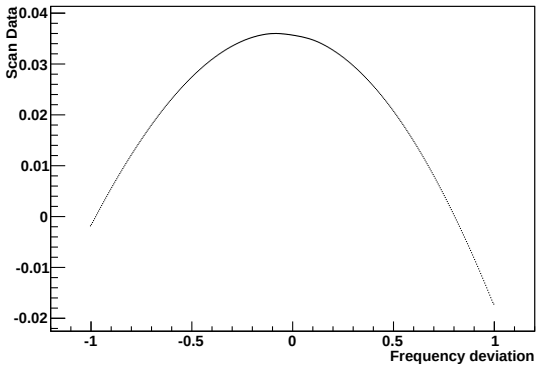


Figure 6.12: Example of a raw thermal equilibrium spectrum. The frequency deviation scale ranges from -1 to 1, where 0 corresponds to the resonant frequency, $\omega_0 \approx 212.6$ MHz, and the extremes of the scale correspond to $\omega_0 \pm 400$ kHz.

This "raw" spectrum shows a parabolic background signal, referred to as the "Q-Curve" superimposed on the proton resonance signal. This is a result

of changes in the effective impedance of the circuit as the frequency is scanned due to temperature fluctuations [136]. The Q-Curve is measured by lowering the magnetic field by ∼1% so that the resonance signal is out of range of the frequency scan, the resulting spectrum being known as the "baseline". The Q-Curve was measured at regular intervals during the data taking at thermal equilibrium. The "true" NMR spectrum is obtained by subtracting the baseline from the raw spectrum as can be seen in Figure 6.13.

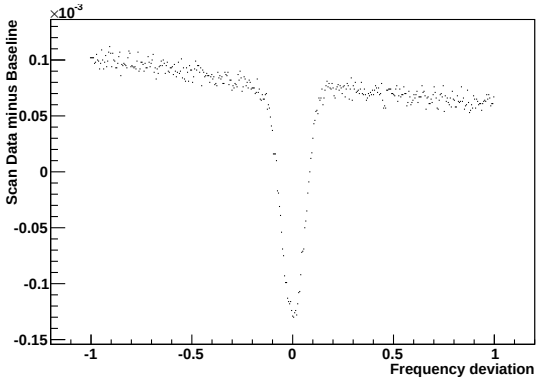


Figure 6.13: Example of a thermal equlibrium spectrum with baseline subtracted.

In principle the NMR spectrum in Figure 6.13 should be a flat line at 0 V with a peak in the centre described by a Lorentz function. However, the wings of the spectrum are not flat showing that there is still a residual Q-Curve. This is often due to a thermal change in some part of the circuit between measuring the baseline and the target polarisation signal. It was found that a second background subtraction had to be performed before the area could be calculated; simultaneous fits to the background and peak did not give fits of sufficient quality as the detailed shape of the peak was unknown.

Almost 200 thermal equilibrium signals were measured, with frequency deviation, baseline and scan data recorded. The first 73 measurements were made at $T$=1.01 K and $B$=5 T, and a second set of 100 measurements was also taken at $T$=1.5 K and $B$=5 T. It was necessary to make as many measurements as thermal equilbrium polarisations are low (∼0.18% at 1.01 K and 5 T, ∼0.12% at 1.5 K and 5 T) hence significant signal averaging is required for an accurate determination of the calibration constant.

Several approaches were taken to calculate the area of the NMR signal minus the background contribution. The chosen procedure was to fit a third order polynomial across the wings of the spectra and then subtract this from the whole spectrum. An example of the resultant corrected NMR spectra is shown in Figure 6.14. A linear fit to the region of the wings results in an average value of $\sim 10^{-18}$ V, which is a negligible contribution to the systematic error. The area could now be calculated as a sum of the voltage at each frequency point over the scanned range, which is equivalent to the integral of the function which describes the spectrum.

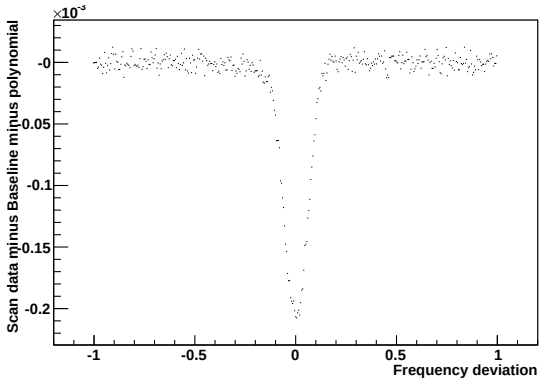


Figure 6.14: Example of a thermal equilibrium spectrum once both baseline and fitted polynomial have been subtracted.

The average area of the spectra was calculated arithmetically and was found to be -0.006 $\mathrm{Vs}^{-1}$ at $T = 1.1$ K and -0.044 $\mathrm{Vs}^{-1}$ at $T = 1.5$ K. The error in these values contributed to the statistical error in the calibration constant. Combining these values with the temperature of the target and the Larmor frequency, the value of polarisation could now be calculated. The temperature of the mixing chamber and hence the target was measured using a Ruthenium Oxide temperature sensor [1] [112] and the Larmor frequency was calculated from the centroid of the NMR peak. The magnetic field is related to the Larmor frequency $\nu$ by [123]:

$$\gamma B = 2\pi\nu \tag{6.15}$$

[1] LakeShore Cryotronics, Model RX202A-AA

where $\gamma$ is the gyromagnetic ratio, which can in turn be calculated using the formula [123]:

$$\gamma = \frac{\nu}{m\hbar} \tag{6.16}$$

where *m = 1/2* for the proton. Substituting these expressions into Equation 6.5, allowed the polarisation at thermal equilibrium to be calculated:

$$P_{TE} = \tanh\left(\frac{\pi\hbar\nu}{kT}\right) \tag{6.17}$$

Using this formula, the average polarisation was found to be -0.0050 ± 0.0008 (SYS) at $T = 1.1$ K and -0.0033 ± 0.0008 (SYS) at $T = 1.5$ K, where *SYS* refers to the systematic error. The statistical error in both cases was negligible ($\sim 10^{-7}$).

The systematic component of the error originates from the calibration of the temperature sensor, carried out by the manufacturers from 0.05 K to 40 K at 0 T with an uncertainty of ±0.016 K at $T$=1.4 K and $B$=5 T [137]. However, as the thermal equilibrium measurements were taken in a 5 T magnetic field, a correction was required to take into account the magnetoresistance of the thermometer [112], *i.e.* the temperature reading of the thermometer did not correspond to the actual temperature of the target.

An estimate of this correction to the temperature reading was obtained [112] by comparing the resistance of the thermometer to $^4$He vapour pressure curves at 5 T, as shown in Figure 6.15. The resistance of the sensor was measured at different values of $^4$He pressure and compared to the data provided by Lakeshore Cryotronics; overall a ∼1% increase in the resistance of the sensor was observed, allowing for a small correction to be made to the temperature indicated on the thermometer during thermal equilibrium measurements. The uncertainty in the magnetoresistance of the temperature sensor was quoted as 0.5% by the manufactuers, leading to an additional systematic uncertainty in the temperature measurement.

The statistical error in the polarisation measurement originates from the statistical error in the temperature measurement. This was simply calculated as the standard error in the mean of the temperature measurements used in the calculation.

The average area of the NMR spectra and the average polarisation were then

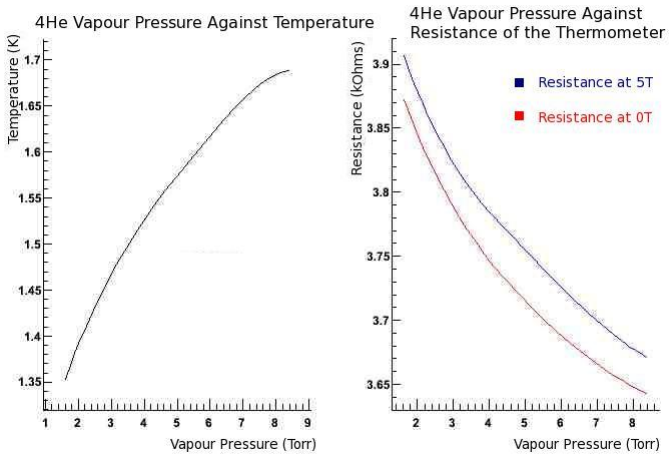


Figure 6.15: Figure above left showing $^4$He vapour pressure as a function of temperature, and above right showing the change in resistance of the Ruthenium Oxide temperature sensor as a function of $^4$He vapour pressure at 0T and at 5T [112].

used to calculate the calibration constant using Equation 6.14.

## 6.10 Further sources of error in the Calculation of $C$

The contribution of two further sources of systematic error in the calculation of the calibration constant were carefully assessed. The first source was the baseline subtraction. The baseline was measured regularly during data taking as its shape and position change with the tune of the NMR circuit. A "good" baseline subtraction was defined as that which produces the least slope in the wings of the NMR spectra. For the TE data set at 1.01 K, there were nine different baselines, corresponding to eight "groups" of spectra. The spectra were analysed using the original baseline, the baseline from the following group and also using an average of these two baselines. In each case the gradient of the wings of the spectra were calculated, the spectra with a gradient closest to zero being selected to calculate the calibration constant. Figure 6.16 shows the effect of swapping baselines on the spectra.

The maximum difference between the optimum value of the calibration

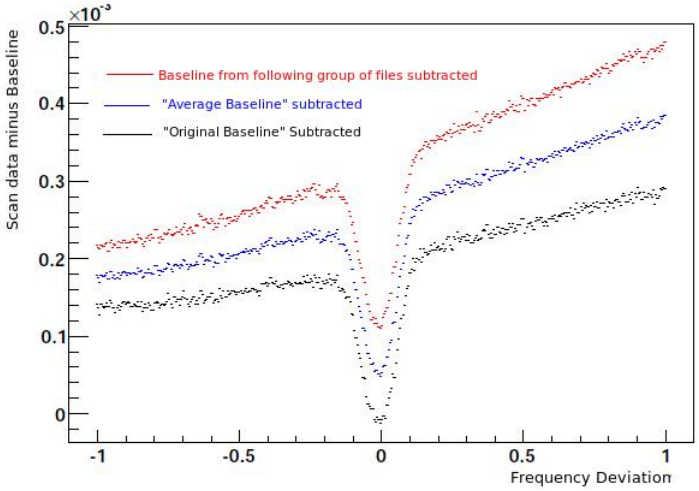


Figure 6.16: NMR spectra showing the effect of subtracting different baselines from the same scan data.

constant and the other values of $C$ resulting from different baseline subtractions was of the order of $10^{-3}$. The systematic error in the calibration constant due to the baseline subtraction was then calculated as the standard error in the value of the calibration constant obtained from each baseline subtraction.

The second source of systematic error was "contamination" of the target by any other material in the target cup containing protons, which would artificially increase the area of the NMR spectra. The target and target system are made of metals and fluorocarbons, so only the protons in the butanol target should contribute to the NMR signal. To confirm that this was the case, NMR data was taken at $T$=1.057 K when the target cup contained no butanol beads, and the same procedure as above used to find the area.

It was found that the average area of these spectra was $\leq$1% of that for the TE signals and that adding a correction to the calibration constant for the empty target signals made negligible difference to the value of $C$.

## 6.11 The Calibration Constant

The calibration constant was calculated for both the 1.045 K and the 1.5 K data sets, the values of which are: $0.799 \pm 0.002\ (STAT) \pm 0.013\ (SYS)$ at $T = 1.1K$ and $0.774 \pm 0.011\ (STAT) \pm 0.008\ (SYS)$ at $T = 1.5K$, as shown in Figure 6.18

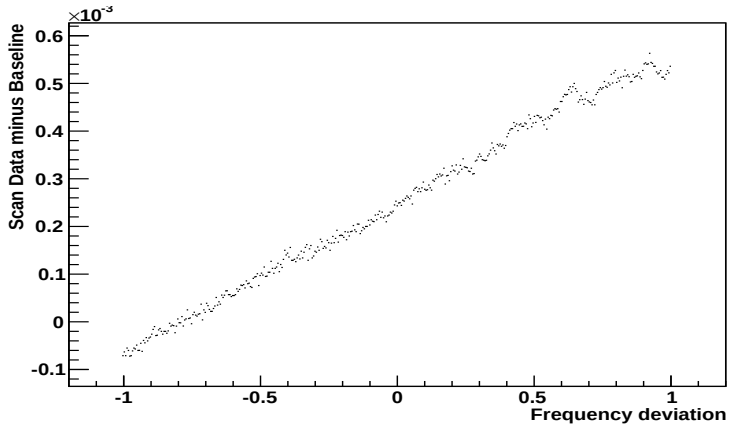


Figure 6.17: Example of an NMR spectrum recorded when the target was empty.

and where *STAT* refers to the statistical error and *SYS* refers to the systematic error as before. The final value of the calibration constant was taken to be the weighted mean of these values:

$$\mathrm{C} = 0.798 \pm 0.002\ (\mathrm{STAT}) \pm 0.013\ (\mathrm{SYS})$$

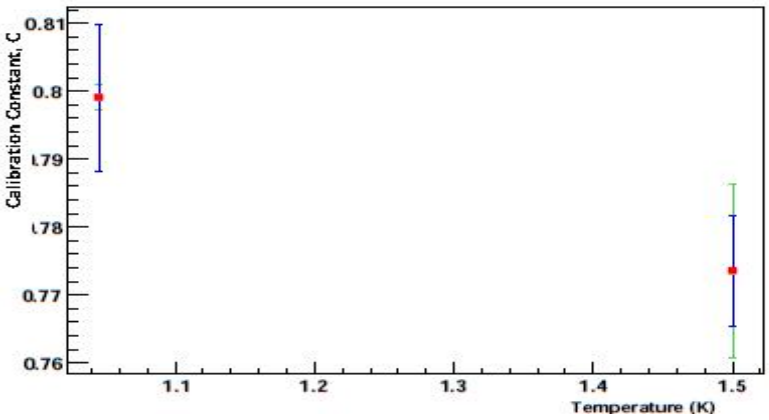


Figure 6.18: Comparison of the two calibration constants calculated from the thermal equilibrium data sets. Green error bars correspond to statistical errors and blue error bars correspond to systematic errors.

## 6.12 Target Polarisation

Once the calibration constant, $C$, had been obtained, the average polarisation per run could be calculated. During frozen spin mode, NMR measurements were taken every 30 minutes (referred to as low field data). NMR measurements were also made every few minutes while the target was being polarised (high field data) and in frozen spin mode before and after repolarisation with no beam on target. Figures 6.19 and 6.20 are schematic diagrams showing how polarisation changes with time.

## 6.13 Calculation of a new calibration constant, $C_{LF1}$

Referring to Figures 6.19 and 6.20, the polarisation, $p_1$, just before frozen spin mode, can be calculated using the value of calibration constant from Section 6.11 and the average area of the last 10 NMR spectra in polarising mode. It can then be assumed that $p_2 \approx p_1$, and so a new calibration constant, $C_{LF1}$, can be calculated from $p_1$ and the average area of the first 10 spectra at the start of holding mode, $A_2$:

$$C_{LF1} = \frac{p_1}{A_2} \tag{6.18}$$

$C_{LF1}$ can be used with the low field NMR areas to calculate the polarisation corresponding to each NMR measurement and hence the average polarisation per run.

In theory $p_3 \approx p_4$ and the areas at the end of holding mode, $A_3$, can also be calculated. Therefore a second calibration constant for the low field data, $C_{LF2}$ can be calculated as before:

$$C_{LF2} = \frac{p_4}{A_3} \tag{6.19}$$

This second low field calibration constant, $C_{LF2}$, should always be equal to $C_{LF1}$.

A comparison the the two low-field calibration constants is shown in Table 6.2. Whereas the two values are very close to each other for the majority of frozen spin cycles, there were occasions where they differed significantly.

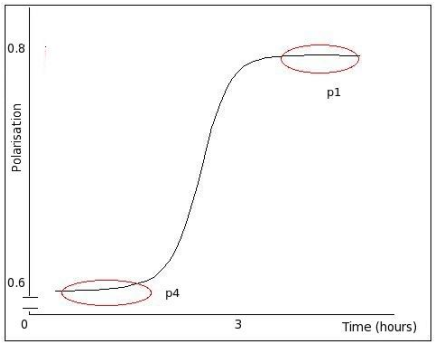


Figure 6.19: Schematic diagram showing how polarisation changes with time during the polarisation process. $p_1$ and $p_4$ are the polarisations of the end and beginning of the polarisation mode respectively. These were determined using the "high field" NMR coil.

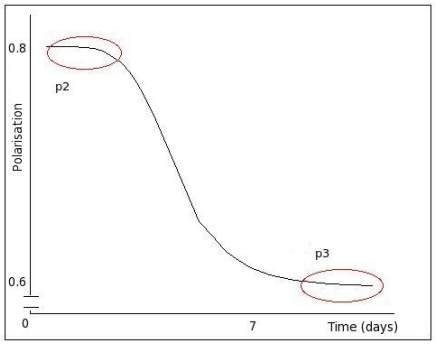


Figure 6.20: Schematic diagram showing how polarisation changes with time in frozen spin mode. $p_2$ and $p_3$ are the polarisations of the beginning and end of the frozen spin mode respectively. These were determined using the "low field" NMR coil.

Table 6.2: Comparison of low-field and high-field calibration constants. "No value" refers to periods where there was a break in the NMR data taking, for example during the Thanksgiving Holiday.

| *p1* LF Calibration Constant, $C_{LF1}$ | HF Calibration Constant, $C_{LF2}$ |
|---|---|
| 0.151 | 0.011 |
| 0.134 | 0.017 |
| 0.119 | 0.014 |
| 0.101 | 0.001 |
| 0.130 | 0.127 |
| 0.127 | 0.123 |
| 0.134 | 0.123 |
| 0.143 | 0.131 |
| 0.133 | No value |
| 0.136 | 0.005 |
| 0.134 | 0.130 |
| 0.149 | 0.127 |
| 0.133 | 0.129 |
| 0.138 | 0.129 |
| 0.136 | 0.007 |
| 0.139 | 0.012 |
| 0.147 | No value |
| 0.138 | 0.131 |
| 0.132 | 0.130 |

The anomalous values have been attributed to the design of the high field NMR coil. It appeared to be more sensitive to the polarisation of the downstream end of the target, which loses polarisation more quickly than the upstream end as it is more sensitive to pair production by the beam inside the target. This would only effect the high field measurements at the start of polarising mode, after the target has been irradiated with the photon beam. For this reason the high field areas used to calculate the anomalous values of $C_{LF2}$ were much smaller than expected. The values of $C_{LF1}$ calculated were in general consistent with each other over the whole running period and so the calculation of target polarisation could be carried out. This does not effect the calculation of target polarisation as the calculations can be performed using NMR spectra from the end of polarising mode and the start of holding mode ie. a new cycle.

The design of the NMR coils has now been changed for the *g9b* experiment in order to avoid this problem in future. The high field and low field NMR

measurements are now performed using a single coil. This has no effect on the calculation of target polarisation performed here, but means that for the *g9b* run, polarisation can be calculated using $C_{LF1}$ and $C_{LF2}$, providing a cross-check.

## 6.14 Sources of Error in $C_{LF1}$

Table 6.3 shows the values of $C_{LF1}$ calculated for each polarisation cycle along with their systematic and statistical errors. The only source of systematic error in the calculation of $C_{LF1}$ originates from the systematic error in the thermal equilibrium calibration constant, $C$. The statistical error in $C_{LF1}$ originates from two sources: the statistical error in $p_1$ which comes from the standard error in the areas, $A_1$, combined with the statistical error in the value of the thermal equilibrium calibration constant, $C$; and the standard error in the average value of areas $A_2$.

Table 6.3: Table showing final values of the low-field calibration constant for each holding cycle. The calculations of the errors are explained in the text.

| *p1* LF Calibration Constant, $C_{LF1}$ | Statistical Error | Systematic Error |
|---|---|---|
| 0.151 | 0.003 | 0.002 |
| 0.134 | 0.001 | 0.002 |
| 0.119 | 0.001 | 0.002 |
| 0.101 | 0.001 | 0.002 |
| 0.131 | 0.001 | 0.002 |
| 0.127 | 0.001 | 0.002 |
| 0.134 | 0.001 | 0.002 |
| 0.143 | 0.015 | 0.002 |
| 0.133 | 0.001 | 0.002 |
| 0.136 | 0.001 | 0.002 |
| 0.135 | 0.001 | 0.002 |
| 0.149 | 0.001 | 0.003 |
| 0.133 | 0.001 | 0.002 |
| 0.138 | 0.001 | 0.002 |
| 0.137 | 0.001 | 0.002 |
| 0.139 | 0.001 | 0.002 |
| 0.147 | 0.013 | 0.002 |
| 0.138 | 0.001 | 0.002 |
| 0.132 | 0.001 | 0.002 |

## 6.15 Calculation of target polarisation per run

Figure 6.21 shows the change in target polarisation over both polarising and holding modes. The polarisation during holding mode was obtained by multiplying the low field spectra areas by $C_{LF1}$.

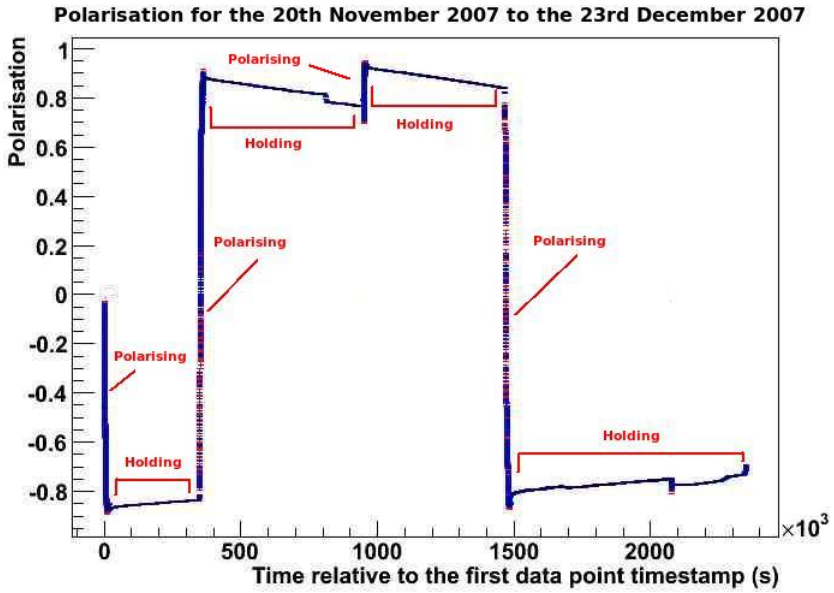


Figure 6.21: Plot showing the change of polarisation with time in both holding and polarising mode.

Each NMR spectrum obtained and hence each value of polarisation calculated in holding mode has a timestamp associated with it. The polarisations measured between the start and end times of each run were then averaged and this average polarisation used in analysis of photoproduction data from the *g9a* experiment.

The main limitation in using low field data taken during runs to calculate the target polarisation, is that on some occasions no NMR data exists. This may occur for short runs $\leq$30 minutes long, which "miss" the NMR sweeps. As can be seen from Figure 6.21, polarisation changes by $\sim$10% over several days. For this reason the polarisation closest to the time of the run was taken as the average polarisation during the run.

Additionally for two groups of runs from the 12th November 2007 to the 13th November 2007 and on the 3rd February 2008 no low field data exists due to data acquistion problems. The runs affected occur at the end of the holding cycle,

so by extrapolating the polarisations of the preceding runs, an estimate of the polarisation during these periods was obtained. If it is assumed that relaxation of the protons in the target follows an exponential decay:

$$P \propto Be^{-kt} \tag{6.20}$$

where $B$ and $k$ are constants and $t$ is time, taking the natural log of this expression shows that a plot of $lnP$ against time, $t$, should produce a first order polynomial fit from which polarisations can be extrapolated (Figure 6.22):

$$lnP = lnB - kt \tag{6.21}$$

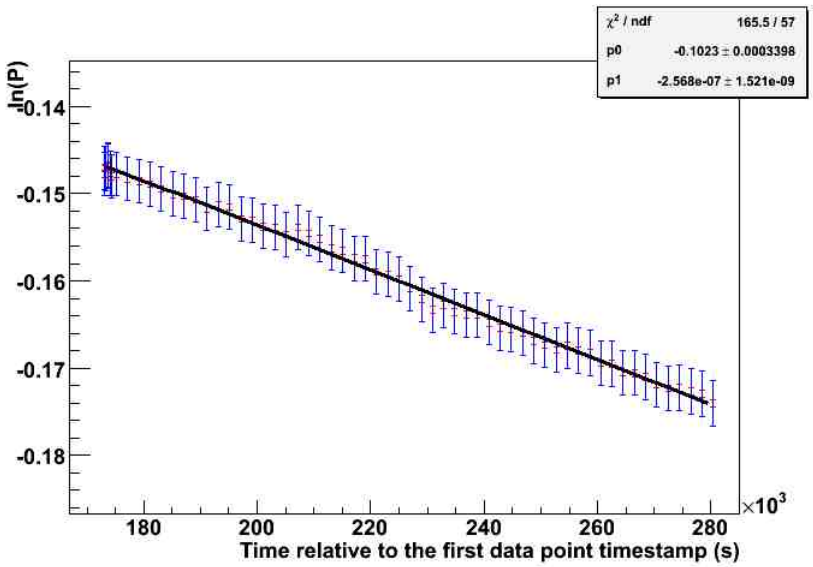


Figure 6.22: Plot of lnP against time for the polarisation data. Statistical errors are in red, systematic errors in blue.

## 6.16 Sources of error in the calculation of polarisation per run

The systematic error in the polarisation corresponding to each indvidual NMR scan in holding mode was simply obtained from the systematic error in $C_{LF1}$. The systematic error in the extrapolated polarisation values for runs where no

low field data is available is the same as the systematic error in the polarisation during the holding cycle they correspond to. However, it was possible that the experimental data did not follow the expected exponential decay, resulting in a further source of systematic error. The $lnP$ against time graphs were also fit with second, third, fourth and fifth order polynomials. For each fit the $\chi^2/ndf$ value was calculated. The fit with a $\chi^2/ndf$ closest to 1 was said to be the "best fit". This function was then extrapolated and the difference in the polarisation obtained with the first order polynomial and the best fit function calculated. This difference was then added in quadrature to the systematic error.

The statistical error in the polarisation corresponding to each indvidual NMR scan in holding mode was simply obtained from the statistical error in $C_{LF1}$. For the groups of runs where no NMR data was available, the an additional statistical error in the natural log of the polarisation, $\delta(lnP)$, was obtained from the error in the fit parameters as shown in Figure 6.22.

## 6.17 Conclusions

It was found that FROST was polarised to between ∼85% and ∼90%, and in general would decay over several days by ∼10%. The average statistical error in the target polarisation was found to be ∼0.034% and the average systematic error to be ∼1.86%. The errors in this calculation have been reduced compared to previous estimates by averaging the NMR signals and other calculated values where possible to reduce standard deviation and hence systematic error, as well as through a detailed study of the optimum technique to perform background subtractions from the NMR signals. The results of these calculations will now be used in the analysis of photoproduction data to measure double polarisation obervables in pion photoproduction as described in this thesis, as well as by colleagues analysing other channels in the *g9a* experiment.

# Chapter 7

# Detector Calibration

## 7.1 Introduction

Before the data can be analysed, the raw ADC and TDC signals must first be converted to physical values for the detected particles such as time, energy and momentum. This calibration process must be repeated for every CLAS experiment due to changes in experimental setup and detector performance. This chapter provides a brief description of the calibration processes required by the *g9a* experiment. All calibrations and calculations of parameters such as the beam and target polarisations were carried out as a collaboration, with each member University having responsibility for one of these tasks. As noted in the previous chapter, the author was primarily responsible for calculating the target polarisation; the calibrations described in this chapter were carried out by colleagues within the FROST group. However, the author was responsible for implementing the calibrations and for checking the consistency and accuracy of the detector systems.

The initial calibrations were carried out at the end of the experiment on an agreed set of runs, usually one run for each set of specific run conditions. For example, for the *g9a* experiment, one run would be chosen for each circularly polarised photon beam setting and one run for each linearly polarised photon beam setting. This initial calibration then produces a set of calibration constants which can be applied to all of the raw data.

There are some corrections made to the ADC and TDC values which are common to all detector subsystems. For example, the ADC values require a

correction to take into account any residual current in the device. This is known as the "pedestal" and applied as a correction to all signals. The pedestals are supressed from being read out to the data stream in normal running but can be evaluated from dedicated unsupressed experimental runs.

The TDC values must all be corrected for "time-walk", a pulse-height dependent shift in timing that results from larger signals rising faster and thus reaching the discriminator threshold level sooner than a smaller signal, as demonstrated in Figure 7.1. The time-walk correction differs slightly for each detector subsystem, requires a dedicated laser run where light pulses of varying pulse height from a laser were applied to the detector counters and the resulting TDC signal heights plot as a function of time. Details specific to each detector will be described below.

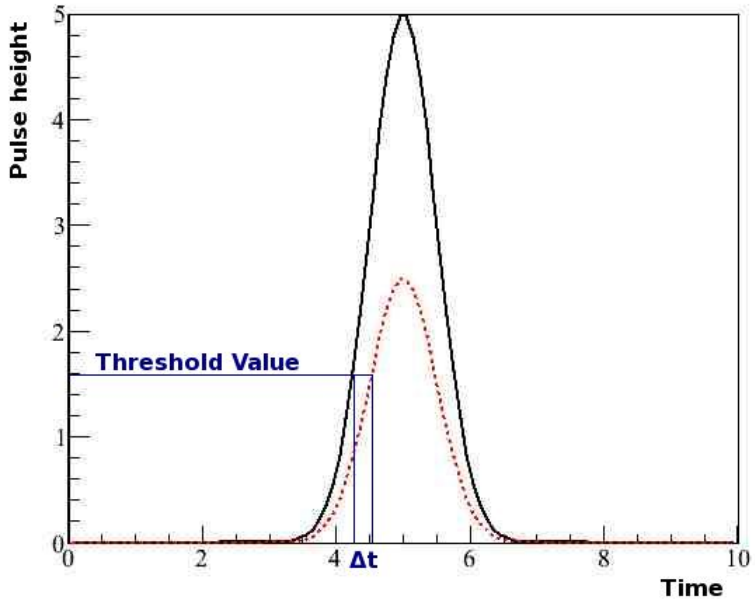


Figure 7.1: Diagram showing the effect of pulse height on the rise time of a signal. The time difference, $\Delta$t, between the two signals reaching the threshold value is known as the "time-walk" and must be corrected for as explained in the text.

Before timing calibrations begin, the TDC values must be converted from TDC channel number to time in ns. A pulsed-signal run was performed for all detector subsytems simultaneously (with the exception of the drift chambers) in order to calculate a channel-to-time conversion constant. 4000 pulsed logic signals

at a fixed interval were sent simulataneously to all TDCs. These pulses were delivered in groups of 50 with a constant time interval, the time interval increasing by 2 ns for each group [138]. Plotted as a function of time, the TDC channels could be fit with a linear function and the fit parameters used to determine the channel-to-time conversion constants.

Each subsystem must be calibrated in a specific order as the definition of a common time to which all the detector subsystems are aligned means that the timing calibrations are inter-linked. The RF signal of the linacs is used to define timing, with the tagger timing aligned relative to this. The timing of the tagger is then defined as the common "zero" time for all other detector subsystems. As such, the tagger calibration was performed first, followed by the time-of-flight and the start counter. Once the time-of-flight data had been corrected, the drift chambers and electromagnetic calorimeters were then be calibrated. The calibration of each subsystem was performed several times in order to optimise the calibration constants obtained. The results of data reconstruction and calibration are stored by the CSQL package [139] in a mySQL database.

## 7.2 Tagger Calibration

Correct calibration of the tagger time is important as it is used as a reference time by all other detector calibrations, providing the photon time at the event vertex. The time of events recorded by the tagger must be aligned to the timing of Bremsstrahlung photon and reactions in the target. The timing provided by the tagger T-Counters (Figure 5.9) is first aligned to the timing of a single reference T-Counter. Once a common tagger counter time has been defined, a single time-offset can be determined to align the tagger timing with the accelerator RF-time and to the other CLAS-detector subsystem times. A brief description of the calibration procedure is presented here, with the reader being referred to References [140] and [141] for further details.

The first stage of the photon tagger calibration was to convert the TDC signals from each end of the E- and T-Counters into times in ns as described above. In general, the channel-to-time conversion constant is found to be $\sim$50 ps/channel [140]. The times from the TDCs at each end of the counters are also aligned relative to each other by plotting an average of the timing difference between them

as a function of average time. The TDCs of a particular counter are calibrated when the slope of this plot is flat at a time difference of zero. This is necessary to allow event time to be independent of hit position along each counter.

Hits that do not correspond to radiating electrons must also be removed from the tagger data set. For a hit to be valid, it must be recorded by both the TDCs for each counter. In addition, the timing of hits in the E and T-Counters which correspond to a particular electron must be coincident to within 20 ns. It is possible for this latter condition to be met by two hits which cannot physically originate from the same electron. A software package based on the optics of the tagger magnet [142] has been developed to geometrically match the E and T-Counters and identify such accidental events.

The timing of each T-Counter was now aligned to a common start signal from the Level 1 Trigger, of which the tagger forms an integral part. The raw spectrum of each TDC shows a sharp peak corresponding to the trigger start signal originating in the T-Counter corresponding to that TDC, with a background to either side of the peak as a result of other TDCs providing the trigger. The value of this peak (known as the Base Peak Position) can then be subtracted from the TDC values in order to align the T-Counter values relative to the trigger start signal, thus taking into account delays in the tagger electronics. A further correction is then made in order to provide a timing alignment with a precision $\leq$1 ns in order to allow the correct beam bucket for each trigger to be identified [140].

This correction involves the alignment of each T-Counter time, $t_i$, to a reference time, $t_{REF}$, by subtraction of a calibration constant, $C_i$ [140]:

$$C_i = t_i - t_{RF} \tag{7.1}$$

The reference time was taken as the accelerator RF time, $t_{RF}$, which was measured relative to the trigger time by a PMT placed upstream of the coherent bremsstrahlung facility at the electron beam entrance to Hall B. This calibration constant will be henceforth referred to as $C_i^{RF}$. The phase difference between this periodic signal with a period of 2.004 ns and the tagger time was calculated for each counter. However, in order to determine the beam bucket corresponding to the measured RF time a timing offset, $k_e$, must also be taken into account [140]:

$$t_{RF} = t_\gamma + 2.004k_e \tag{7.2}$$

The start counter time was also taken as the reference time allowing the calibration constant, ${C_i}^{SC}$ to be calculated. The difference in the two calibration constants could was then used to calculate $k_e$ [140]:

$$C_i^{SC} - C_i^{RF} = t_\gamma - t_{SC} - 2.004k_e \tag{7.3}$$

where $t_{SC}$ is the start counter time.

The final stage of this timing calibration is then to determine the offset between the tagger time and the time determined by the other detector subsystems. This calculation was performed during the TOF calibration as all timings were aligned relative to the TOF timing and as such will be discussed in Section 7.4.

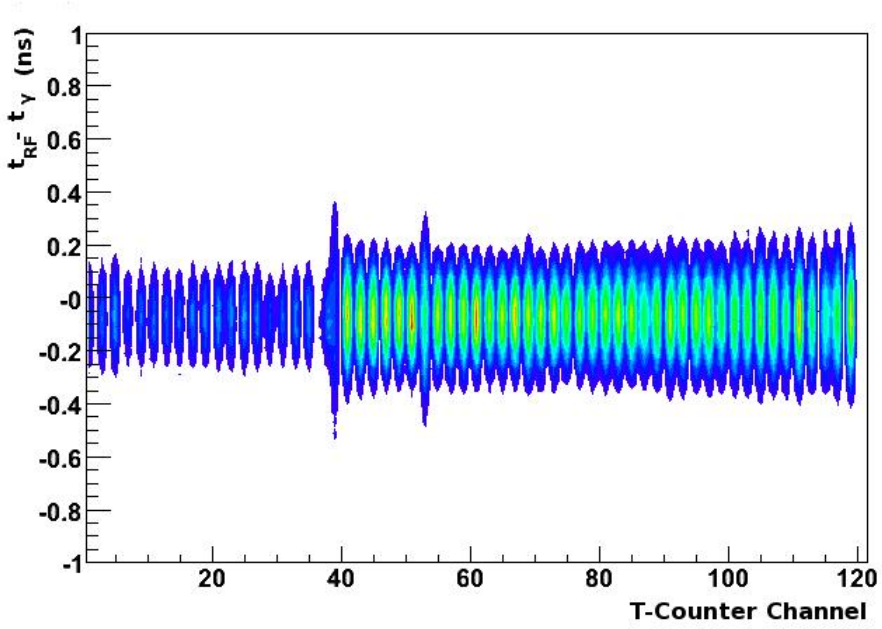


Figure 7.2: Plot of the difference in RF-corrected tagger time and tagged photon time as a function of T-Counter channel showing that all counter timings are now aligned [81].

The response of the tagger E-Counters to energy deposition was determined using a dedicated run using the pair spectrometer located downstream of the

tagger system. The energy of the $e^+e^-$ pairs produced by the pair spectrometer was measured, allowing the photon energy to be obtained. The tagged photon energy was also calculated using the radiating electron energy measured by the E-Counters and the electron beam energy. A calibration constant to correct the E-Counter energies was then defined as the ratio of these two values.

## 7.3 Start Counter Calibration

The start counter calibration involves the correction of the TDC timing signals for each paddle and provides an accurate start signal for the particle's time-of-flight calculation as well as for the determination of tagger timing offsets as described in Section 7.2. A more complete description of the start counter calibration procedure than presented here can be found in Reference [143].

The times obtained from the channel-to-time conversion of the start counter TDC signals were corrected first for the time-walk and for the time taken for a signal to travel from the hit position to the PMT located at the end of the paddle.

The time-walk correction was measured by plotting start counter time relative to the tagger time against ADC pulse height for both pion and proton events. Projections were taken along the pulse-height axis and the position of the corresponding timing peak determined. A plot of these peaks against the ADC bins could then be fit in order to obtain calibration constants to correct for the time-walk as shown in Figure 7.3.

The propagation time for the signals was calculated by plotting start counter time relative to tagger time as a function of distance along the paddle, as shown in Figure 7.4. Projections were taken along the x-axis and the peak position determined. The position of the peak in timing was then fit in order to determine the calibration constants corresponding to the propagation time.

Once the timing of each start counter paddle had been calibrated, the timing of each paddle with respect to its mirror image was adjusted so that the difference between the two times was equal to zero. The timing of each pair of start counter paddles was then aligned using the tagger as a reference time. The time difference between each event in the tagger and the corresponding event in the pairs was calculated and plot as a function of paddle number. A calibration constant was then obtained in order to align the peaks of the distribution for each pair. The

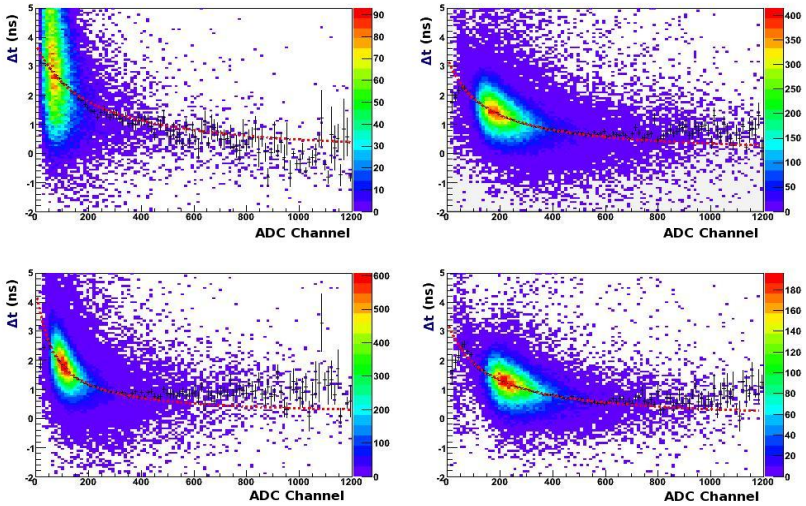


Figure 7.3: Plot of the difference in start counter and tagger time as a function of ADC channel which was fit to determine the calibration constants for the time-walk correction [81].

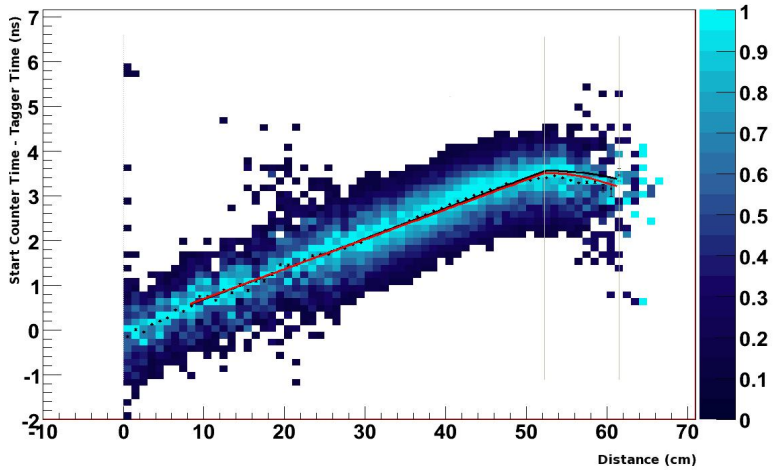


Figure 7.4: Plot of the difference in start counter and tagger time as a function of distance along the start counter for Paddle 4 of Sector 2 [81].

corrected start counter timing could now be aligned to the common time.

## 7.4 Time-of-Flight Calibration

The aim of the time of flight calibration is to enable accurate timing and energy information for each hit in the TOF. This information is central to the particle identification procedure. A more detailed description of this procedure than presented below can be found in References [100] and [138].

### 7.4.1 Timing Calibration

The first stage of the procedure is to convert the digital output of the TDC signals of the TOF system into time in ns. Data from dedicated laser runs were used to make the time-walk corrections and to align the timing obtained for signals at opposite ends of each scintillator paddle. Four nitrogen lasers which produced light with a wavelength of 337 nm [100] were used for these runs, with the light incident on the centre of each TOF paddle. The light was pulsed, with ∼4% reflected onto a photodiode circuit by a quartz plate in order to record the timing of the pulses. Signals from the TDCs during these runs were used to determine the timing offset between the PMTs at both ends of the scintillator paddle by comparing the start time recorded by the photodiode circuit and the end time when the pulse reached the TDCs. The times could then be corrected so that the signal time at both ends of the TOF paddle were aligned.

The time-walk calibration constants were calculated by plotting the difference in the TDC and diode times as a function of peak height. The peak height was obtained from the ADCs and fitting to the resulting histogram, using a similar procedure as for the start counter timing calibration (Section 7.3).

The timing of the self-consistently calibrated TOF paddles had to be aligned to the common reference time, taken as the tagger. Roughly calibrated data were used, with rough cuts made on channels containing an electron and a pion in the final state. The time difference between the electrons and pions at the event vertex was calculated using the TOF and the tagger and start counter. Constants were then calculated in order to determine the offsets between these times. In this way, the tagger, start counter and TOF subsystems were all aligned to a common time.

### 7.4.2 Energy Calibration

The aim of the energy calibration is for the energy measurement of each particle to be independent of hit position. In order to do this, the pedestal-corrected ADC peak heights are first converted into energy in MeV, and then the offset between energy measurements at each end of the scintillator paddle are calculated.

Pulse heights for pion (Minimum Ionising Particles or MIP) events at each end of the TOF scintillator paddles were obtained and converted into the geometric mean, $A_{MIP}$ which is defined as:

$$A_{MIP} = \sqrt{A_L A_R} \tag{7.4}$$

where $A_L$ and $A_R$ are the ADC peak heights from the left and right ends of the TOF paddle respectively. This also required the use of roughly calibrated data where pion events were selected using rough mass cuts. The geometric mean height was also normalised so that a MIP incident normally to the centre of the paddle would produce an ADC pulse height equivalent to 10 MeV. The peak height, $A$, was then converted to energy, $E_{ADC}$, using the relation [138]:

$$E_{ADC} = \frac{C_{ADC} A}{A_{MIP}} \tag{7.5}$$

where $C_{ADC}$ is a conversion factor.

The energies obtained at opposite ends of the TOF paddle can now be compared and an offset calculated. The ratio of energy deposition at both ends of the scintillator paddle is related to the hit position at the centre of the paddle, $x$, by:

$$\frac{ln(E_L)}{ln(E_R)} = C_\lambda - \lambda x \tag{7.6}$$

where $C_\lambda$ is an offset parameter, $E_L$ and $E_R$ are the energies measured by the left and right ADCs respectively. $x$ can be calculated using the effective velocity, $v_{eff}$, of light in the TOF scintillator material and the timings recorded by the left and right TDCs, $T_L$ and $T_R$:

$$E_{ADC} = \frac{v_{eff}(T_L - T_R)}{2} \tag{7.7}$$

$v_{eff}$ has a nominal value of 16 cmns$^{-1}$ for the CLAS TOF counters [138], but can

also be extracted by plotting the hit distance of each MIP event from the edge of the counter.

## 7.5 Drift Chamber Calibration

The drift chamber calibration aims to accurately determine the charged particle trajectories within the drift chambers. This is important as these tracks are used in conjunction with information from the Cherenkov Counters, Electromagnetic Calorimeters and TOF for particle identification. References [95] and [144] provide a more detailed description of this procedure, a brief summary being provided below.

The initial reconstruction of charged particle trajectories was performed online during the experiment and is known as "hit-based" tracking. For each sector, the charged particle hits within each superlayer and all three regions were joined using a least-squares fit. Up to 34 hits can be included in this fit, although ∼30 hits are used on average due to drift chamber inefficiencies and broken sense wires [144]. At this stage the momentum resolution of the tracks is typically ∼3-5% [95], which can be improved upon by taking into account the timing of the charged particle hits.

This second stage of drift chamber calibrations is known as "time-based" tracking and it improves momentum resolution to ∼0.5%. This stage was carried out offline once the TOF system has been calibrated. Here the drift times of the particles within the drift chambers are calculated and converted into drift distances (the distance of closest approach or DOCA) using a look-up table. The drift time is defined as the start time based on coincident signals from the tagger, start counter and TOF plus a time delay to take into account electronic delays in the electronic cables. This timing was then corrected for the channel-to-time calibration of the drift chamber TDCs, the time of flight of the particle between the reaction vertex and the hit position, the propagation time of the signal along the sense wire and also the time-walk of the signal. Fine-tuning of the correction was achieved by determining which side of the sense wire the charged particle passed. This is determined from the chi-squared values obtained from a fit to all possible tracks within a superlayer on either side of the sense wire.

## 7.6 Electromagnetic Calorimeter Calibration

Neutral particles are identified by CLAS as a hit in an Electromagnetic Calorimeter with no matching track in the drift chambers. In particular, the Electromagnetic Calorimeters are used to discriminate between photon and neutron events using their beta values[1] and as such accurate timing information is required. As the analysis presented in this thesis relies on the detection of $\pi^+$ events and the reconstruction of the neutron using the missing mass technique, this calibration was not required and is included here for completeness. The reader is referred to References [145] and [101] for further information. The Large Angle Calorimeters are calibrated in a similar way.

The EC calibrations were carried out using roughly calibrated data to identify electron and charged pion events over a wide range of energies and all angles. These particular events were chosen as the time of flight could be easily established. The charged-particle timing was first converted from TDC channel to time and corrected for the time-walk, light attenuation, signal delays, and its offset compared to a the common zero time. The time obtained for each event by the EC was then converted into the vertex time for the event in the target and compared to the vertex time obtained by the TOF subsystem. Calibration constants were then obtained in order to correct the time difference to zero.

[1]Here a neutron is defined as having, $\beta \leq 0.9$ [145].

# Chapter 8

# Data Analysis: Particle Identification and Selection of the $\pi^+ n$ Final State

This chapter will describe in detail the analysis procedure to select events belonging to the $\gamma(p,n)\pi^+$ channel from the *g9a* data set corresponding to the linearly polarised beam and longitudinally polarised target settings.

Charged particles are identified with high efficiency in the CLAS detector ($\geq$90% [82]), so the analysis relies on detecting the $\pi^+$ and reconstructing the neutron from kinematics. The $\pi^+ n$ channel was first identified by filtering the data based on the invariant mass, beta and timing of each $\pi^+$ event. The neutron was then reconstructed using the missing mass technique. Neutral particles could only be detected with a much lower efficiency ($\sim$5% for neutrons with momenta $\sim$0.6 GeV/c increasing to $\sim$50% for neutrons with momenta $\geq$2 GeV/c [82]), which would significantly reduce the event sample.

Once the channel of interest had been identified, the azimuthal ($\phi$) distribution of the $\pi^+$ in the CLAS detector was obtained, binned according to $\pi^+$ centre-of-mass energy, $W$, and the cosine of the centre-of-mass polar angle, $cos(\theta)$.

The data set analysed for this thesis was divided into subsets for each photon beam (or coherent peak) energy setting (730, 930, 1100, 1300, 1500, 1700, 1900, 2100 and 2300 MeV) and for each target setting (target polarisation parallel or anti-parallel to the beam), providing in total 18 subsets of data in the energy range 730-2300 MeV ($W$=1400-2280 MeV). At the binning stage, the data were

also further subdivided according to the specific linear photon beam polarisation setting *i.e.* whether the electric field vector of the photon beam was parallel to the floor (PARA), perpendicular to the floor (PERP) or unpolarised (AMO).

Chapter 9 will describe the next stage of analysis, in which the $G$ double-polarisation observable is extracted from the $\pi^+$ azimuthal distributions.

## 8.1 Data Reduction

The BOS files stored on the JLab tape silo contain all the data collected during JLab experiments so that they can be used for a wide range of analyses. Before the analysis of these data could begin a preliminary reduction of the *g9a* data set was carried out at JLab allowing the reduced files to be copied to the Edinburgh work disks and to also reduce the CPU time required for analysis[1].

The CLAS analysis package, ROOTBEER [146] was used for the preliminary data reduction process as well as for the subsequent analysis procedure described in this chapter. This is based on ROOT/C++ and interprets the bank structure of CLAS data. In this preliminary event selection two conditions determined the events which were retained:

1. For each event, between one and three particles must be detected in conjunction with a hit in the tagger.

2. Only three combinations of particles were allowed: one positive particle, one positive and one neutral particle, or one positive and two neutral particles.

The resulting files were then output as more compact ROOTDST (Data Summary Tape) files, the files having been typically reduced to ∼2% of their original size.

[1]Approximately 35 TBytes of data were recorded over the whole *g9a* running period.

## 8.2 The *g9a* Targets

In *g9a* experiment there were three targets simultaneously in the beamline, as shown in Figure 8.1.

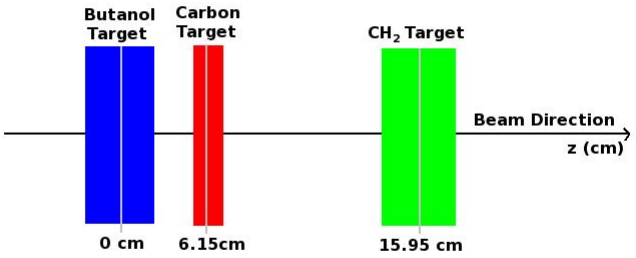


Figure 8.1: Schematic diagram of the butanol, carbon and $CH_2$ targets in the beamline (not to scale) showing the position of their centres along the $z$ axis. The butanol target was 2.67 mm thick, the carbon target was 1.49 mm thick and the $CH_2$ target was 3.45 mm thick.

The butanol ($C_4H_9OH$) target formed part of the FROST target system, as described in Chapter 6, providing polarised protons. As butanol contains unpolarised carbon and oxygen atoms as well as polarised hydrogen, analysis of events originating within the carbon target allowed assessment of this unpolarised background contribution. The $CH_2$ target provides unpolarised protons, another useful cross-check for the analysis.

Events from each of the three targets were selected by making a cut on the z-vertex position of each event to originate within one of the three targets. The z-vertex position is defined as the point of intersection of the beamline axis with the particle's trajectory extrapolated back from the drift chambers. Figure 8.2 shows the z-vertex position of all positive particle events along with the cuts made on the target positions as follows: -2.67 cm $\leq z \leq$ 2.67 cm for the butanol target, 5.0 cm $\leq z \leq$ 7.0 cm for the carbon target and 15.0 cm $\leq z \leq$ 17.0 cm for the $CH_2$ target.

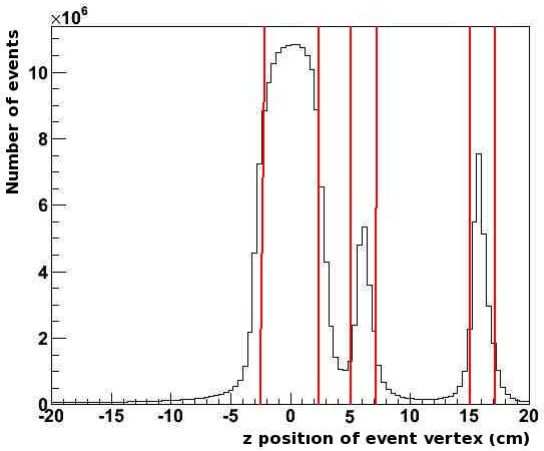


Figure 8.2: Z-vertex distribution of all positively charged particle events. The vertical red lines show the cuts made on the target positions as described in the text.

## 8.3 Initial $\pi^+$ Identification

Once events from the target of interest have been selected, the particles were identified based on their charge, $q$, momentum, $\mathbf{p}$, and beta, $\beta$. The charge of each particle is obtained from the direction of curvature of the particle's flight path as it passes through the drift chambers within the magnetic field of CLAS. The radius of curvature of this path allows the momentum of the particle to be determined:

$$\mathbf{p} = q(\mathbf{r} \times \mathbf{B}) \tag{8.1}$$

The flight time of each particle, $t_f$, is calculated based on the particle's timing in the start counter and the TOF detector. As the distance, $d$, between the hits in these detectors is known, the velocity of the particle, $v$, and hence the $\beta$ value can be obtained:

$$\beta = \frac{v}{c} = \frac{d}{ct_f} \tag{8.2}$$

where $c$ is the speed of light. These values were calculated during data reconstruction and were then used during analysis to obtain the mass-squared of each particle, $m^2$:

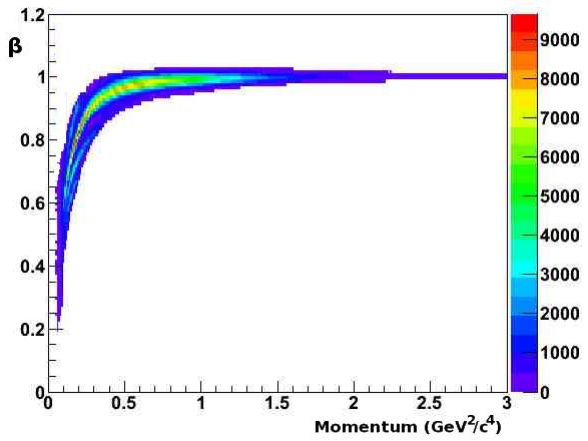


Figure 8.3: Beta as a function of momentum for the $\pi^+$ after the initial mass-squared cut.

$$m^2 = \frac{p^2(1-\beta^2)}{\beta^2} \tag{8.3}$$

and hence the energy, $E$:

$$E = \sqrt{m^2 + p^2} \tag{8.4}$$

A four-vector could then be created for each particle:

$$\mathbf{p} = [\mathbf{p}, E] \tag{8.5}$$

The first stage of channel identification was therefore to select positively charged particles, followed by a loose cut on their mass-squared values to separate $\pi^+$ from proton events. A $\pi^+$ was defined at this stage as having a mass-squared value between 0 and 0.09 GeV$^2$/c$^4$. The $\beta$ distributions of positively charged particles after this mass cut are shown in Figure 8.3. These distributions are smeared out due to background contributions from mis-identification of positively charged particles with a different mass *e.g.* $K^+$ and also from incorrect timing, showing that further filtering of the data set was still required at this stage.

## 8.4 Pion-Photon Timing in CLAS

The time at which each event took place was now compared to the timing of the photon measured by the tagger. This allowed the reduction of background and accurate knowledge of the photon energy corresponding to each event as required for the missing mass calculation.

The photons within the coherent peak were first selected using a simple cut on the photon energy range. The upper limit of this range was the coherent peak setting, the lower limit was the photon energy at which the beam polarisation dropped to 20%. The arrival time of these photons at the event vertex, $t_\gamma$, was then calculated using the tagger time, $t_{TAG}$, and the distance the photon travels from the radiator to the event vertex along the axis of the beamline, $z$:

$$t_\gamma = t_{TAG} + \frac{z}{c} \tag{8.6}$$

The $\pi^+$ time, $t_\pi$, at the event vertex was then calculated as:

$$t_\pi = t_{SC} - \frac{d}{c\beta_\pi} \tag{8.7}$$

where $t_{SC}$ is the time recorded for the event by the Start Counter, $d$ is the distance between the event vertex and the hit position in the Start Counter and $\beta_\pi$ is the beta value for the $\pi^+$ calculated using Equation 8.3, the measured value of momentum and the PDG (Particle Data Group) value of $\pi^+$ mass.

The event photon was defined as the photon whose vertex time is closest to the $\pi^+$ vertex time. Figure 8.4 shows the time difference between these event photons and the $\pi^+$ vertex time, $\Delta t$, with the majority of events having a time difference centred on zero. The smaller peaks to either side of the main peak correspond to photons from other beam buckets which were recorded during the time-window of the trigger for each event. These photons arising from neighbouring beam buckets were removed by setting the condition that $\Delta t$ must be within 1 ns. A further condition was then imposed that there should be only one photon in this timing region per event, reducing the background due to accidental photons that were recorded in the tagger within the same 1 ns timing window as the event photon, but which did not produce the event of interest detected in CLAS.

At this stage a more precise, momentum-dependent timing cut was applied to the data. Examples of plots generated for this calculation are shown in Figure

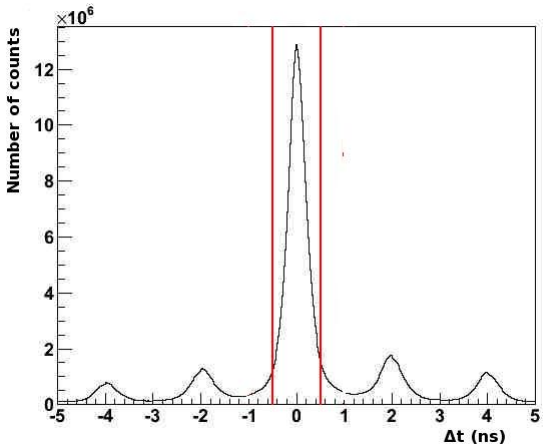


Figure 8.4: Plot showing the time difference between the event photon and the $\pi^+$ at the event vertex, $\Delta t$. The vertical red lines show the cut made to select photons which arrived at the event vertex within 1 ns of the $\pi^+$.

8.4. Figure 8.5(a) shows $\Delta t$ plot as a function of $\pi^+$ momentum. The $x$-axis of this histogram was divided into $\sim$10 MeV/c$^2$-wide bins, and the peak around $\Delta t$=0 for each projection was fit with a Gaussian function as shown in Figure 8.5(b). For bins containing at least 10 events, the width of the Gaussian, $\sigma$, was plot as a function of momentum and fit with a polynomial to determine the parameters for a cut on $\Delta t$=0 to within $\pm 3\sigma$, as shown in Figure 8.5(c). The order of polynomial was chosen based on the $\chi^2/ndf$ values of the fit, with an eighth order polynomial being chosen in general. Only bins where there were at least 10 events were included in this fit. Figure 8.5(d) shows the effect of this cut on the $\Delta t$ against $\pi^+$ momentum distribution.

Figure 8.6 shows the $\pi^+$ beta distribution at this stage of the analysis, showing a clean selection of $\pi^+$ from the original data set.

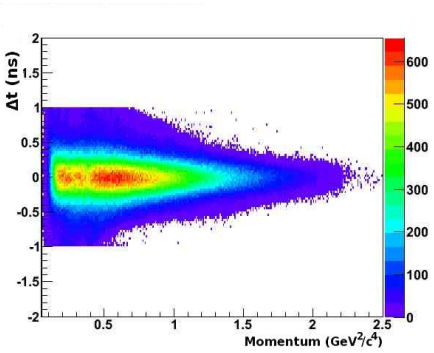


(a) $\Delta t$ plot as a function of $\pi^+$ momentum after the 1 ns timing cut.

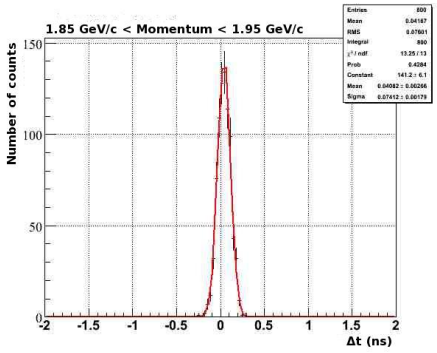


(b) Projection through the $\Delta t$ vs. $\pi^+$ momentum plot in Figure 8.5(a). The red line shows the Gaussian function fit to this projection.

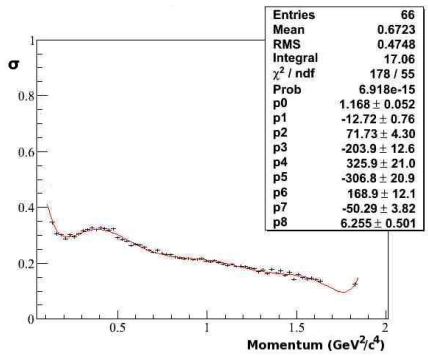


(c) Width of the Gaussian function fit to the projections obtained from Figure 8.5(a) plot as a function of momentum and fit with a eigth order polynomial.

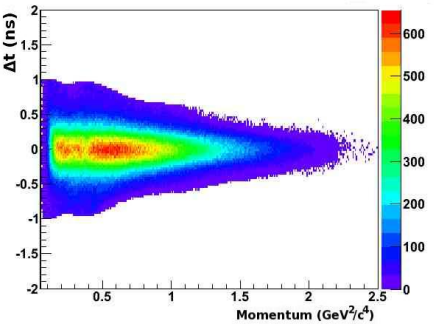


(d) $\Delta t$ plot as a function of $\pi^+$ momentum after the momentum-dependent timing cut.

Figure 8.5: Examples of plots used in the momentum dependent timing calculation described in the text.

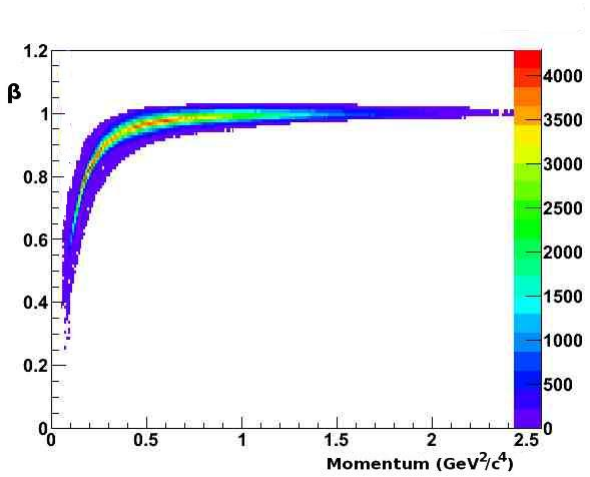


Figure 8.6: $\Delta t$ plot as a function of $\pi^+$ momentum after the momentum-dependent timing cut.

## 8.5 Fiducial Cuts

In CLAS the areas of uniform acceptance where the magnetic field is accurately mapped are known as "fiducial regions". A "fiducial cut" is the standard practice in which events detected in areas of non-uniform acceptance close to the coils of the CLAS torus magnets are removed from the analysis. In these regions the magnetic field is not well-known and the uncertainty in the trajectory and momentum of particles detected in these regions is compromised. The coils are centred at an azimuthal angle of $\phi$= $150^0$, $90^0$, $30^0$, -$30^0$, -$90^0$ and -$150^0$. A cut was made on the $\pi^+$ azimuthal angular distribution to be at least $5^0$ away from these sector angles, Figure 8.7 showing the $\pi^+$ angular distribution before and after this condition was applied.

## 8.6 Energy Loss Corrections

The four-momentum of the $\pi^+$ is determined, in part, by the three-momentum obtained from the $\pi^+$ tracks in the drift chambers. This measured momentum does not take into account the energy losses of the particles as they pass through the target cell walls, mixing chamber and holding coil as well as the start counter

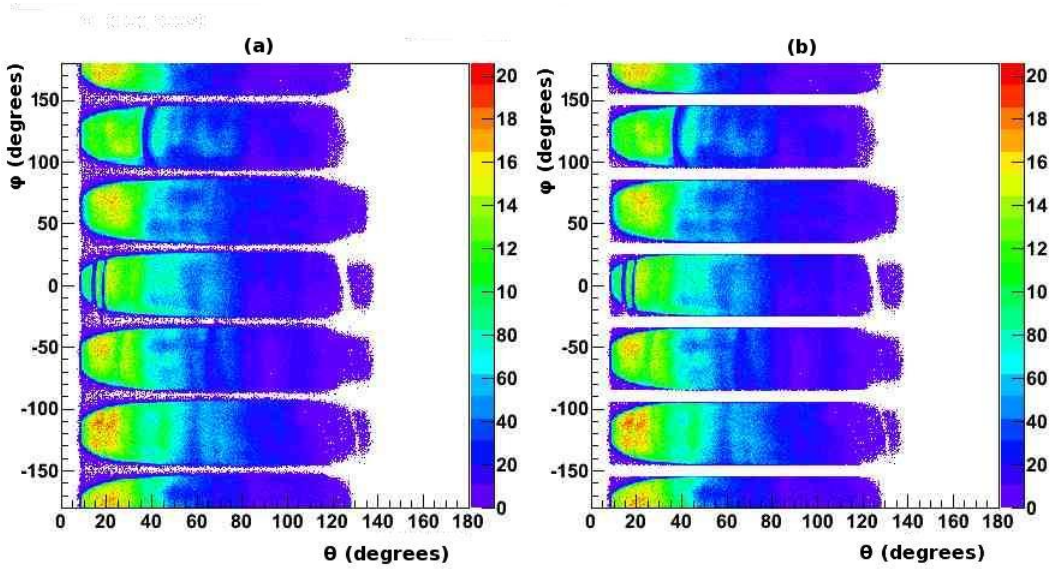


Figure 8.7: $\pi^+$ angular distribution both before (a) and after (b) the fiducial cut had been applied. Note that in (a) most events from the areas of limited acceptance around the torus coils had already been removed during the particle identification analysis procedure.

before entering the drift chambers. As a result, the momentum of the $\pi^+$ can be up to ∼0.02 GeV/c higher than that measured, as shown in Figure 8.8.

The data were corrected for this loss in momentum using the ELOSS package [147] which was updated for the *g9a*. This is the standard energy-loss correction software for CLAS experiments and can be applied to any charged particle with a mass greater than that of an electron.

The target geometry, event vertex position and particle four-momentum is input into ELOSS which then tracks back the flight path of the particle from the point at which it entered the Region 1 Drift Chambers to the event vertex. The path length of the particle in each of the materials it traverses is obtained allowing the energy lost in each material and hence the momentum lost by the particle to be calculated.

The mass and energy of the $\pi^+$ were now recalculated using the energy-loss corrected values of momentum, the PDG value of $\pi^+$ mass and the measured value of beta (Equations 8.3 and 8.4). A new energy-loss corrected four-vector was therefore created for the $\pi^+$ which was then applied in the missing mass calculation described in the next section.

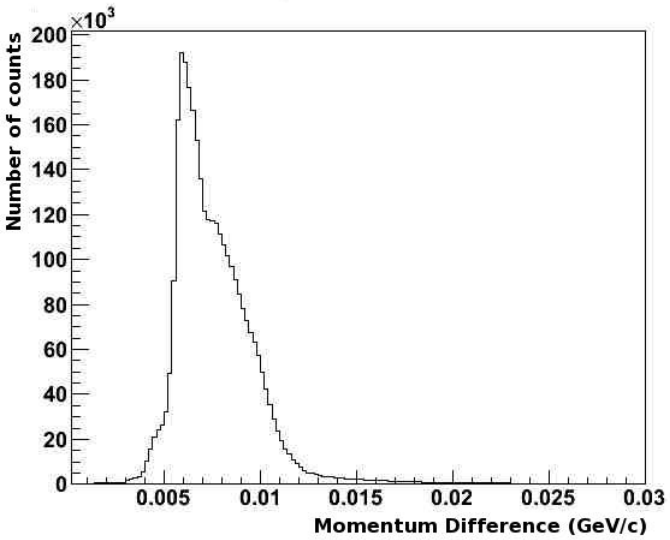


Figure 8.8: The difference in $\pi^+$ momenta measured by CLAS before and application of the ELOSS package as described in the text.

## 8.7 Reconstruction of the neutron using the missing mass technique

As the four vectors of the incident photon, target proton and outgoing pion were known, the neutron four-vector was reconstructed using the missing mass technique:

$$\gamma + p \rightarrow \pi^+ + X \tag{8.8}$$

assuming momentum is conserved in this reaction. Here $X$ can represent the neutron, other neutral particles, or combinations of positively and negatively charged particles such as $\pi^+\pi^-$. Figure 8.9 shows the missing mass distribution obtained from the reconstructed neutral four-vector, showing a sharp peak corresponding to the missing neutron mass and a broad peak to the right of this corresponding to other possible channels such as multi-pion production. This plot also shows background contributions due to photon interactions with the carbon and oxygen atoms in the butanol target.

A mass cut was performed to select the neutron and hence the $\pi^+ n$ events of interest. The width of the neutron-mass squared cut was determined by

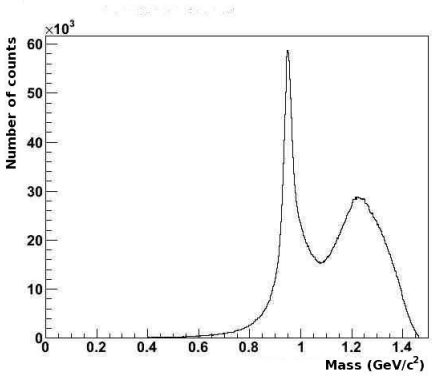


Figure 8.9: Mass distribution obtained from the reconstructed neutron four-vector, showing a sharp peak corresponding to the reconstructed neutron and a broad peak to the right of this corresponding mainly to two-pion production channels.

making a rough subtraction of the carbon and oxygen background using the missing mass distribution obtained from the carbon target data. The missing-mass squared distribution obtained from the carbon target was first scaled to the butanol missing-mass distribution. To obtain the scale factor, the butanol missing mass spectrum was divided by the carbon missing mass spectrum and fit with a Gaussian function in the region of the neutron peak and a zeroth order polynomial in the region to the left of this peak as shown in Figure 8.10.

The result of the subtraction of the carbon data from the butanol data is shown in Figure 8.11. The centroid of the peak was determined from a Gaussian fit to this distribution and a cut made on the missing mass to within three sigma of this value. It should be noted that this is the only stage of the analysis procedure in which it was necessary to physically subtract the carbon from the butanol data and that this calculation had no effect on the data set. At this stage the background underneath the neutron peak was not removed as this was not required for particle identification. A more rigorous determination of the carbon and oxygen background being performed at a later stage of analysis to calculate the dilution factor for the asymmetries as will be described in Section 9.6 of Chapter 9.

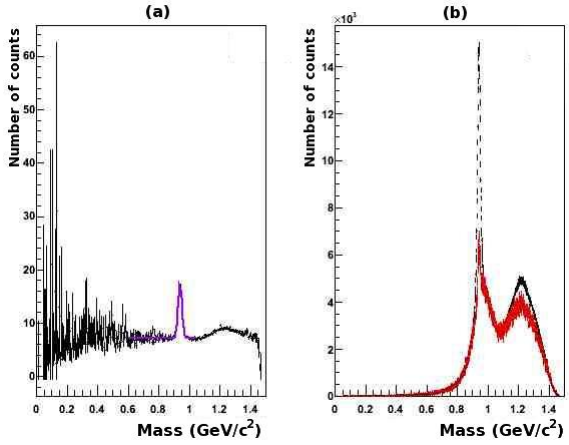


Figure 8.10: (a) Missing mass distribution obtained from the butanol target divided by the missing mass-squared distribution obtained from the carbon target. The blue line shows the fit required to obtain the scale factor as explained in the text. (b) Mass distribution obtained from the butanol target (black) overlaid with the scaled mass-squared distribution obtained from the carbon target (red).

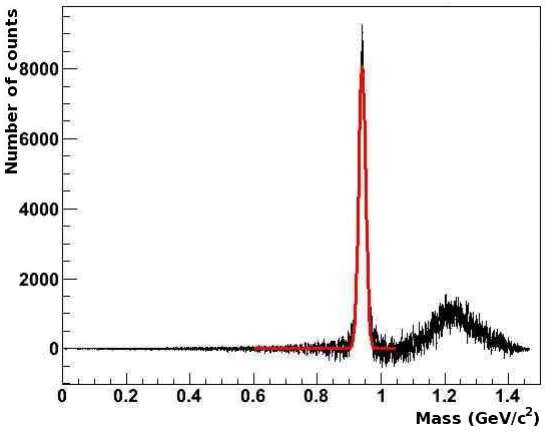


Figure 8.11: Missing mass distribution for the butanol target data with the carbon target data subtracted showing a sharp peak corresponding to the neutron mass. The red line shows a Gaussian fit to this peak used to obtain the neutron-mass cut.

## 8.8 The $\pi^+$ differential cross-section

At this stage of the analysis the $\gamma(p,n)\pi^+$ channel had been carefully selected using a combination of mass and timing cuts to the *g9a* data. The final stage of analysis was to plot the azimuthal distribution of the $\pi^+$ for each polarised photon beam and for each polarised target setting, binned in centre-of-mass energy, *W*, and the cosine of centre-of-mass angle, *cos(θ)* (Figures 8.12, 8.13 and 8.14). From these histograms, asymmetries were created between the distributions corresponding to the PARA and PERP settings from which the $G$ double-polarisation observable was extracted.

It is standard practice to create these asymmetries in the centre-of-mass (CMS) frame of reference. The invariant mass of the photon plus target proton system was obtained, allowing the $\pi^+$ four-vector to be calculated in the CMS frame using the Lorentz transformation [148]:

$$p'_x = \gamma\left(p_x - \frac{uE}{c^2}\right) \tag{8.9}$$

$$p'_y = p_y \tag{8.10}$$

$$p'_z = p_z \tag{8.11}$$

$$E = \gamma(E - up_x) \tag{8.12}$$

where $u$ is the speed of the particle in the $x$ direction and $\gamma$ is defined as:

$$\gamma = \left(\frac{1}{\sqrt{1-\beta^2}}\right) \tag{8.13}$$

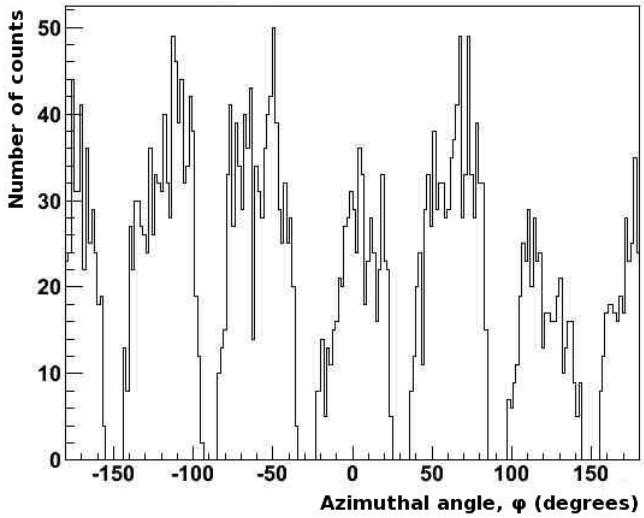


Figure 8.12: Example of a $\pi^+$ azimuthal distribution obtained for the PARA beam setting for the W=1980-2000 MeV and cos($\theta$)=0.2-0.4. Note that the holes in this distribution and in Figures 8.13 and 8.14 correspond to the areas of limited acceptance of CLAS .

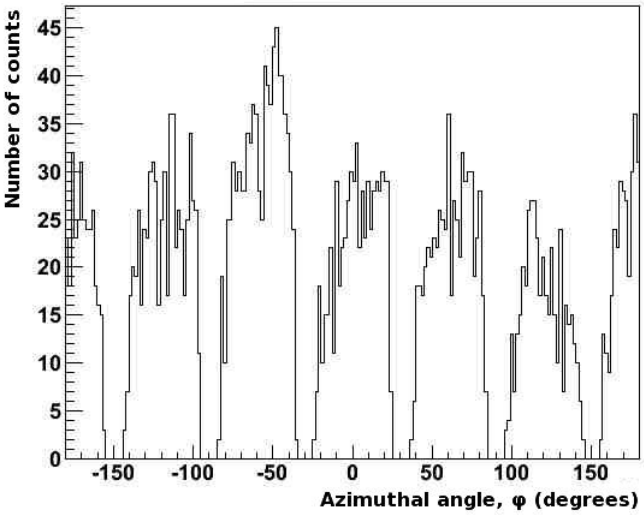


Figure 8.13: Example of a $\pi^+$ azimuthal distribution obtained for the PARA beam setting for the W=1980-2000 MeV and cos($\theta$)=0.2-0.4.

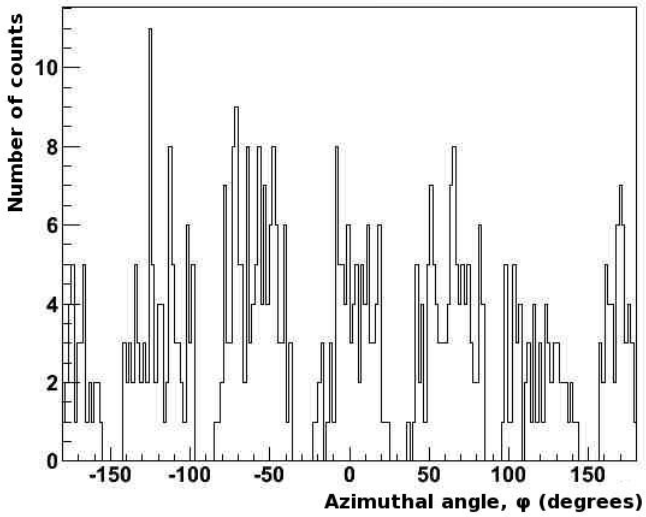


Figure 8.14: Example of a $\pi^+$ azimuthal distribution obtained for the PARA beam setting for the W= 1980-2000 MeV and $\cos(\theta)$=0.2-0.4.

# Chapter 9

# Data Analysis: Extraction of the $G$ Double-Polarisation Observable

The previous chapter described the particle identification procedure used to identify events belonging to the $\gamma(p,\pi^+)n$ channel. This chapter will describe the procedure used to extract the $G$ double-polarisation observable from the $\pi^+$ azimuthal distributions shown in Figures 8.12, 8.13 and 8.14. The results of these calculations are presented in the next chapter.

## 9.1 Introduction

When a linearly polarised photon beam is incident on a longitudinally polarised proton target, the differential cross section given by Equation 3.43 simplifies to:

$$\frac{d\sigma}{d\Omega} = \left(\frac{d\sigma}{d\Omega}\right)_{unpolarised} (1 - P_L \Sigma \cos(2\phi) + P_L P_z G \sin(2\phi)) \tag{9.1}$$

Two possible settings were used for the photon beam polarisation in the *g9a* experiment: PARA in which the electric field vector was parallel to the floor and PERP in which the electric field vector was perpendicular to the floor. In addition, the target was polarised either parallel or anti-parallel to the beam direction, defined as positive and negative target polarisation respectively. This resulted in a total of four possible combinations of polarised beam-polarised target

settings and therefore four possible descriptions of the $\pi^+$ azimuthal distributions shown in Figures 8.12, 8.13 and 8.14:

$$N_{\perp+}(\phi) = a(\phi)F_{\perp+}(1 + P_{\perp}\Sigma\cos(2(\phi-\phi_0)) - P_{+z}P_{\perp}G\sin(2(\phi-\phi_0))) \quad (9.2)$$

$$N_{||+}(\phi) = a(\phi)F_{||+}(1 - P_{||}\Sigma\cos(2(\phi-\phi_0)) + P_{+z}P_{||}G\sin(2(\phi-\phi_0))) \quad (9.3)$$

$$N_{\perp-}(\phi) = a(\phi)F_{\perp-}(1 + P_{\perp}\Sigma\cos(2(\phi-\phi_0)) + P_{-z}P_{\perp}G\sin(2(\phi-\phi_0))) \quad (9.4)$$

$$N_{||-}(\phi) = a(\phi)F_{||-}(1 - P_{||}\Sigma\cos(2(\phi-\phi_0)) - P_{-z}P_{||}G\sin(2(\phi-\phi_0))) \quad (9.5)$$

where the subscripts $||$ and $\perp$ correspond to the PARA and PERP photon beam settings respectively and the subscripts $+z$ and $-z$ correspond to the positive and negative target polarisation settings respectively. *a($\phi$)* is the acceptance of the CLAS detector, which is independent of polarisation and is therefore the same for all polarised beam-polarised target settings. $F$ is the flux on target for each beam setting, which is dependent on both energy and linear beam polarisation. $\phi_0$ is the "phi-offset" which accounts for any small mis-alignment of the diamond resulting in the beam polarisations not being exactly parallel or exactly perpendicular to the floor.

Approximately one fifth of the data were also taken using an amorphous (AMO) carbon radiator, resulting in an effectively unpolarised photon beam. In this special case, $P_L$=0 and the equations describing the $\pi^+$ azimuthal distributions become:

$$N(\phi)_{AMO} = a(\phi)F_{AMO} \quad (9.6)$$

The optimum method of removing the acceptance from the equations 9.2 to 9.5, thus allowing the extraction $G$ from the PARA and PERP data sets, is the formation of an asymmetry, *$\alpha(\phi)$*:

$$\alpha(\phi) = \frac{N(\phi)_{\perp} - N(\phi)_{||}}{N(\phi)_{\perp} + N(\phi)_{||}} \quad (9.7)$$

A parallel analysis was performed for both target polarisation settings and a weighted mean of the extracted values of $G$ obtained.

## 9.2 Choice of bin size

Ideally the data would be binned as finely as possible in centre-of-mass energy, $W$, and the cosine of the $\pi^+$ centre-of-mass angle $cos(\theta)$, limited only by the resolution of the CLAS detector. The data for each coherent peak setting were first divided into energy bins. The range of the cut placed on the coherent peak (Chapter 8 Section 8.4) was first converted into $W$ and then divided into an integer number of bins, limited by the statistics available for each coherent peak setting and by currently available beam size for the beam polarisation.

Only first stage linear photon beam polarisation tables were available at the time of writing this thesis. The ANB calculation described in Chapter 5 Section 5.12 was performed for one representative run for each coherent peak setting and for each linear beam polarisation setting, producing tables of beam polarisation as a function of beam energy. These tables were then used to produce a weighted mean of the degree of beam polarisation for accepted events in each energy bin.

This calculation contains systematic errors $\sim$10% due to changes in the position of the coherent edge and therefore the linear beam polarisation during each run[1]. These shifts are still being assessed in detail for an improved calculation with reduced systematic errors; this will become available in the near future. The current analysis uses the available polarisation tables with wider photon energy (and therefore $W$) bins. The bin widths in $W$ chosen for each coherent peak setting are summarised in Table 9.1. The current analysis can easily incorporate the updated polarisation tables when they become available.

Once the energy bin width had been determined, the $cos(\theta)$ bin width was chosen to be 0.2 for all subsets of data, based on the statistics available in each energy bin. The data set was therefore divided into a total of 340 bins, although for the coherent peak settings above 1700 MeV not all bins in $W$ were included in the final results due to limited statistics.

## 9.3 Calculation of the flux on target, $F$

During the experiment, every effort was made to collect the same amount of data for all four possible combinations of polarised beam-polarised target settings. In practice, however, the flux incident on the target for the PARA and PERP beam

[1]This systematic uncertainty is expected to be reduced to 5% by the final ANB calculation.

Table 9.1: Summary of energy bin widths in $W$ for each coherent peak setting.

| Coherent Peak Energy Setting (MeV) | Energy Range in $W$ (MeV) | Number of Energy Bins | Energy Bin Width (MeV) |
|---|---|---|---|
| 730 | 1400-1500 | 4 | 25 |
| 930 | 1480-1620 | 4 | 35 |
| 1100 | 1600-1720 | 3 | 40 |
| 1300 | 1710-1820 | 2 | 55 |
| 1500 | 1800-1920 | 3 | 40 |
| 1700 | 1800-2020 | 2 | 70 |
| 1900 | 1870-2100 | 5 | 46 |
| 2100 | 1920-2200 | 5 | 56 |
| 2300 | 1980-2280 | 6 | 50 |

settings was not equal and the $\pi^+$ azimuthal distributions had to be scaled to each other before any further analysis.

The PARA and PERP $\pi^+$ distributions for a particular target setting were first divided through by the AMO data to remove acceptance effects. Dividing equations 9.2 to 9.5 by Equation 9.6 results in the expressions:

$$N(\phi)_{||+} = \frac{F_{||}}{F_{AMO}} \left(1 + P_{||}\Sigma\cos(2(\phi-\phi_0)) - P_{||}P_{+z}G\sin(2(\phi-\phi_0))\right) \tag{9.8}$$

$$N(\phi)_{\perp+} = \frac{F_{\perp}}{F_{AMO}} \left(1 - P_{\perp}\Sigma\cos(2(\phi-\phi_0)) + P_{\perp}P_{+z}G\sin(2(\phi-\phi_0))\right) \tag{9.9}$$

$$N(\phi)_{||-} = \frac{F_{||}}{F_{AMO}} \left(1 + P_{||}\Sigma\cos(2(\phi-\phi_0)) + P_{||}P_{-z}G\sin(2(\phi-\phi_0))\right) \tag{9.10}$$

$$N(\phi)_{\perp-} = \frac{F_{\perp}}{F_{AMO}} \left(1 - P_{\perp}\Sigma\cos(2(\phi-\phi_0)) - P_{\perp}P_{-z}G\sin(2(\phi-\phi_0))\right) \tag{9.11}$$

Examples of the resulting distributions for the positively polarised target setting are shown in Figures 9.1 and 9.2. They were fit respectively with functions of the form:

$$f_{||}(\phi) = A_{||}(1 + B_{||}\cos(2\phi - C_{||}) - D_{||}\sin(2\phi - C_{||})) \tag{9.12}$$

$$f_{\perp}(\phi) = A_{\perp}(1 - B_{\perp}\cos(2\phi - C_{\perp}) + D_{\perp}\sin(2\phi - C_{\perp})) \tag{9.13}$$

where in this case $A_{||\perp}$ corresponds to the ratio of PARA (or PERP) flux on target to AMO flux on target, $B_{||\perp}$ corresponds to $P_{||\perp}\Sigma$, $C_{||\perp}$ corresponds to the phi-offset and $D_{||\perp}$ corresponds to $P_{||\perp}P_Z G$.

This method of dividing by the amorphous data rather than forming an asymmetry was necessary to allow the PARA and PERP flux to be extracted separately. In order to minimise the statistical error, this calculation was performed for each energy bin, but integrated over all polar angles. The fit was optimised by measuring $\phi_0$ and then fixing this value in the fit (Section 9.4). By extracting parameter $A_{||\perp}$ from these fits, the ratio of flux between each polarised beam setting was calculated as:

$$\frac{F_{||}}{F_{\perp}} = \frac{A_{||}}{A_{\perp}} \tag{9.14}$$

## 9.4 Measurement of the Phi-Offset

The offset in the alignment of the goniometer, $\phi_0$, was measured using the PARA and PERP $\pi^+$ azimuthal distributions obtained from the unpolarised $CH_2$ target data set. In this case $P_Z$=0 and equations 9.2 to 9.5 simplify to:

$$N_{\perp}(\phi) = a(\phi)F_{\perp}(1 + P_{\perp}\Sigma\cos(2(\phi - \phi_0))) \tag{9.15}$$

$$N_{||}(\phi) = a(\phi)F_{||}(1 - P_{||}\Sigma\cos(2(\phi - \phi_0))) \tag{9.16}$$

An asymmetry formed between these two distributions is of the form:

$$\frac{N(\phi)_{\perp} - N(\phi)_{||}}{N(\phi)_{\perp} + N(\phi)_{||}} = \frac{(1 - F_R) + \frac{2\bar{P}}{1+P_R}(1 + F_R P_R)\Sigma\cos(2(\phi - \phi_0))}{(1 + F_R) + \frac{2\bar{P}}{1+P_R}(1 - F_R P_R)\Sigma\cos(2(\phi - \phi_0))} \tag{9.17}$$

where

$$F_R = \frac{F_{||}}{F_{\perp}}$$

$$P_R = \frac{P_{||}}{P_{\perp}}$$

and

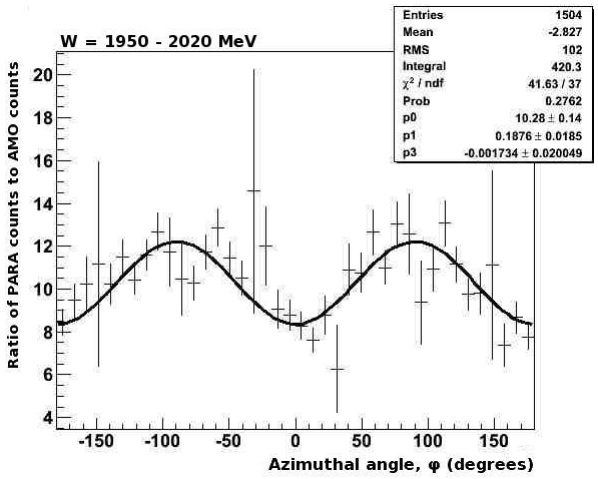


Figure 9.1: $\pi^+$ azimuthal distribution for the PARA polarised photon beam setting divided by the amorphous data set for -1.0$\leq cos(\theta) \leq$1.0. The black lines shows the fit with a function of the form of Equation 9.12

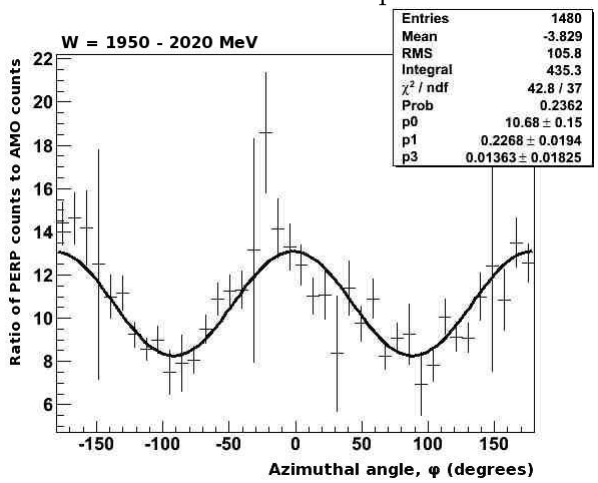


Figure 9.2: $\pi^+$ azimuthal distribution for the PERP polarised photon beam setting divided by the amorphous data set for -1.0$\leq cos(\theta) \leq$1.0. The black line shows the fit with a function of the form of Equation 9.13

$$\bar{P} = \frac{P_{||} + P_{\perp}}{2}$$

After the scaling described in the previous section, $F_R$=1, and if $P_{||}$=$P_{\perp}$=$P_L$, this equation simplifies to:

$$\frac{N(\phi)_{\perp} - N(\phi)_{||}}{N(\phi)_{\perp} + N(\phi)_{||}} = P_L \Sigma \cos(2(\phi - \phi_0))) \tag{9.18}$$

As $\phi_0$ is independent of the beam energy and the $\pi^+$ polar angle, data for all coherent peak settings summed over all polar angles were combined in order to make the most high-statistics measurement of $\phi_0$ possible. Due to the preliminary nature of the beam polarisation calculation, it was taken that $P_{||}$=$P_{\perp}$ and an average of the degree of linear polarisation for the PARA and PERP beam settings used in the fits. It was therefore possible to set $\bar{P}$ to this average value for each energy bin and $P_R$ was fixed to one.

Figure 9.3 shows the asymmetry obtained, fit with the function of the form of Equation 9.17, resulting in a value of $\phi_0$=0.2 $\pm$ 0.2$^0$.

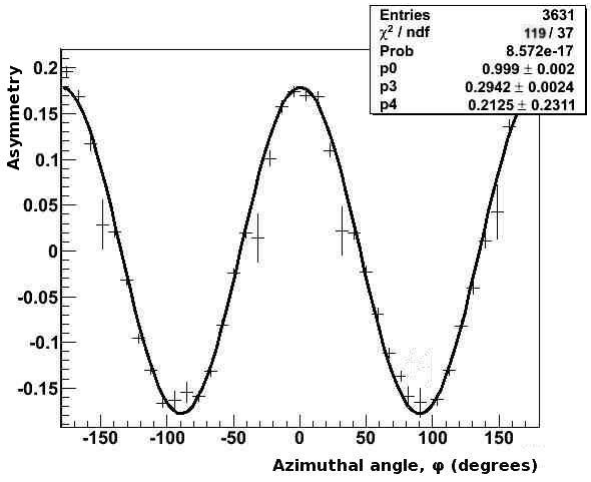


Figure 9.3: Asymmetry formed using data from the $CH_2$ target and fit with a function of the form of Equation 9.17 for 1400$\leq W \leq$2280 MeV and -1.0$\leq cos(\theta) \leq$1.0. The parameter *p4* is a measure of $\phi_0$.

## 9.5 Extraction of the $G$ Observable

Applying equation 9.7 to equations 9.2 and 9.3, the asymmetry of the PARA and PERP differential cross sections for the butanol data where the target has been positively polarised is described by:

$$\frac{N(\phi)_{\perp} - N(\phi)_{||}}{N(\phi)_{\perp} + N(\phi)_{||}} = \frac{(1 - F_R) + \frac{2\bar{P}}{1+P_R}(1 + F_R P_R)\Sigma\cos(2\phi) - \frac{2\bar{P}}{1+P_R}(1 + F_R P_R)P_z G sin(2\phi)}{(1 + F_R) + \frac{2\bar{P}}{1+P_R}(1 - F_R P_R)\Sigma\cos(2\phi) - \frac{2\bar{P}}{1+P_R}(1 - F_R P_R)P_z G sin(2\phi)} \tag{9.19}$$

This equation can also be simplified under the assumptions that the scaling has been performed correctly such that $F_R$=1, and that $P_{||}$=$P_{\perp}$=$P_L$:

$$\frac{N(\phi)_{\perp} - N(\phi)_{||}}{N(\phi)_{\perp} + N(\phi)_{||}} = P_L\Sigma\cos(2(\phi - \phi_0)) - P_L P_Z G\sin(2(\phi - \phi_0)) \tag{9.20}$$

Figures 9.4 and 9.5 show examples of asymmetries formed using the PARA and PERP $\pi^+$ azimuthal distributions obtained from both the positively polarised and negatively polarised butanol data sets. These asymmetries have been fit with the function of the form of Equation 9.19. In this fit $\bar{P}$ is fixed to the mean value of the PARA and PERP beam polarisations for the bin and $P_R$ is set to one. The value of $\phi_0$ was also fixed. $F_R$, $\Sigma$ and $P_Z G$ are left as free parameters, shown in Figures 9.4 and 9.5 as parameters $p_0$, $p_3$ and $p_5$ respectively.

Having measured $P_Z G$, the $G$ observable was now extracted by:

$$G = \frac{p_5}{P_Z} = \frac{p_5}{p_Z f} \tag{9.21}$$

where $p_z$ is the free target proton polarisation (Chapter 6 Section 6.12), an average of polarisation per run for all the runs in each data subset being used in this calculation. The $f$ term is known as the "dilution factor", required as the NMR technique calculated the polarisation of the hydrogen nuclei in the target and was not able to take into account the unpolarised carbon and oxygen nuclei present in the butanol. Quasi-free scattering from protons inside these nuclei will constitute an unpolarised background to the measured asymmetry, and hence $P_Z$=$p_Z f$ is an effective polarisation from both free and quasi-free scattering events. The calculation of the dilution factor will be described in Section 9.6.

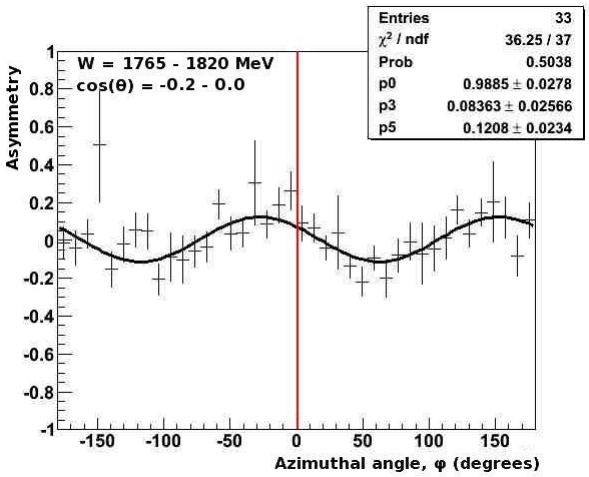


Figure 9.4: Asymmetry for the positively polarised target setting fit with a function of the form of Equation 9.19. The parameter *p5* was extracted to calculate the $G$ Observable. When compared with Figure 9.5, the vertical red line at $0^0$ is present to help demonstrate the phase shift in the asymmetry due to the target polarisation.

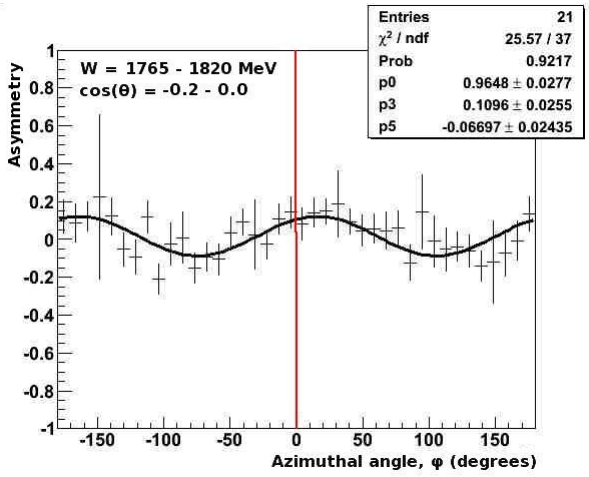


Figure 9.5: Asymmetry for the negatively polarised target setting fit with a function of the form of Equation 9.19. The parameter *p5* was extracted to calculate the $G$ Observable. When compared with Figure 9.4, the vertical red line at $0^0$ is present to help demonstrate the phase shift in the asymmetry due to the target polarisation.

## 9.6 Measurement of the Dilution Factor

The dilution factor was calculated for each energy and for each *cos(θ)* bin using data obtained from the carbon target to model the unpolarised nucleon background in the butanol target. An example of a missing-mass distribution obtained from the carbon and butanol targets is shown in Figure 9.6 below, the carbon distribution having been scaled to the butanol distribution using the method described in Chapter 8 Section 8.7.

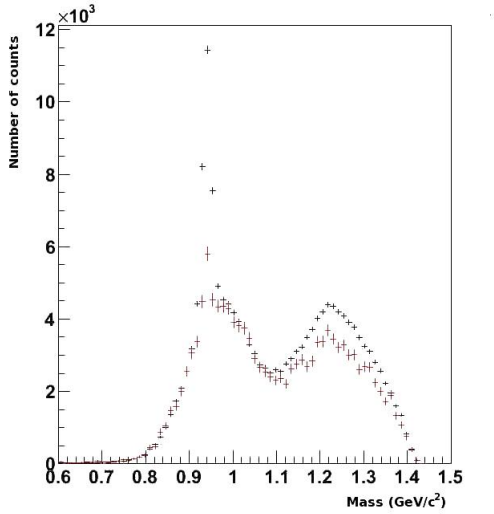


Figure 9.6: Example of a missing-mass distribution for the butanol target (black) overlaid with the scaled missing-mass distribution obtained for the carbon target (red).

### 9.6.1 Assessment of carbon background

As the carbon and butanol targets were very close together in the beamline and could not be fully resolved in the z-vertex distribution spectrum (Chapter 8, Figure 8.1), some events within the carbon z-vertex cuts will have originated from polarised protons within the butanol target.

The carbon missing-mass distribution shown in Figure 9.6 was therefore fit with a combination of two Gaussian functions and a third order polynomial in order to model its shape as shown in Figure 9.7. One Gaussian function

modelled the hydrogen "contamination", the position and width being taken from the Gaussian fit to the carbon-subtracted butanol missing-mass distribution (Chapter 8, Figure 8.11). The second Gaussian function represented the neutron peak due to the photon interaction with the carbon and oxygen nuclei. Neutron events originating from the photon interaction with a carbon or oxygen nucleus in butanol would be expected to form a peak similar in shape to the neutron peak corresponding to events from the hydrogen atom, but broadened due to the Fermi motion of the nucleons in the carbon or oxygen nucleus. The polynomial modelled the broad background coming from mostly multi-pion production and other non quasi-free processes.

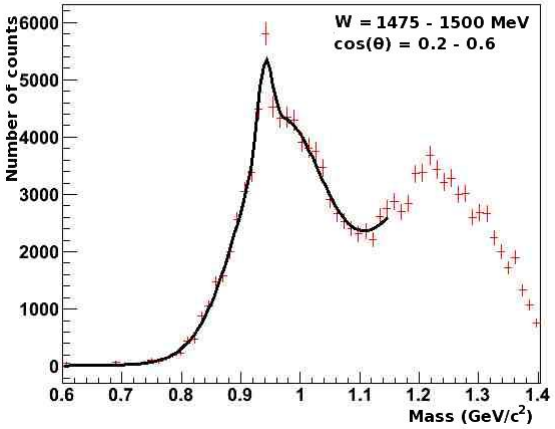


Figure 9.7: Example of a missing-mass distribution for the carbon target after scaling to the butanol missing-mass distribution. The black line shows the fit with a two Gaussian plus third order polynomial function.

Figure 9.8 shows the butanol missing-mass distribution overlaid with a function representing only the quasi-free background in butanol, and so including only the Gaussian corresponding to events on carbon nuclei and the third order polynomial function obtained from the fit in Figure 9.7.

At higher energies ($W \geq 1800$ MeV) and more backward angles ($cos(\theta) \leq 0$), it was difficult to distinguish either a free or a quasi-free neutron peak in the carbon missing-mass distributions. This effect is due to the relatively small single-pion production cross-section in this kinematical region compared to multi-pion production. An example of such a distribution is shown in Figure 9.9. In these cases, it was found that a simple third order polynomial fit was more appropriate.

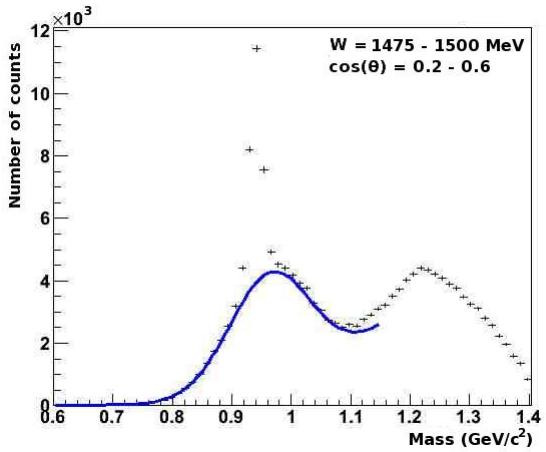


Figure 9.8: Example of a missing-mass distribution for the butanol target overlaid with a Gaussian plus third order polynomial function representing the carbon contribution to the butanol data in blue. This function is obtained from the fit to Figure 9.7.

The choice of fit to the carbon missing-mass distributions was determined by comparing the $\chi^2$ per degree of freedom obtained from the two Gaussian plus third order polynomial fit and the simple third order polynomial fit.

Figure 9.10 shows a butanol missing-mass distribution overlaid with the function obtained with the third order polynomial fit in Figure 9.9.

### 9.6.2 Calculation of the Dilution Factor, *f*

The integral of the butanol spectrum and the carbon function within the neutron mass cuts defined in Chapter 8 Section 8.7 were then obtained, allowing the dilution factor to be calculated as:

$$f = \frac{N_B - N_c}{N_B} \tag{9.22}$$

where $N_B$ is the integral of the butanol spectrum within the neutron-mass cuts and $N_C$ is the integral of the carbon function within the neutron missing-mass cuts. In order to maximise the statistics available to obtain each data point, it was decided to measure the dilution factor for all $W$ bins, but with the data divided into five *cos(θ)* bins. Graphs of $f$ as a function of *cos(θ)* for each energy bin were fit with a first order polynomial from which the dilution factor for each

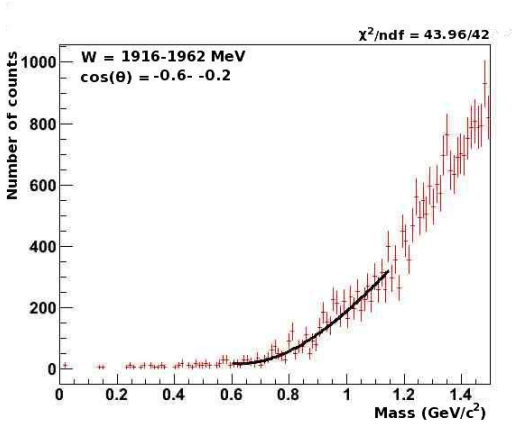


Figure 9.9: Example of a missing-mass distribution for the carbon target after scaling to the butanol missing-mass distribution. The black line shows the fit with a third order polynomial function.

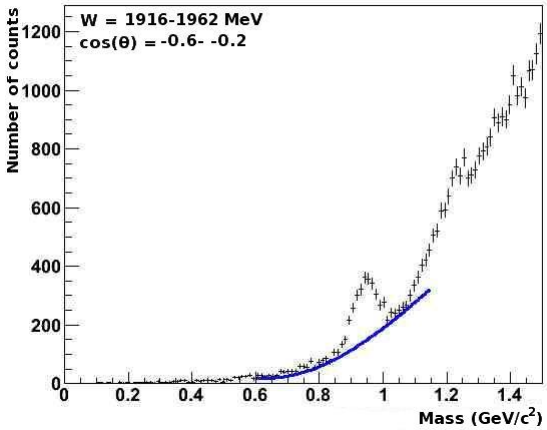


Figure 9.10: Example of a missing-mass distribution for the butanol target overlaid with a third order polynomial representing the carbon contribution to the butanol data in blue. This function is obtained from the fit to Figure 9.9.

*cos(θ)* bin could be extracted. Examples of these graphs are shown along with their fit functions in Figures 9.11.

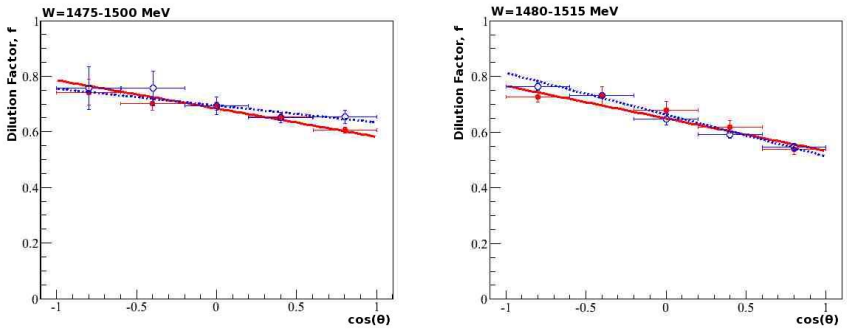


Figure 9.11: The dilution factor, *f*, plot for two different centre-of-mass energies, *W*. The solid-red circles represent data taken from the positively polarised target setting whose fit function is shown as the solid-red line. The hollow-blue circles represent data taken from the negatively polarised target setting whose fit function is shown as the dashed-blue line. The errors shown are statistical errors.

In a similar way, the proportion of hydrogen events originating within the carbon z-vertex cuts was estimated as:

$$f_C = \frac{N_{CT} - N_C}{N_{CT}} \tag{9.23}$$

where $N_{CT}$ is the integral of the scaled carbon spectrum within the neutron-mass cuts and $N_C$ is the integral of the carbon Gaussian plus third order polynomial function within the neutron missing-mass cuts as before. Figure 9.12 shows the range of values obtained in the calculation of $f_c$.

## 9.7 Uncertainties in the measurement of *G*

This section will describe the uncertainties in the extraction of the $G$ double-polarisation observable detailed above.

### 9.7.1 Statistical Uncertainties

The sources of statistical uncertainty in the value of the $G$ double-polarisation observable are listed below:

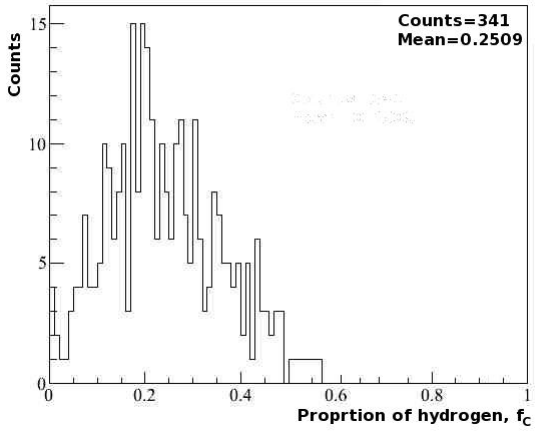


Figure 9.12: Histogram showing the range of values obtained in the calculation of the proportion of polarised protons contaminating the carbon target.

1. The statistical error for each value of the the dilution factor calculated from the missing-mass distributions, and shown as the points in Figures 9.11 for example, is calculated as follows:

$$\delta f^2 = \left(\frac{N_C}{N_B^2}\right)^2 \delta N_B^2 + \left(\frac{-1}{N_B}\right)^2 \delta N_C^2 \tag{9.24}$$

   where $\delta f$ is the statistical error in the dilution factor, $\delta N_B$ is the error in the integral of the butanol missing-mass distribution, and $\delta N_C$ is the error in the integral of the carbon function. The error in the values of dilution factor extracted from the fits to these figures is then calculated as the addition in quadrature of the errors of the two parameters describing the fit functions.

2. The fractional error in the fit parameter from which the $G$ observable is obtained.

3. The statistical error in the target polarisation, the calculation of which is described in Chapter 6 Section 6.16.

These were then combined by adding the three fractional errors in quadrature, the statistical error being dominated by the asymmetry fit parameter. The final values of the $G$ observable shown in Chapter 10 are plot with this prescription for calculating the statistical errors.

### 9.7.2 Systematic Uncertainties

The first stage in assessing the systematic uncertainties of this experiment involved verifying the analysis procedure described above through the goodness of fit to the asymmetries.

#### Goodness of fit

The chi-squared per degree of freedom of the fits to the butanol data provides a good indication of the quality of the fits used to obtain the $G$ observable. As can be seen from Figure 9.13, their distribution is peaked close to a value of one, showing that the fits to each asymmetry were good overall.

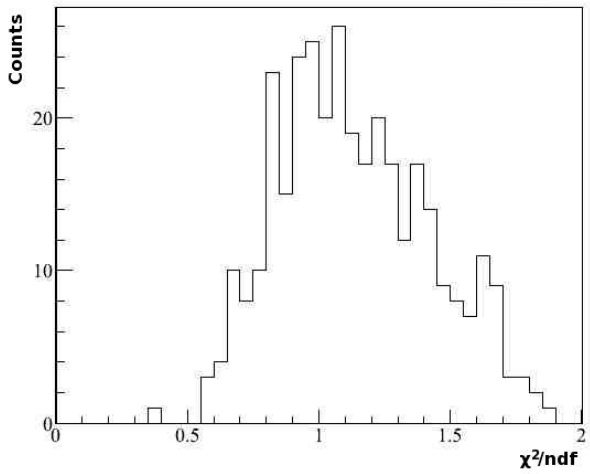


Figure 9.13: Distribution of the chi-squared per degree of freedom for all fits to the butanol asymmetries.

**Comparison of the $G$ Observable for both target settings** Appendix A compares the values of the $G$ observable obtained using both target settings plot as a function of $W$ and for all ten $cos(\theta)$ bins. It was seen that the the values of this observable obtained for each target setting were consistent with each other within errors, as would be expected if the difference in running conditions for the positive and negative target settings do not systematically effect the final results. These differences were therefore well-accounted for by the calculated values of target polarisation.

**Comparison of the Σ Observable for both target settings** Referring to equation 9.19, the single-polarisation observable Σ could also be extracted from the fit to the butanol asymmetry. If data from the unpolarised $CH_2$ target are analysed using the same procedure as for the butanol target data, Σ can also be extracted. An example of an asymmetry from the $CH_2$ target is shown in Figure 9.14, fit with the function of the form of Equation 9.17, the parameter *p3* corresponding to the Σ observable.

Appendix B shows values of the Σ observable plot as a function of $W$ for both the $CH_2$ and butanol targets. The values obtained for both targets are consistent.

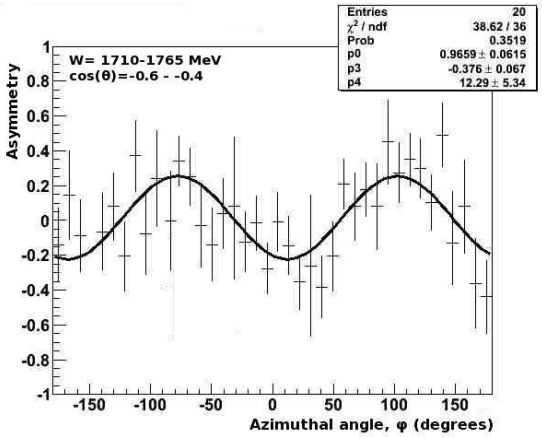


Figure 9.14: Example of an asymmetry obtained for the $CH_2$ target, fit with a function of the form of Equation 9.17. The Σ observable was extracted as parameter *p3* from this fit.

### Calculation of systematic uncertainties

The effect of the most dominant systematic uncertainties on the values of $G$ is quantified in the following sections. These dominantly arise from the following calculations: the dilution factor, the beam polarisation, the target polarisation and the phi-offset. A brief description of the assessment of each source of systematic error is given below, with the exception of the target polarisation which can be found in Chapter 6 Section 6.16.

The uncertainties are quoted as percentage errors, calculated for every value of $G$ as:

$$\sigma_Q = \frac{Q_0 - Q_1}{Q_0} \times 100 \tag{9.25}$$

where $Q_0$ is the actual parameter used in the extraction of $G$ and $Q_1$ is a recalculated value of this parameter. In the sections which follow, the percentage errors are histogrammed in order to show their effect on $G$ *i.e.* whether the magnitude of the observable will increase or decrease. They are also quoted as an average magnitude for each coherent peak setting, calculated as:

$$\bar{\sigma_Q} = \frac{\sum_{N=0}^{N} \mid \sigma_Q \mid}{N} \tag{9.26}$$

where $|\sigma_Q|$ is the magnitude of the percentage error for the value of $G$ and $N$ is the number of values of $G$ in for the four combinations of polarised beam-polarised target.

**Determination of the systematic error in $G$ due to the dilution factor**
The systematic uncertainty in the dilution factor arose from the calculation of the scale factor and the fits to the scaled carbon missing-mass spectra, each contribution being assessed separately.

Referring to Chapter 8 Section 8.7 the scale factor was calculated by fitting a Gaussian plus a zeroth order polynomial function to the butanol missing mass spectrum divided by the carbon missing mass spectrum (Figure 8.7). The range of this fit was determined by the mass region in which there were sufficient statistics *ie.* where there were at least 10 events in each 12 MeV/c$^2$ bin, and was typically between 0.7 and 1.1 MeV/c$^2$. The sensitivity of the dilution factor to the fit range of the scale factor was checked by refitting the range reduced by 50 MeV. The variation on the calculated dilution factor was expressed as a percentage difference and is plot as a histogram in Figure 9.15.

The fit range to the scaled carbon missing-mass distribution was typically between 0.7 and 1.15 MeV/c$^2$, chosen in the same manner as the range for the scale factor fit. As for the scale factor, the sensitivity of the dilution factor to the fit range of the scale factor was checked by refitting the range, in this case by $\pm$50 MeV. The resulting percentage difference between the original and refitted dilution factors is histogrammed in Figure 9.16.

The dominant source of uncertainty in the calculation of the dilution factor arises from the choice of fit function to the scaled carbon missing mass spectra. In order to place a limit on this uncertainty, the dilution factor was recalculated using

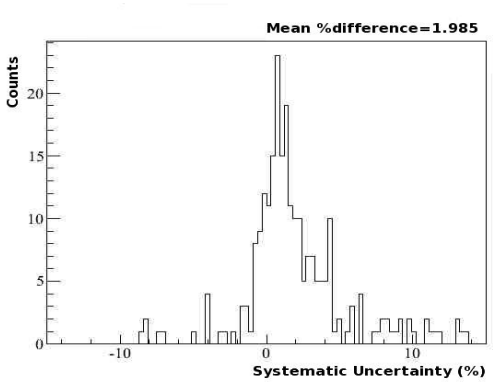


Figure 9.15: Histogram demonstrating the uncertainty due to the fit range chosen for the scale factor. The percentage differences in the dilution factor were obtained by reducing the fit range of the scale factor by 50 MeV.

only the integral of the butanol missing-mass distribution within the neutron mass cuts and the integral of the carbon distribution within the neutron mass cuts. The carbon distribution was corrected for the hydrogen contamination using the values calculated using Equation 9.23. Again, the recalculated and original values of $f$ were compared, the range of the resulting percentage error being shown in Figure 9.17.

**Determination of the systematic error in $G$ due to the beam polarisation** The systematic error in the beam polarisation due to the ANB calculation (Chapter 5 Section 5.12) was estimated to be 10% [149]. This is expected to have a significant effect on the value of the $G$ observable obtained from the fits to the asymmetries, as the two parameters involving the beam polarisation are fixed in the fits.

Referring to Section 9.5, the ratio of $P_{||}$ to $P_{\perp}$, $P_R$ is fixed to one, assuming that the beam polarisation for each setting must be equal. To assess the contribution of this assumption to the systematic error, $P_R$ was fixed in the fits to the asymmetries as its maximum and minimum possible values, $P_{RMAX}$ and $P_{RMIN}$ respectively:

$$P_{RMAX} = \frac{P_{||} + 0.1P_{||}}{P_{\perp} - 0.1P_{\perp}} \tag{9.27}$$

$$P_{RMIN} = \frac{P_{||} - 0.1P_{||}}{P_{\perp} + 0.1P_{\perp}} \tag{9.28}$$

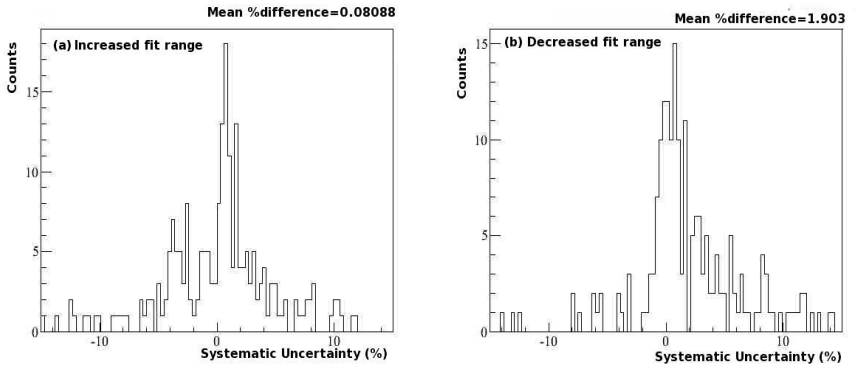


Figure 9.16: Histogram demonstrating the uncertainty due to the fit range chosen for the fit to the carbon histogram. The percentage differences in the dilution factor were obtained by (a) increasing the fit range of the scale factor by 50 MeV and (b) decreasing the fit range of the scale factor by 50 MeV.

By comparing the values of $G$ obtained by fixing the ratio of beam polarisations to its extreme values. The percentage difference in the measured and recalculated values of $G$ for both cases were calculated in the same manner as for the dilution factor and are histogrammed in Figure 9.18.

A more dominant source of systematic error due to the beam polarisation arose from the parameter in which the mean value of beam polarisation is fixed in the fit to the asymmetries. New values of $G$ were calculated where this mean polarisation was fixed to its maximum and minimum possible values, $\bar{P}_{MAX}$ and $\bar{P}_{MIN}$ respectively:

$$\bar{P}_{MAX} = \frac{(P_{||} + 0.1P_{||}) + (P_{\perp} + 0.1P_{\perp})}{2} \tag{9.29}$$

$$\bar{P}_{MIN} = \frac{(P_{||} - 0.1P_{||}) + (P_{\perp} - 0.1P_{\perp})}{2} \tag{9.30}$$

This resulted in an average systematic error in the value of $G$ of $\sim$10% as would be expected.

**Determination of the systematic error in $G$ due to $\phi_0$** A further parameter fixed in the fit to the asymmetries was $\phi_0$, which was calculated to be $0.2 \pm 0.2^0$. Fits to the asymmetries were therefore performed with $\phi_0$ set to its maximum and minimum values of $0.4^0$ and $0^0$ respectively. Figure 9.19 shows

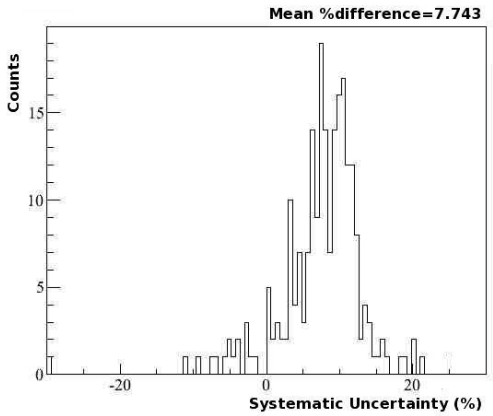


Figure 9.17: Distribution of the percentage difference in the values of dilution factor obtained by integrating the carbon function and by integrating the carbon histogram within the neutron mass cuts.

the percentage difference between the values of $G$ calculated using the measured value of $\phi_0$ and its extreme values. It can be seen from these histograms that the dominant uncertainty was that obtained from the upper value of $\phi_0$.

**Summary of systematic errors** Table 9.2 summarises the average systematic percentage errors calculated for each coherent peak and polarised target setting. For each parameter, the systematic error was calculated using Equation 9.26 for every bin. For simplicity, the values quoted in the tables are the average of the systematic uncertainty for each value of $G$ for all four combinations of polarised beam-polarised target settings. Where more than one uncertainty was calculated for a parameter, these were added in quadrature before the average was calculated.

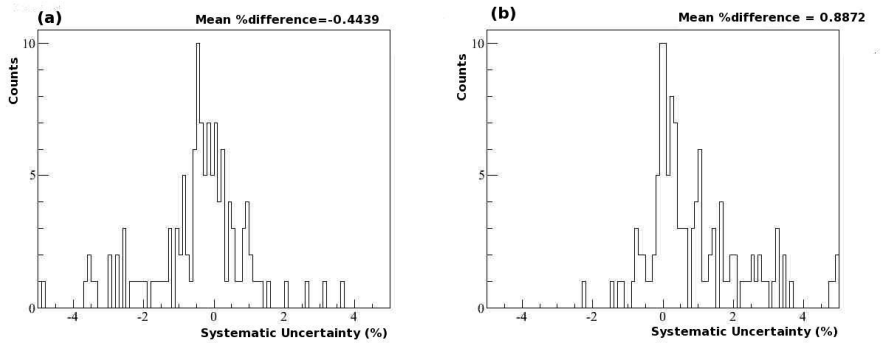


Figure 9.18: Histogram demonstrating the uncertainty in $G$ due to the ratio of PARA and PERP beam polarisations, $P_R$. The percentage differences in $G$ were obtained by (a) fixing $P_R$ to its minimum possible value and (b) fixing $P_R$ to its maximum possible value.

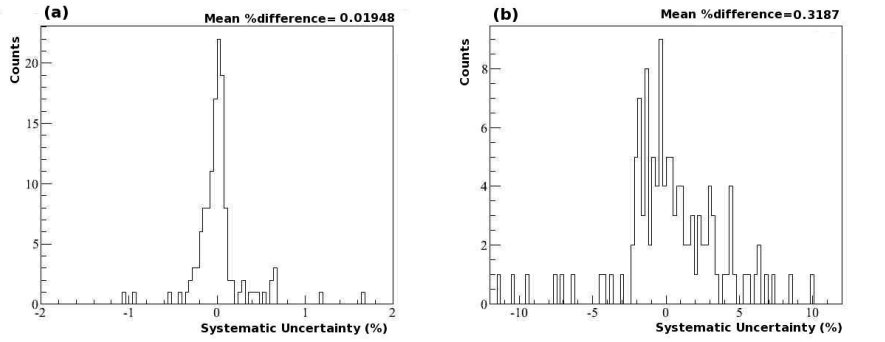


Figure 9.19: Histogram demonstrating the uncertainty in $G$ due to fixing $\phi_0$ in the fit to the butanol asymmetries. The percentage differences in $G$ were obtained by (a) fixing $\phi_0$ to its minimum possible value and (b) fixing $\phi_0$ to its maximum possible value.

Table 9.2: Summary of the systematic uncertainties in the value of the $G$ observable measured in this experiment.

| Coherent Peak Energy Setting (MeV) | % uncertainty due to $f$ | % uncertainty due to $P_L$ | % uncertainty due to $\phi_0$ | % uncertainty due to $p_Z$ |
|---|---|---|---|---|
| 730 | 14 | 10 | 3 | 2 |
| 930 | 12 | 10 | 2 | 2 |
| 1100 | 12 | 10 | 2 | 2 |
| 1300 | 9 | 10 | 5 | 2 |
| 1500 | 13 | 10 | 1 | 2 |
| 1700 | 11 | 10 | 7 | 2 |
| 1900 | 10 | 12 | 5 | 2 |
| 2100 | 11 | 10 | 9 | 2 |
| 2300 | 15 | 10 | 4 | 2 |

# Chapter 10

# Results and Discussion

This chapter will present the values of the $G$ double-polarisation observable extracted from the *g9a* data set for the $\gamma(p,\pi^+)n$ reaction using the methodology described in Chapters 8 and 9. These results are presented both as a function of centre-of-mass energy, $W$, for all ten $cos(\theta)$ bins and as a function of $cos(\theta)$ for the 26 $W$ bins containing sufficent statistics for a precise measurement of $G$. Each value of $G$ is plotted with statistical errors only, the reader being referred to Chapter 9 Section 9.7.2 for further details of the associated systematic errors. This chapter also compares these results to the current SAID [44], MAID2007 [43] and Bonn-Gatchina BG2010-02 [48] PWA solutions (shown on the figures as solid-red, dashed-blue and dot-dashed black lines respectively) and to the previous experimental data in the 730 to 2300 MeV photon energy region [71] (shown as pink squares).

## 10.1 G as a function of energy

Figures 10.1 to 10.3 show the results for the extraction of the $G$ observable plot as a function of $W$ in 10 bins of $cos(\theta)$ from -1.0 to 1.0. The new data clearly represent a very significant improvement in the quality of measurement and kinematic coverage compared to the current world data set for most of the $cos(\theta)$ bins. The new data are in limited agreement with the one previous measurement of $G$ in this region measured by Bussey *et al.*, within the relatively poor statistical accuracy of these previous data. However, $cos(\theta)$ bins -0.2 to 0.0 and 0.6 to 0.8 indicate a systematic drift between the new and previous data sets.

Broad general agreement is obtained at lower energies ($W \leq 1800$ MeV) between the new data measured for this thesis and at least one of the three partial wave analyses. In particular, Figure 10.1 shows that for $-1.0 \leq cos(\theta) \leq -0.8$, $-0.8 \leq cos(\theta) \leq -0.6$, the Bonn-Gatchina solution appears to be favoured by the data and for $-0.6 \leq cos(\theta) \leq -0.4$, the SAID solution tends to be favoured between 1600 and 1800 MeV. For the most forward angle bins shown in Figure 10.3, the solutions of the three partial wave analyses are similar in this low energy region and their current solutions are confirmed by the new data points.

Above 1800 MeV, the three PWA solutions strongly diverge as the experimental data set in this region is increasingly sparse resulting in unconstrained PWA fits to this region. For example, for the $-0.4 \leq cos(\theta) \leq -0.2$ bin, the expectations for $G$ from current PWA solutions span almost the entire range of the $G$ observable. For $W \geq 1800$ MeV, none of the PWA solutions provide a good description of the new data and clearly the PWA need to be refitted including the new data set. The data exhibit interesting and unexpected structure as a function of $W$. In particular, the large peak at $W \approx 2100$ MeV in the $-0.6 \leq cos(\theta) \leq -0.4$ bin (Figure 10.1) is not at all expected by the PWA solutions within this angular range. However, until these data are finalised and included in new partial wave analysis fits to the world data set, it is difficult to draw any firm conclusions as to the significance of this observation.

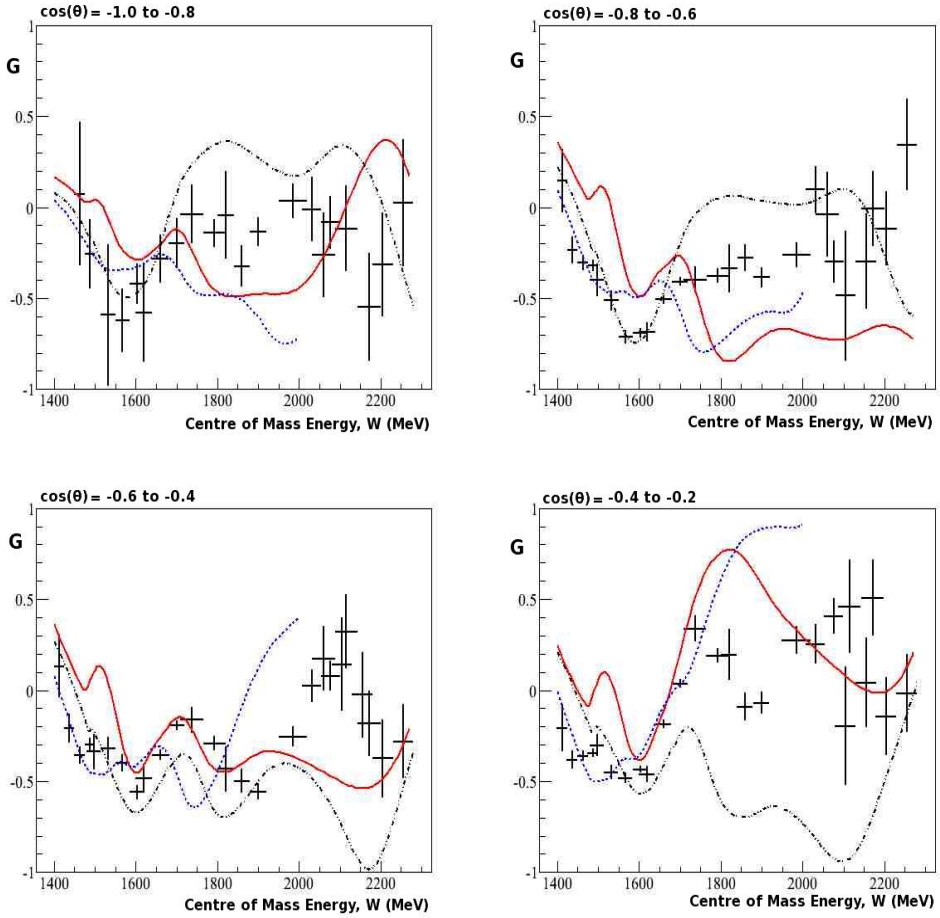


Figure 10.1: New values of the $G$ double-polarisation observable calculated for this thesis (black points) plot as a function of $W$. Overlaid on the plots are the current SAID [44] (solid-red line), MAID2007 [44] (dashed-blue line) and Bonn-Gatchina BG2010-02 [48] (dot-dashed black line) PWA solutions, where the new data have not yet been included in the fits.

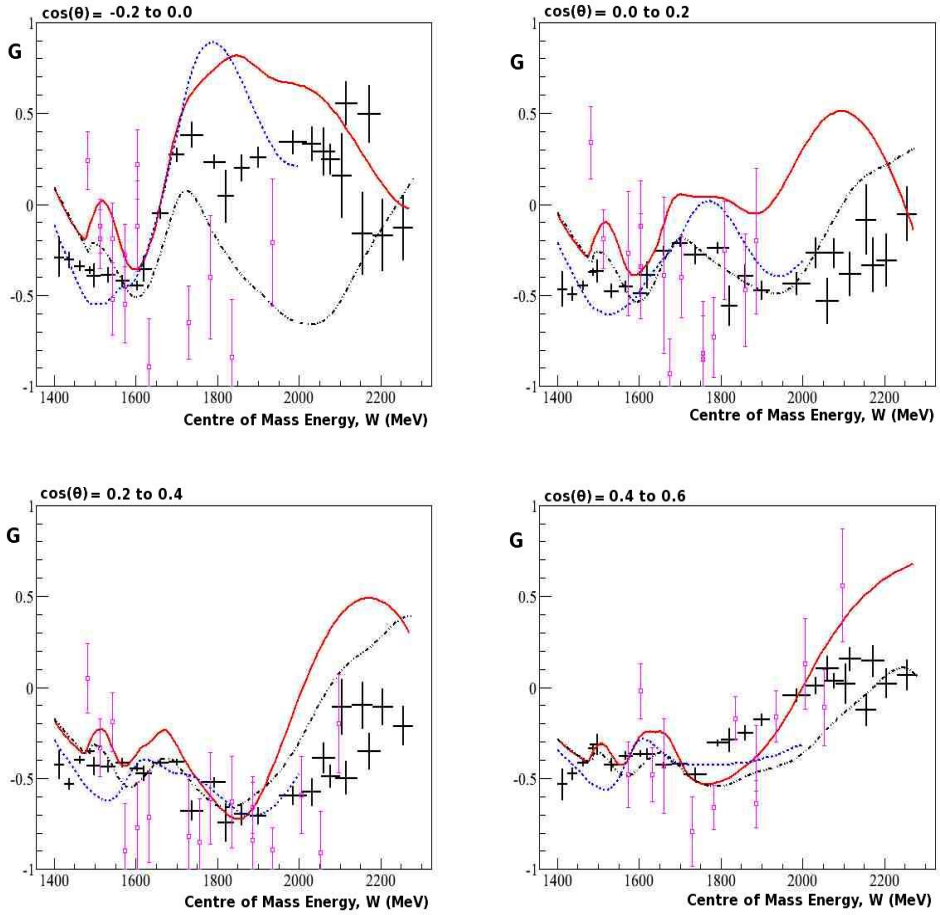


Figure 10.2: New values of the $G$ double-polarisation observable calculated for this thesis (black points) plot as a function of $W$. Overlaid on the plots are the current SAID [44] (solid-red line), MAID2007 [44] (dashed-blue line) and Bonn-Gatchina BG2010-02 [48] (dot-dashed black line) PWA solutions, where the new data have not yet been included in the fits. The open pink squares show the previous experimental data for the $G$ observable [71].

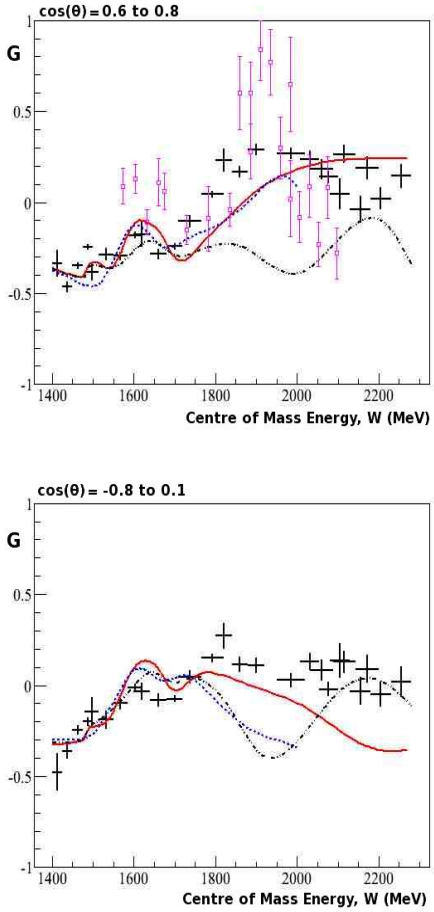


Figure 10.3: New values of the $G$ double-polarisation observable calculated for this thesis (black points) plot as a function of $W$. Overlaid on the plots are the current SAID [44] (solid-red line), MAID2007 [44] (dashed-blue line) and Bonn-Gatchina BG2010-02 [48] (dot-dashed black line) PWA solutions, where the new data have not yet been included in the fits. The open pink squares show the previous experimental data for the $G$ observable [71].

## 10.2 G as a function of *cos(θ)*

Figures 10.4 to 10.10 show the $G$ observable plot as a function of *cos(θ)* in 26 bins of $W$.

As was seen in Figures 10.1 to 10.3, better general agreement with at least one of the PWA solutions is obtained below $W \approx 1800$ MeV, with the level of agreement deteriorating above this energy. The angular dependence of $G$ also appears to be in some limited agreement with the sparse previous data of Bussey *et al.* for many $W$ bins. However, there are some suggestions of a different shape in the distributions for more forward angles in the $1475 \leq W \leq 1500$ MeV and $1480 \leq W \leq 1515$ MeV bins where the previous data exhibits positive $G$ values while the new data are strongly negative.

Figures 10.4 to 10.10 also allow the results of each of the three leading PWA solutions to be compared more easily on an individual basis with the new data. The new data clearly favour overall the MAID solution at lower energies ($W \leq 1475$ MeV). This is a particularly important result lying in a mass region where there are relatively fewer contributing resonances, and which is also the region of the poorly-established $P_{11}(1440)$ Roper resonance. However, for the region $1475 \leq W \leq 1550$ MeV the new data appear to be best described by the Bonn-Gatchina solution. This is also the case for the region $1550 \leq W \leq 1620$ MeV where *cos(θ)*$\leq$-0.4.

The previous Bussey *et al.* data have shown large and somewhat puzzling discrepancies with all modern PWA analyses for the $1475 \leq W \leq 1515$ MeV and $1585 \leq W \leq 1620$ MeV energy regions; here the new data tend to lie within the region expected by the partial wave analyses. Although not conclusive, the magnitude and sign of the new data in this region and the inability of the PWA to describe the previous data may indicate some systematic uncertainties in this part of the Bussey *et al.* data set. As discussed in Chapter 4, the extraction of $G$ from the earlier data was complicated significantly by the orientation of the target polarisation.

At higher energies ($W \geq 1600$ MeV) the partial wave analyses exhibit oscillations in the angular distribution of $G$, the features of which are broadly evident in the new data. The magnitudes of these oscillations are in broad agreement with MAID and SAID, although the data suggest their size is smaller than the current PWA expectations. The Bonn-Gatchina model significantly underestimates the

magnitude of the central maxima and gives a poor description of the phase of the oscillations in the data.

Significant discrepancies between the new data and the PWA solutions arise, where $1950 \leq W \leq 2088$ MeV. In this region neither the SAID nor the Bonn-Gatchina predictions are favoured by the new data and the MAID solution is no longer valid as MAID does not include resonances above 2000 MeV (Chapter 3 Section 3.6.1). The new data continue to show similar angular dependencies as for the $1600 \leq W \leq 1950$ MeV region. However, the PWA solutions predict different angular dependencies. The Bonn-Gatchina model in particular gives poor agreement in this region predicting $G$ to be larger and of opposite sign to the experimental data in many regions.

For the highest $W$ range above 2088 MeV, the data tend to exhibit flatter distributions. The PWA show some general agreement but exhibit strong discrepancies, in particular the strong dip in $G$ predicted around $0.4 \leq cos(\theta) \leq 0.5$ by both the PWA solutions is not strongly evident in the new data.

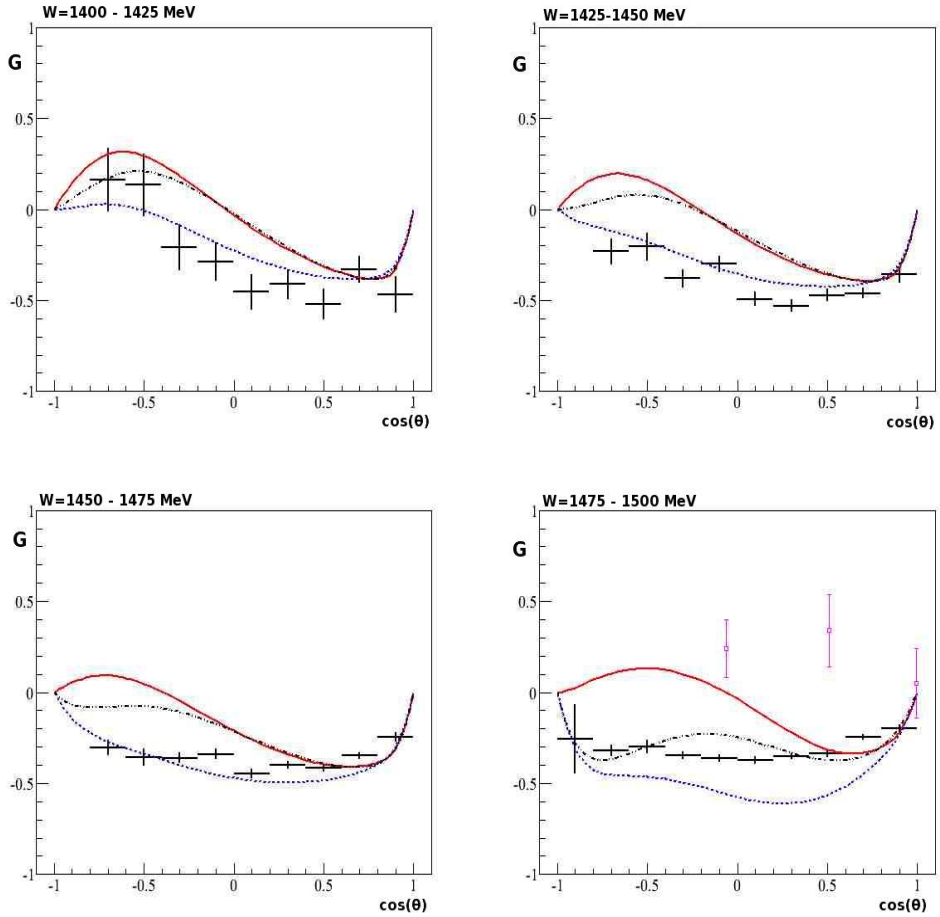


Figure 10.4: New values of the $G$ double-polarisation observable calculated for this thesis (black points) plot as a function of *cos(θ)*. Overlaid on the plots are the current SAID [44] (solid-red line), MAID2007 [44] (dashed-blue line) and Bonn-Gatchina BG2010-02 [48] (dot-dashed black line) PWA solutions, where the new data have not yet been included in the fits. The open pink squares show the previous experimental data for the $G$ observable [71].

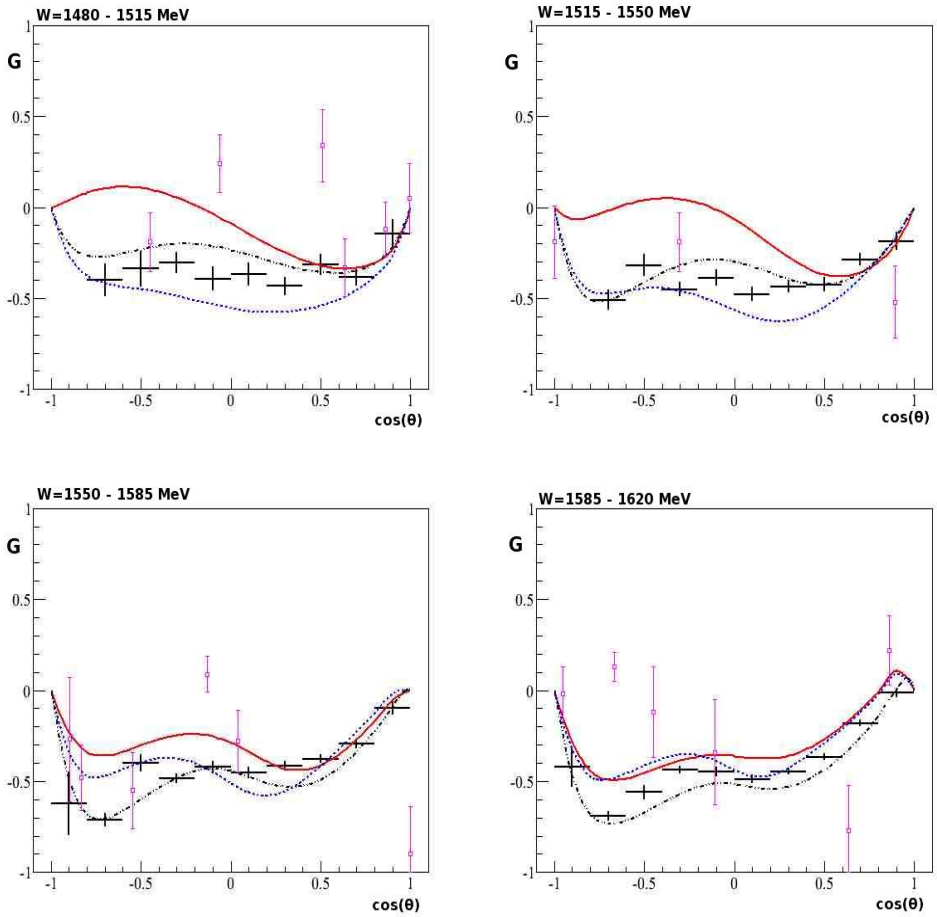


Figure 10.5: New values of the $G$ double-polarisation observable calculated for this thesis (black points) plot as a function of *cos(θ)*. Overlaid on the plots are the current SAID [44] (solid-red line), MAID2007 [44] (dashed-blue line) and Bonn-Gatchina BG2010-02 [48] (dot-dashed black line) PWA solutions, where the new data have not yet been included in the fits. The open pink squares show the previous experimental data for the $G$ observable [71].

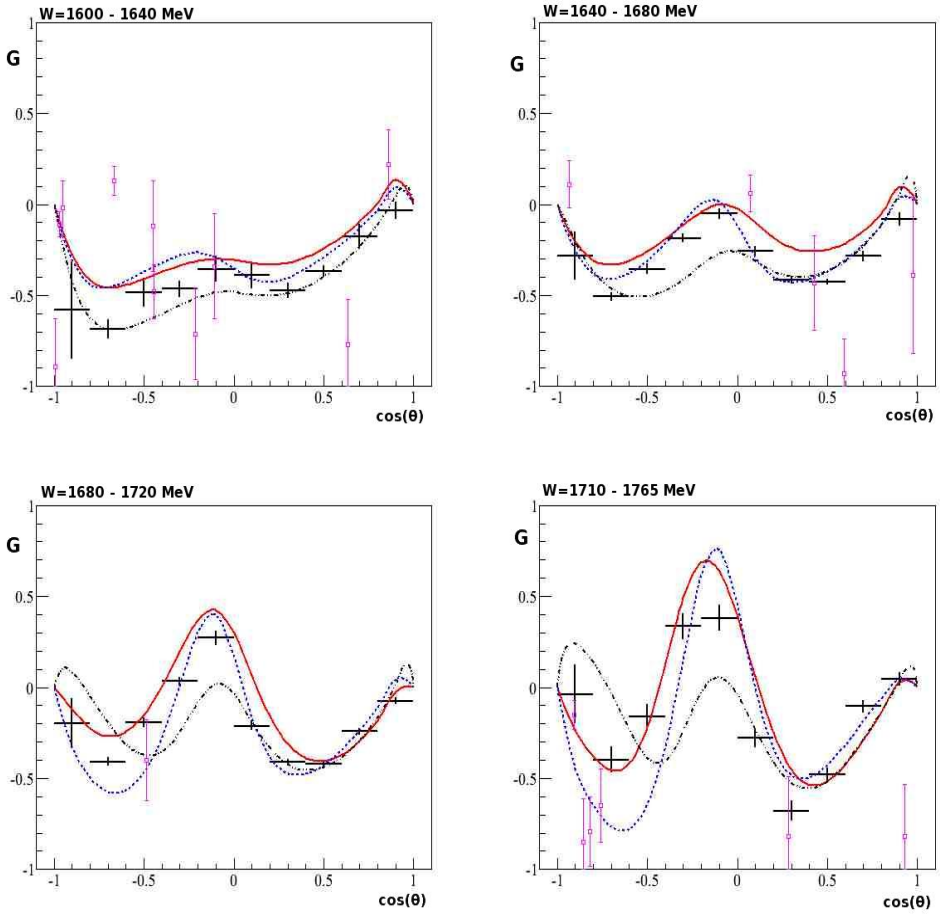


Figure 10.6: New values of the $G$ double-polarisation observable calculated for this thesis (black points) plot as a function of *cos(θ)*. Overlaid on the plots are the current SAID [44] (solid-red line), MAID2007 [44] (dashed-blue line) and Bonn-Gatchina BG2010-02 [48] (dot-dashed black line) PWA solutions, where the new data have not yet been included in the fits. The open pink squares show the previous experimental data for the $G$ observable [71].

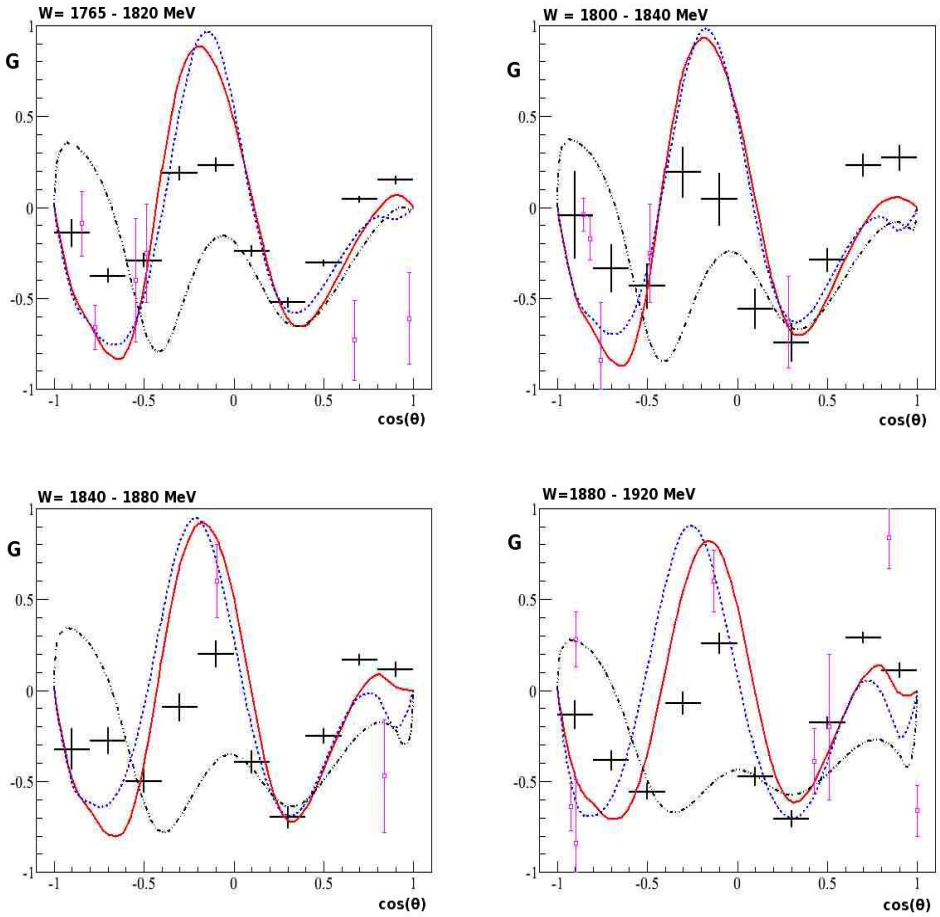


Figure 10.7: New values of the $G$ double-polarisation observable calculated for this thesis (black points) plot as a function of *cos(θ)*. Overlaid on the plots are the current SAID [44] (solid-red line), MAID2007 [44] (dashed-blue line) and Bonn-Gatchina BG2010-02 [48] (dot-dashed black line) PWA solutions, where the new data have not yet been included in the fits. The open pink squares show the previous experimental data for the $G$ observable [71].

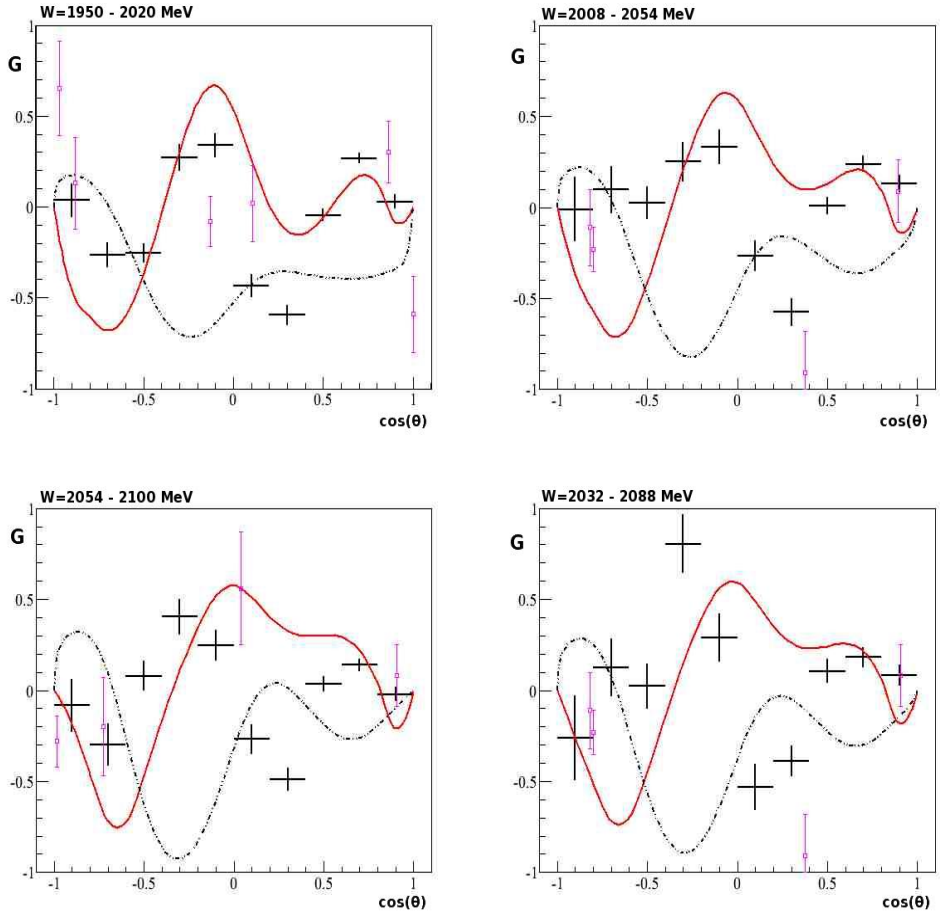


Figure 10.8: New values of the $G$ double-polarisation observable calculated for this thesis (black points) plot as a function of *cos(θ)*. Overlaid on the plots are the current SAID [44] (solid-red line) and Bonn-Gatchina BG2010-02 [48] (dot-dashed black line) PWA solutions, where the new data have not yet been included in the fits. The open pink squares show the previous experimental data for the $G$ observable [71].

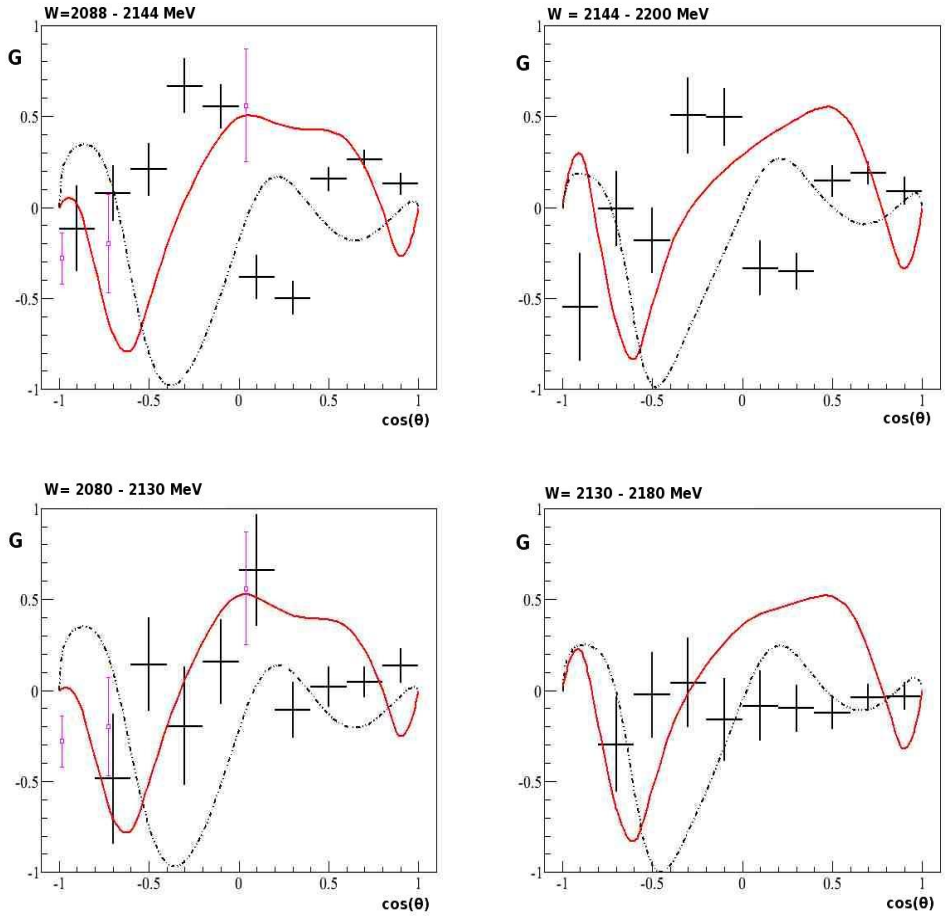


Figure 10.9: New values of the $G$ double-polarisation observable calculated for this thesis (black points) plot as a function of *cos(θ)*. Overlaid on the plots are the current SAID [44] (solid-red line), MAID2007 and Bonn-Gatchina BG2010-02 [48] (dot-dashed black line) PWA solutions, where the new data have not yet been included in the fits. The open pink squares show the previous experimental data for the $G$ observable [71].

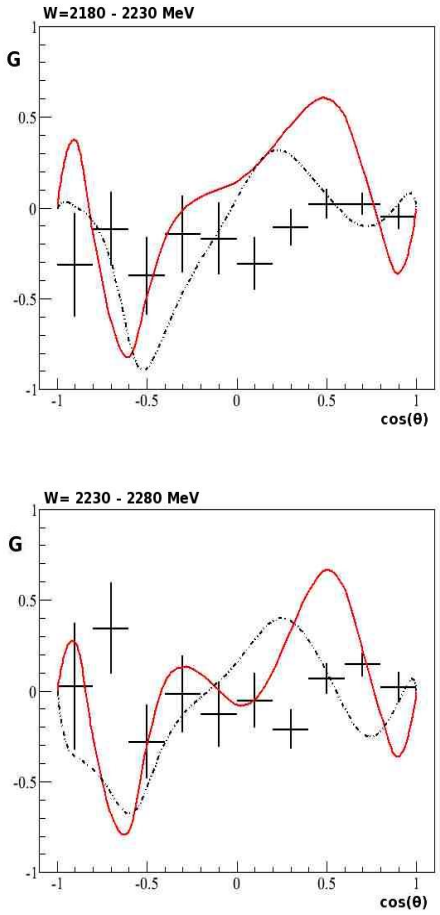


Figure 10.10: New values of the $G$ double-polarisation observable calculated for this thesis (black points) plot as a function of *cos(θ)*. Overlaid on the plots are the current SAID [44] (solid-red line) and Bonn-Gatchina BG2010-02 [48] (dot-dashed black line) PWA solutions, where the new data have not yet been included in the fits.

### 10.2.1 Implications of the Results

The next stage will be for the new data to be included in the partial wave analyses and the resulting effect on the resonance spectrum and its properties established. Clearly the new data will provide a valuable experimental constraint on the PWA solutions. The present analysis indicates that the PWAs are currently underconstrained by experimental data not only in the region of missing resonances, but even in the lower lying part of the resonance spectrum.

Some idea of the expected sensitivity of the new data to resonances can be obtained by examining the current solutions and removing the contribution of certain resonances to explore the resulting effect on G. Figures 10.11 and 10.12 below explore the sensitivity to the low-lying nucleon resonances. As already discussed and seen in Figure 10.4, MAID provided good descriptions of the data below ∼1500 MeV whereas the other PWA solutions did not. As few resonances give strong contributions in this region, it is illustrative to remove the contribution of different resonances to the PWA fit to explore the sensitivity to specific resonances in the data.

In Figures 10.11 and 10.12, the MAID2007 solution for $G$ has been plotted as a function of energy. The solid black line represents the full MAID2007 calculation, including the $P_{33}(1232)$, $P_{11}(1440)$, $D_{13}(1520)$, $S_{11}(1535)$, $S_{31}(1620)$, $S_{11}(1650)$, $D_{15}(1675)$, $F_{15}(1680)$, $D_{33}(1700)$, $P_{13}(1720)$, $F_{35}(1905)$, $P_{31}(1910)$ and $F_{37}(1950)$ resonances[1]. The other lines show the MAID2007 solution with the $S_{11}(1535)$ removed (solid-red line) and with the $P_{11}(1440)$ Roper resonance removed (dashed-blue line) from the fit. The new experimental data have also been superimposed into these Figures, shown as the black points. These figures illustrate how $G$ is a very sensitive observable to the contribution and properties of these low-lying resonances. Including the new data in all the PWA fits would therefore be expected to provide more constraints to these resonances, with information on the Roper resonance being particularly valuable as no model predicts it should be the first excited N* state and its mass, decay width and amplitudes are still poorly established. For example, the decay width of the Roper resonance is listed as 200-450 MeV by the Particle Data Group [1].

It should be noted, however, that this procedure of removing the resonances is

[1]The reader is referred back to Chapter 2 Section 2.6 for an explanation of the spectroscopic notation.

only an approximation; a full refit of the PWA with omission of these resonances has not been performed which would be considered the more correct procedure.

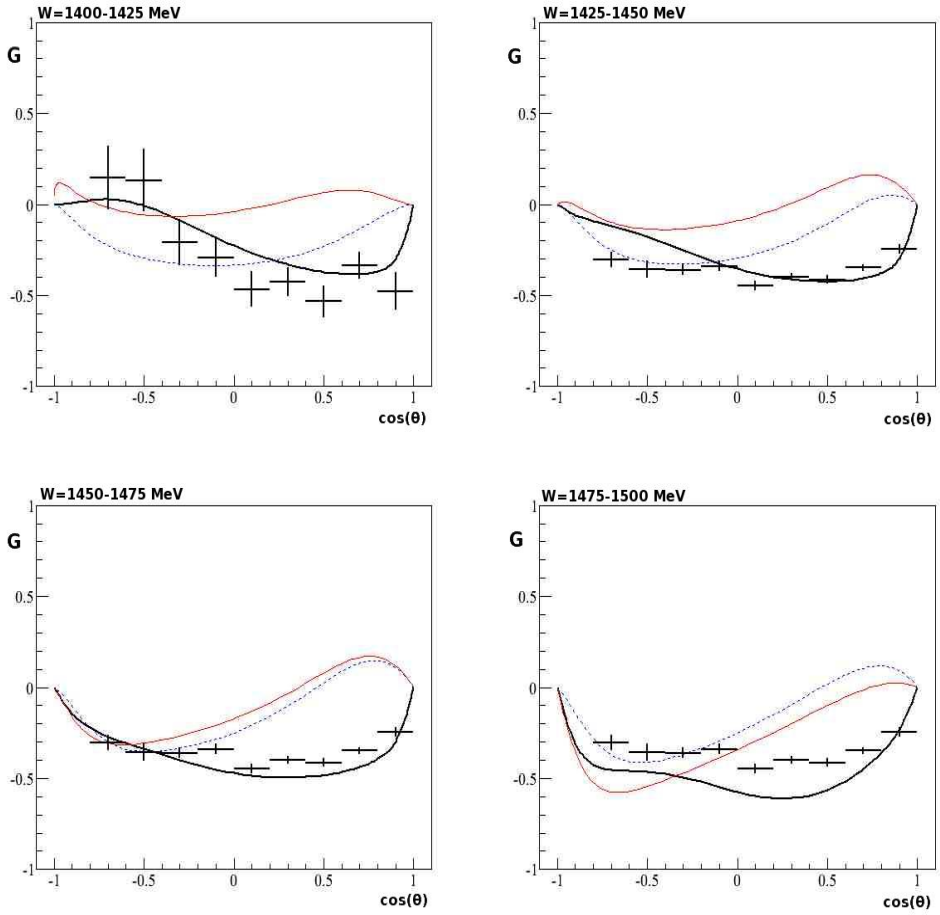


Figure 10.11: The MAID2007 solution [43] for the $G$ double-polarisation observable for the $\gamma(p,\pi^+)n$ channel plot as a function of energy. The solid-black line shows the full solution, the solid-red line shows the full solution with $S_{11}(1535)$ removed from the fit, the dashed-blue line shows the full solution with $P_{11}(1440)$ Roper resonance removed from the fit. The black crosses show the new experimental data presented in this thesis.

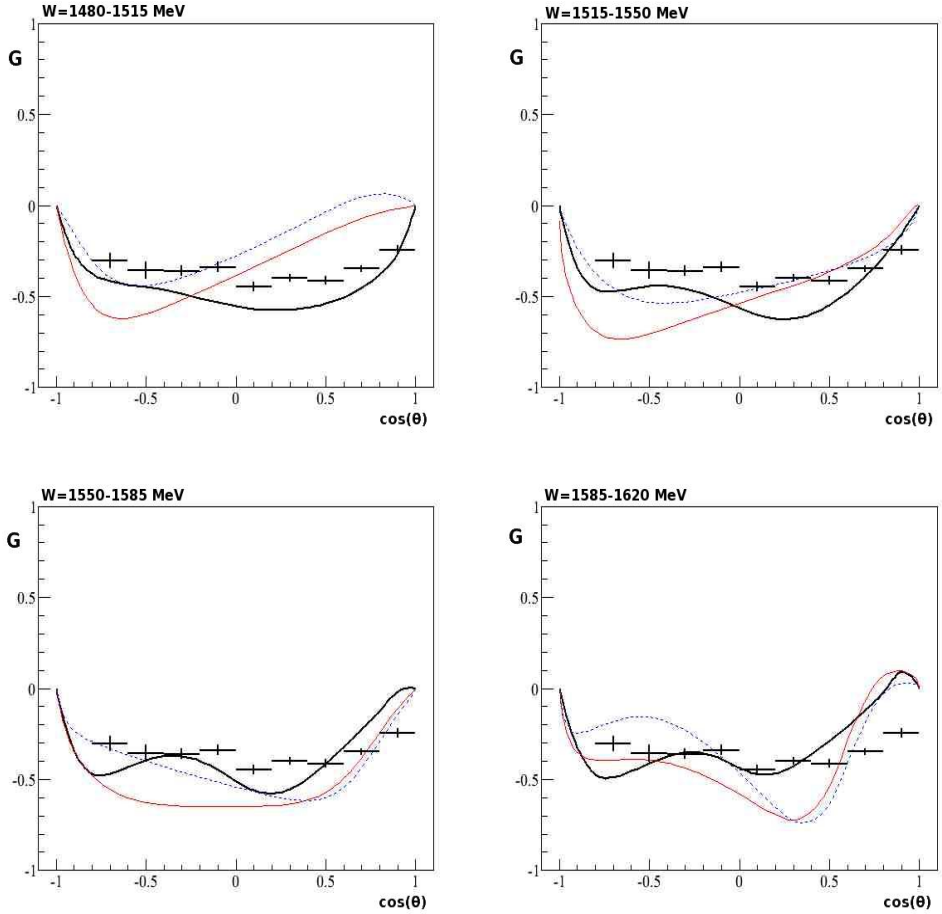


Figure 10.12: The MAID2007 solution [43] for the $G$ double-polarisation observable for the $\gamma(p,\pi^+)n$ channel plot as a function of energy. The solid-black line shows the full solution, the solid-red line shows the full solution with $S_{11}(1535)$ removed from the fit, the dashed-blue line shows the full solution with $P_{11}(1440)$ Roper resonance removed from the fit. The black crosses show the new experimental data presented in this thesis.

# Chapter 11

# Conclusions and Outlook

A new, high statistics measurement of the $G$ double-polarisation observable has been made for the $\gamma(p,\pi^+)n$ reaction in the photon energy range 730-2300 MeV, corresponding to centre-of-mass energies of $W$=1400-2280 MeV, and for pion centre-of-mass angles -1.0$\leq cos(\theta) \leq$1.0. This measurement significantly extends the current world data set for this observable, greatly improving the $W$ and $cos(\theta)$ coverage. The new data provide a step change in the quality of measurement of the $G$ observable compared to previous data and will be a crucial component of the world programme to improve the consistency and quality of the extraction of the nucleon resonance spectrum and its properties through the partial wave analyses of meson photoproduction.

The new data show some limited agreement with the sparse previous measurement of $G$. In particular, there is some noticeable disagreement above $W$=1600 MeV, particularly in the 1600$\leq W \leq$1800 MeV, -0.2$\leq cos(\theta) \leq$0.0 and the 1475$\leq W \leq$1500 MeV, 0.0$\leq cos(\theta) \leq$0.5 kinematic regions where the previous and current values of $G$ are of opposite sign. These differences arise in regions where the previous data have shown long-standing disagreements with the three main PWA solutions. Here the new data fall in the region more consistent with expectations from the PWA. This implies that there may be some unidentified systematic error in the previous data which employed much more complicated methodologies than the current measurement of $G$.

When compared the the current solutions of the three main partial wave analyses (SAID, MAID2007 and Bonn-Gatchina BG2010-02), the new data show general agreement with at least one of these predictions at lower energies

($W \leq 1640$ MeV). However, no single PWA solution can describe the new data for all $W$ bins in this region. In this region near the peak of the Roper resonance at 1440 MeV the data strongly favour the MAID PWA over the SAID and Bonn-Gatchina solutions, indicating that even in the low-lying part of the resonance spectrum, the new data give extremely valuable new information. In the intermediate $W$ range (1640 to 1920 MeV), the strong $cos(\theta^*)$ dependent oscillations in $G$ are observed in experiment for the first time, although the data indicate that the amplitude is smaller than the current PWA expectations. In the region $W \geq 2000$ MeV, where a high density of missing resonances are predicted to occur, the PWA solutions diverge and do not provide a good description of the new experimental data.

Once the linear beam polarisations have been finalised, the new experimental data for the $G$ observable will be included in future partial wave analyses, such as MAID, SAID and Bonn-Gatchina. The comprehensive angular coverage and statistical accuracy of the new data, provided by this thesis will greatly help to constrain the partial wave analyses and the extraction of the reaction amplitudes in these calculations. In conjunction with the measurements of polarisation observables currently being performed at Jefferson Lab, MAMI, ELSA, GRAAL and Spring8, this thesis is an important step towards the measurement of a "complete" set of experimental observables which will better constrain the amplitudes of the PWA calculations. Achieving as close to a model-independent PWA solution as possible is the crucial next step to determine the resonance spectrum of the nucleon and its properties with accuracy for the first time. The properties of this fundamental excitation spectrum providesunique and stringent constraints on the dynamics and degrees of freedom of the components of the nucleon and non-perturbative QCD. The partial wave analyses will search for missing nucleon resonances predicted by almost all QCD-based theories but not yet observed. Improvements in the world data set of the experimental observables also allows better establishing the masses, widths and electromagnetic couplings of all resonances.

# Appendix A

# The $G$ Observable for both target settings

Figures A.1 to A.3 show the $G$ observable plot as a function of centre of mass energy, $W$, for all ten bins in $cos(\theta)$. Values of $G$ extracted from the positively polarised butanol target are shown in red, while $G$ from the negatively polarised butanol target is shown in blue. The two data sets shown in these figures are, in general, consistent with each other, suggesting that the calculation of target polarisation (Chapter 6) and data analysis procedures (Chapters 8 and 9) are reliable. The values of $G$ presented in the Results Chapter (Chapter 10) are the weighted mean of the values presented in this Appendix.

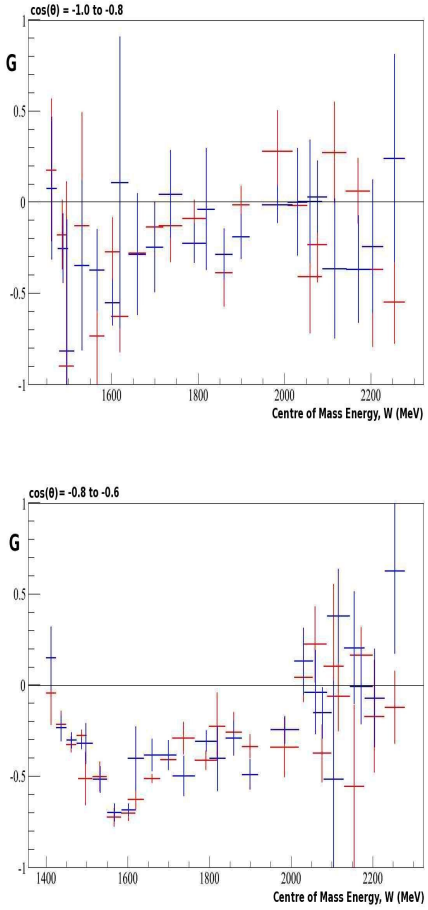


Figure A.1: The $G$ observable plot as a function of centre of mass energy $W$. Values extracted from the positively polarised butanol target are shown in red, while values extracted from the negatively polarised butanol target are shown in blue.

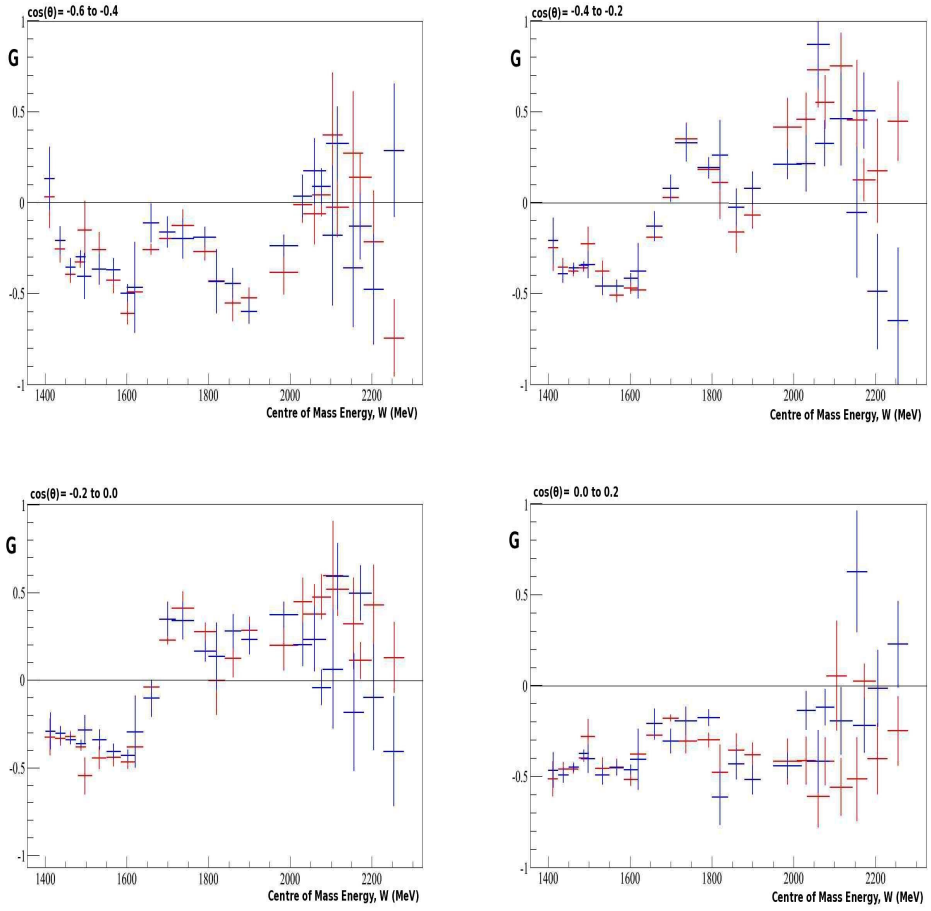


Figure A.2: The $G$ observable plot as a function of centre of mass energy $W$. Values extracted from the positively polarised butanol target are shown in red, while values extracted from the negatively polarised butanol target are shown in blue.

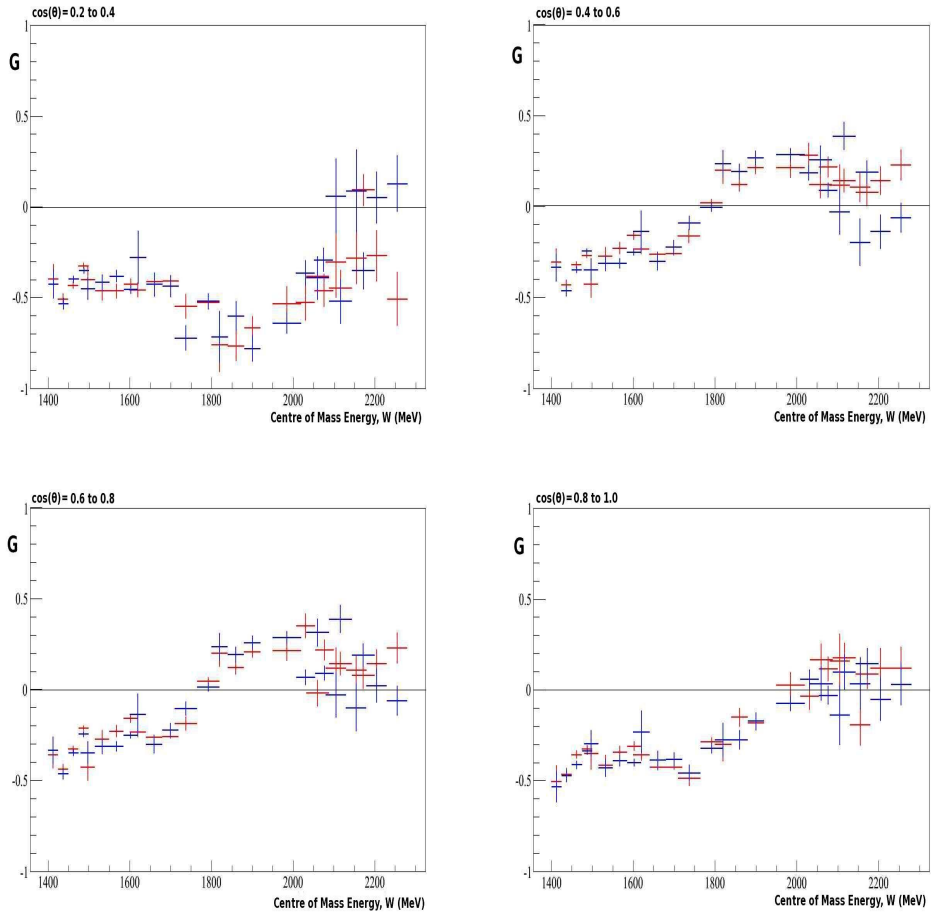


Figure A.3: The $G$ observable plot as a function of centre of mass energy $W$. Values extracted from the positively polarised butanol target are shown in red, while values extracted from the negatively polarised butanol target are shown in blue.

# Appendix B

# The $\Sigma$ Observable for both target settings

Figure B.1 shows the $\Sigma$ observable plot as a function of centre of mass energy, *W*, for all five bins in *cos(θ)*. The weighted mean of $\Sigma$ extracted from both the polarised butanol target for both target settings is shown in black. The data from the unpolarised $CH_2$ target was divided according to the run numbers corresponding to each polarised butanol target setting. The weighted mean of $\Sigma$ extracted from the unpolarised $CH_2$ target for each of these subsets of data is shown in red. The two data sets shown in these figures are, in general, consistent with each other, suggesting that the calculation of target polarisation (Chapter 6) and data analysis procedures (Chapters 8 and 9) are reliable. Note that these values are not for $\Sigma$ on the free proton, and as such cannot be compared directly to the PWA solutions or previous experimental data for this observable.

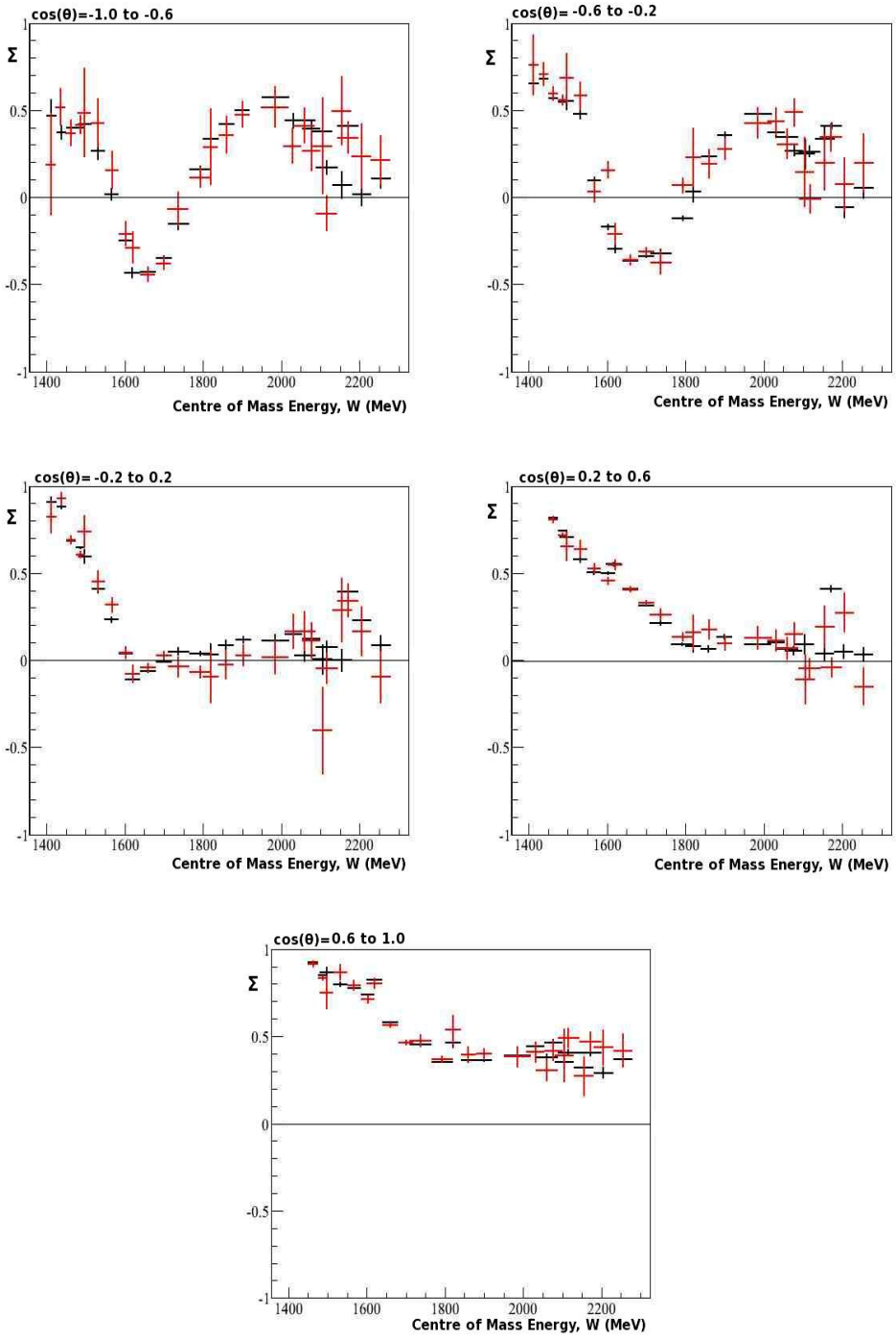


Figure B.1: The Σ observable plot as a function of centre of mass energy $W$. Values extracted from the butanol target are shown in black, while values extracted from the $CH_2$ target are shown in red.

# Bibliography


[1] The Particle Data Group, `http://pdg.lbl.gov`.

[2] D. H. Perkins, *Introduction to High Energy Physics*, fourth ed. (CUP, Cambridge, 2000).

[3] B. R. Martin and G. Shaw, *Particle Physics*, 3rd ed. (Wiley, Chichester, England, 2008).

[4] A. Watson, *The Quantum Quark*, 1st ed. (CUP, Cambridge, 2004).

[5] *Murray Gell-Mann Selected Papers*, 1st ed., edited by H. Fritzsch (World Scientific Series in 20th Century Physics, New Jersey, 2010).

[6] S. Bethke, Prog. Part. Nucl. Phys. **58**, 351 (2007).

[7] K. Wilson, Physical Review D **10**, 2445 (1974).

[8] The Frontiers of Nuclear Science, A Long Range Plan, arXiv:0809.3137v1 [nucl-ex], 2007.

[9] G. P. Lepage, Lattice QCD for Novices, arXiv:hep-lat/0506036v1, 2005.

[10] A. W. Thomas and W. Weise, *The Structure of the Nucleon*, 1st ed. (Wiley-VCH, Weinheim, 2001).

[11] S. Durr *et al.*, Science **322**, 1224 (2008).

[12] J. W. Negele *et al.*, Physical Review D **74**, 034508 (2006).

[13] S. Basak *et al.*, Physical Review D **72**, 094506 (2005).

[14] J. Dudek, Meson and baryon spectroscopy from Lattice QCD, `http://irfu.cea.fr/Documentation/Conferences/webCALS12/Talks/March9/dudek.pdf`, 2011.

[15] J. F. Donoghue, Medium Energy Antiprotons and the Quark Gluon Structure of Hadrons **58**, 39 (1990).

[16] V. Bernard and U.-G. Meissner, Annual Review of Nuclear and Particle Science **57**, 33 (2007).

[17] S. Capstick and W. Roberts, Prog. Part. Nucl. Phys. **45**, S241 (2000).

[18] C. E. DeTar and J. Donoghue, Ann. Rev. Nucl. Part. Sci. **33**, 235 (1983).

[19] L. Chang *et al.*, Exploring the light quark interaction, arXiv:0906.4304v2 [nucl-th], 2009.

[20] D. Faiman and A. W. Hendry, Physical Review **173**, 1720 (1968).

[21] A. deRujula *et al.*, Physical Review D **12**, 147 (1975).

[22] N. Isgur and G. Karl, Physical Review D **20**, 1191 (1979).

[23] M. Anselmino *et al.*, Review of Modern Physics **65**, 1199 (1993).

[24] E. Santopinto, Physical Review C **72**, 022201 (2005).

[25] D. B. Leinweber, Physical Review D **47**, 5096 (1993).

[26] P. N. Bogoliubov, Ann. Inst. Henri Poincare **8**, 163 (1967).

[27] A. Chodos *et al.*, Physical Review D **9**, 3471 (1974).

[28] S. Theberge and A. W. Thomas, Physical Review D **22**, 2838 (1980).

[29] T. DeGrand *et al.*, Physical Review D **12**, 2060 (1975).

[30] K. Nakamura and others (Particle Data Group), Journal of Physics G **37**, 075021 (2010).

[31] N. Bianchi *et al.*, Physical Review C **54**, 1688 (1996).

[32] R. L. Walker, Physical Review **182**, 1729 (1969).

[33] S. Playfer, Senior Honours Particle Physics Lecture Notes, `http://www2.ph.ed.ac.uk/teaching/course-notes/documents/75/1480-feynman.pdf`.

[34] J. Bjorken and S. Drell, *Relativistic Quantum Mechanics*, 1st ed. (McGraw Hill, New York, 1964).

[35] A. Nagl, V. Devanathan, and H. Uberall, *Nuclear Pion Photoproduction*, 1st ed. (Springer-Verlag, Heidelberg, 1991).

[36] G. F. Chew *et al.*, Physical Review **106**, 1345 (1957).

[37] B. Krusche and S. Schamand, Prog. Part. Nucl. Phys. **51**, 399 (2003).

[38] R. M. Davidson, Czechoslovak Journal of Physics **44**, 365 (1994).

[39] I. S. Barker, A. Donnachie, and J. K. Storrow, Nuclear Physics B **79**, 431 (1974).

[40] I. S. Barker, A. Donnachie, and J. K. Storrow, Nuclear Physics B **95**, 347 (1975).

[41] G. Keaton and R. Workman, Physical Review C **53**, 1434 (2006).

[42] W.-T. Chiang and F. Tabakin, Physical Review C **55**, 2054 (1997).

[43] The MAID Homepage, `http://www.kph.uni-mainz.de/MAID`.

[44] CNS Data Analysis Center, `http://gwdac.phys.gwu.edu`.

[45] D. Drechsel, S. S. Kamalov, and L. Tiator, European Physical Journal A **34**, 69 (2007).

[46] R. A. Arndt *et al.*, Physical Review C **42**, 1853 (1990).

[47] R. A. Arndt *et al.*, Physical Review C **66**, 055213 (2002).

[48] Bonn Gatchina Partial Wave Analysis, `http://pwa.hiskp.uni-bonn.de`.

[49] A. V. Anisovich *et al.*, Photoproduction of pions and properties of baryon resonances from a Bonn-Gatchina partial wave analysis, arXiv:0911.5277.

[50] T. Sato and T.-S. Lee, Journal of Physics G-Nuclear and Particle Physics **36**, 073001 (2009).

[51] A. Matsuyama, T. Sato, and T.-S. Lee, Physics Reports-Review Section of Physics Letters **439**, 193 (2007).

[52] Excited Baryon Analysis Center, `http://ebac-theory.jlab.org`.

[53] L. M. Brown, M. Dresden, and L. Hoddeson, *Pions to Quarks: Particle Physics in the 1950s: Based on a Fermilab Symposium* (CUP, Cambridge, 1989).

[54] A. A. Komar, *Photoproduction of Pions on Nucleons and Nuclei* (Nova Science Publishers, New York, 1989).

[55] T.-S. H. Lee and L. C. Smith, Journal of Physics G: Nuclear and Particle Physics **34**, S83 (2007).

[56] R. A. Arndt *et al.*, Proposal to Jefferson Lab PR-03-105: Pion Photoproduction from a Polarized Target, 2007.

[57] J. Ball *et al.*, Proposal to Jefferson Lab PR-05-012: Measurement of polarization observables in $\eta$ photoproduction with CLAS, 2007.

[58] D. I. Sober *et al.*, Proposal to Jefferson Lab: PR-04-102: Helicity Structure in Pion Photoproduction, 2007.

[59] L. Blaszczyk *et al.*, Proposal to Jefferson Lab: PR-06-013: Measurement of $\pi^+\pi^-$ Photoproduction in Double Polarization Experiments using CLAS, 2007.

[60] F. J. Klein *et al.*, Proposal to Jefferson Lab: PR-02-112: Search for missing Nucleon resonances in the Photoproduction of Hyperons using a Polarized Photon Beam and a Polarized Target, 2007.

[61] R. Beck, Chinese Physics C **33**, 1056 (2009).

[62] D. Elsner, International Journal of Modern Physics E: Nuclear Physics **19**, 869 (2010).

[63] H. J. Arends, A. Braghieri, M. Kotulla, and A. Thomas, Mainz Proposal A2/7-07: Helicity Dependence of Meson Photoproduction on the Proton, 2007.

[64] R. Becka, K. Livingston, and E. Heid, Mainz Proposal A2/7-09: Measurement of the G asymmtetry in $\gamma p \rightarrow p\pi^0$ and $\gamma p \rightarrow p\pi^+$, 2009.

[65] A. M. Bernstein, W. Deconinck, D. Hornidge, and M. Ostrick, Mainz Proposal A2/10-09: Mesurement of Polarised Target and Beam Asymmetries in Pion Photoproduction: Test of Chiral Dynamics, 2009.

[66] V. L. Kaseravov, A. Fix, and M. Ostrick, Mainz Proposal A2/9-09: Single Polarisation Observables in $\pi\eta$ Photoproduction in the $D_{33}(1700)$ Region, 2009.

[67] B. Krusche and W. Briscoe, Mainz Proposal A2/10-05: Photoproduction of $\eta$ mesons off the neutron Part I: Angular Distribution and Double Polarisation Observable E, 2005.

[68] M. Rost, R. Beck, and K. Livingston, Mainz Proposal A2/8-05: Measurement of the G Asymmetry in $\gamma p \rightarrow p\pi^0$ and $\gamma p \rightarrow p\pi^+$, 2005.

[69] D. P. Watts, G. Rosner, D. I. Glazier, and P. Pedroni, Mainz Proposal A2/5-05: Recoil Polarimetry Observables in Meson Photoproduction at MAMI, 2005.

[70] D. P. Watts, D. I. Glazier, and J. Annand, Mainz Proposal A2/3-09: Polarisation Observables using Nucleon Polarimetry with the Crystal Ball at MAMI, 2009.

[71] P. J. Bussey *et al.*, Nuclear Physics B **169**, 403 (1980).

[72] P. J. Bussey *et al.*, Nuclear Physics B **159**, 383 (1979).

[73] I. M. Barbour, R. L. Crawford, and N. H. Parsons, Nuclear Physics B **B141**, 253 (1978).

[74] A. A. Belyaev *et al.*, Soviet Journal of Nuclear Physics **40**, 83 (1984).

[75] W. J. Metcalf and R. L. Walker, Nuclear Physics B **B76**, 253 (1976).

[76] P. Fëller *et al.*, Nuclear Physics B **B104**, 219 (1976).

[77] J. Ahrens *et al.*, European Physical Journal A **26**, 135 (2005).

[78] E. S. Smith, Nuclear Physics A **827**, 599c (2009).

[79] J. Alcorn *et al.*, Nuclear Instruments and Methods in Physics Research A **522**, 294 (2004).

[80] O. K. Baker *et al.*, Nuclear Instruments and Methods in Physics Research A **367**, 92 (1995).

[81] Thomas Jefferson National Accelerator Facility Official Website, `http://www.jlab.org`, 2010.

[82] B. A. Mecking *et al.*, Nuclear Instruments and Methods in Physics Research A **503**, 513 (2003).

[83] D. I. Sober *et al.*, Nuclear Instruments and Methods in Physics Research A **440**, 263 (2000).

[84] J. M. Grames *et al.*, Physical Review Special Topics-Accelerators and Beams **7**, 04280201 (2004).

[85] C. K. Sinclair *et al.*, Physical Review Special Topics - Accelerators and Beams **10**, 02350101 (2007).

[86] C. W. Leeman, D. R. Douglas, and G. A. Krafft, Annual Review of Nuclear and Particle Science **51**, 413 (2001).

[87] C. Hovater *et al.*, The CEBA RF Separator System, 1996, proceedings of the LINAC 1996 Conference, Geneva, Switzerland, August 1996.

[88] JLab Hall B Electronic Logbook, `http://www.clasweb.jlab.org/clasonline/prodlogsearch.html`, 2008.

[89] F. Klein *et al.*, The Coherent Bremsstrahlung Facility in Hall B at Jefferson Lab, 2008, www.jlab.org/∼fklein/cbf_nim_v2.0.pdf.

[90] J. D. Kellie *et al.*, Nuclear Instruments and Methods in Physics Research A **545**, 164 (2005).

[91] K. Livingston, Nuclear Instruments and Methods in Physics Research A **603**, 205 (2009).

[92] H. Bilokon *et al.*, Nuclear Instruments and Methods in Physics Research **204**, 299 (1983).

[93] F. A. Natter *et al.*, Nuclear Instruments and Methods in Physics Research B **211**, 465 (2003).

[94] A. A. Sabintsev and K. Livingston, CLAS-NOTE 2010-009: A Preliminary Investigation of Linear Polarization in g9a/FROST, 2010.

[95] M. D. Mestayer *et al.*, Nuclear Instruments and Methods in Physics Research A **449**, 81 (2000).

[96] E. Pasyuk, FROST Readiness Review, `http://clasweb.jlab.org/rungroups/g9/wiki/files/FROST_readiness.pdf`, 2007.

[97] D. Tilles, Hall B Picture Archive, `http://www.jlab.org/$\sim$tilles/miniT/master_thumb_index.html`.

[98] Y. G. Sharabian *et al.*, Nuclear Instruments and Methods in Physocs Research A **556**, 246 (2006).

[99] G. Adams *et al.*, Nuclear Instruments and Methods in Physics Research A **465**, 414 (2001).

[100] E. S. Smith *et al.*, Nuclear Instruments and Methods in Physics Research A **432**, 265 (1999).

[101] M. Amarian *et al.*, Nuclear Instruments and Methods in Physics Research A **460**, 239 (2001).

[102] M. Anghinolfi *et al.*, Nuclear Instruments and Methods in Physics Research A **447**, 424 (2000).

[103] M. Anghinolfi *et al.*, Nuclear Instruments and Methods in Physics Research A **537**, 562 (2005).

[104] D. C. Doughty Jr. *et al.*, Nucl. Sci. IEEE Transactions **39**, 241 (1992).

[105] Jefferson Lab Data Acquisition Group CODA Wiki, `https://coda.jlab.org/Wiki/`.

[106] D. G. Crabb and W. Meyer, Annual Review of Nuclear and Particle Science **47**, 67 (1997).

[107] T. O. Niinikoski and F. Udo, Nuclear Instruments and Methods in Physics Research A **134**, 219 (1976).

[108] C. D. Keith *et al.*, Nuclear Instruments and Methods in Physics Research A **501**, 327 (2003).

[109] C. D. Keith, M. L. Seeley, and O. Dzyubak, in *GDH 2004: Proceedings of the 3rd International Symposium on the Gerasimov-Drell-Hearn Sum Rule and its Extensions* (World Scientific, New Jersey, 2004).

[110] C. D. Keith, Freezing the Spin of the Proton The Next Generation Polarized Target for CLAS, `http://www.jlab.org/frost/CLAS_FST_Talks.html`, jefferson Lab Seminar given by Chris Keith on the 9th June 2004.

[111] E. Pasyuk, Private Communication, 2010.

[112] C. D. Keith, Private Communication, 2010.

[113] C. D. Keith, Frozen Spin Targets in a Nutshell Volume 3: RESULTS, `http://www.jlab.org/$\sim$ckeith/Frozen/FrozenSpinNutshell3.pdf`, jefferson Lab Hall B Seminar given by Chris Keith in 2008.

[114] S. Mango, Nuclear Instruments and Methods in Physics Research A **526**, 1 (2004).

[115] M. Borghini, CERN Report: Choice of Substances for Polarised Proton Targets, 1966.

[116] M. Pluckthun *et al.*, Nuclear Instruments and Methods in Physics Research A **400**, 133 (1997).

[117] J. Pierce, Private Communication, 2010.

[118] D. A. Hill and J. J. Hill, 1981, argonne National Laboratory Report ANL-HEP-PR-81-05.

[119] F. Pobell, *Matter and Methods at Low Temperatures*, 2nd ed. (Springer, Heidelberg, 1996).

[120] H. London, G. R. Clarke, and E. Mendoza, Physical Review **128**, 1992 (1962).

[121] O. V. Lounasmaa, J. Phys. E: Sci. Instrum. **12**, 668 (1979).

[122] M. H. Levitt, *Spin Dynamics: Basics of Nuclear Magnetic Resonance* (Wiley, New York, 2008).

[123] T. C. Pochapsky and S. S. Pochapsky, *NMR For Physical and Biological Scientists*, 1st ed. (Garland Science, London, 2007).

[124] C. D. Keith, Frozen Spin Targets in a Nutshell Version 1.0, `http://www.jlab.org/$\sim$ckeith/Frozen/FrozenSpinNutshell.pdf`, jefferson Lab Hall B Seminar given by Chris Keith on the 20th March 2006.

[125] A. Abragam and M. Goldman, Rep. Prog. Phys. **41**, 395 (1978).

[126] A. Abragam and W. G. Proctor, Physical Review **109**, 1441 (1958).

[127] C. F. Hwang and D. A. Hill, Physical Review Letters **19**, 1011 (1967).

[128] C. D. Keith, Frozen Spin Targets in a Nutshell Version 2.0, `http://www.jlab.org/$\sim$ckeith/Frozen/FrozenSpinNutshell2.pdf`, jefferson Lab Hall B Seminar given by Chris Keith in 2006.

[129] Photographs of FROST taken by the Jefferson Lab Polarized Target Group, `http://www.jlab.org/$\sim$ckeith/Frozen/Photos/Photos.html`.

[130] C. Bradtke *et al.*, Nuclear Instruments and Methods in Physics Research A **436**, 430 (1999).

[131] G. R. Court *et al.*, Nuclear Instruments and Methods in Physics Research A **324**, 433 (1993).

[132] Experimental and Industrial Control System, EPICS Home Page, `http://www.aps.nnl.goc/epics/`.

[133] National Instruments Website, `http://www.ni.com/labview`.

[134] The ROOT System Homepage, `http://root.cern.ch`.

[135] M. Goldman, J. F. Jacquinot, M. Chapellier, and V. H. Chau, Journal of Magnetic Resonance **18**, 22 (1975).

[136] P. Hautle, Nuclear Instruments and Methods in Physics Research A **526**, 76 (2004).

[137] Lakeshore Cryotronics Website, `http://www.lakeshore.com`, accessed February 2010.

[138] E. S. Smith *et al.*, Calibration of the CLAS TOF System, CLAS-NOTE 1999-011, 1999.

[139] G. Gavalian, C interface to mySQL for monitoring and storing CLAS data analyses results, CLAS-NOTE 2002-011, 2002.

[140] E. Anciant *et al.*, Tagger hit reconstruction software and tagger calibration overview, CLAS-NOTE 1999-04, 1999.

[141] J. Li, The New Tagger Calibration Program, CLAS-NOTE 2003-004, 2003.

[142] D. I. Sober, A Guide to the Optics of the Tagged Photon Magnet, CLAS-NOTE 91-012, 1991.

[143] D. Sokhan, Beam Asymmetry Measurement from Pion Photoproduction on the Neutron, University of Edinburgh Thesis, 2009.

[144] D. Lawrence and M. Mestayer, CLAS Drift Chamber Calibration: Software Procedures, CLAS-NOTE 1999-018, 1999.

[145] M. Guillo *et al.*, EC Time Calibration Procedure for Photon Runs in CLAS, CLAS-NOTE 2001-014, 2001.

[146] The ROOTBEER Homepage, `http://nuclear.gla.ac.uk/$\sim$kl/rootbeer/index.php`.

[147] E. Pasyuk, Energy loss corrections for charged particles in CLAS, CLAS-NOTE 2007-016, 2007.

[148] K. S. Krane, *Introductory Nuclear Physics*, 1st ed. (John Wiley and Sons, New York, 1988).

[149] K. Livingston, Private Communication, 2011.